

COMPARISON OF ALLOYED AND NON-ALLOYED OHMIC CONTACTS IN
GAN/ALGAN HEMT FOR KA BAND RADAR APPLICATIONS

A THESIS SUBMITTED TO
THE GRADUATE SCHOOL OF NATURAL AND APPLIED SCIENCES
OF
MIDDLE EAST TECHNICAL UNIVERSITY



BY

HÜSEYİN ÇAKMAK

IN PARTIAL FULFILLMENT OF THE REQUIREMENTS
FOR
THE DEGREE OF DOCTOR OF PHILOSOPHY
IN
MICRO AND NANOTECHNOLOGY

DECEMBER 2020

Approval of the thesis:

**COMPARISON OF ALLOYED AND NON-ALLOYED OHMIC
CONTACTS IN GAN/ALGAN HEMT FOR KA BAND RADAR
APPLICATIONS**

submitted by **HÜSEYİN ÇAKMAK** in partial fulfillment of the requirements for the degree of **Doctor of Philosophy in Micro and Nanotechnology, Middle East Technical University** by,

Prof. Dr. Halil Kalıpçılar
Dean, Graduate School of **Natural and Applied Sciences** _____

Prof. Dr. Almıla Güvenç Yazıcıoğlu
Head of the Department, **Mechanical Engineering** _____

Assist. Prof. Dr. Bilge İmer
Supervisor, **Metallurgical and Materials Eng. Dept., METU** _____

Assoc. Prof. Dr. Alpan Bek
Co-Supervisor, **Physics Department, METU** _____

Examining Committee Members:

Prof. Dr. Ekmel Özbay
Electrical and Electronics Eng. Dept., Bilkent University _____

Assist. Prof. Dr. Bilge İmer
Metallurgical and Materials Eng. Dept., METU _____

Prof. Dr. Hüsni Emrah Ünalın
Metallurgical and Materials Eng. Dept., METU _____

Prof. Dr. Hakan Ateş
Metallurgical and Materials Eng. Dept., Gazi University _____

Prof. Dr. Burcu Akata Kurç
Micro and Nanotechnology Dept., METU _____

Date: 28.12.2020



I hereby declare that all information in this document has been obtained and presented in accordance with academic rules and ethical conduct. I also declare that, as required by these rules and conduct, I have fully cited and referenced all material and results that are not original to this work.

Name, Last name: Hüseyin Çakmak

Signature:

ABSTRACT

COMPARISON OF ALLOYED AND NON-ALLOYED OHMIC CONTACTS IN GAN/ALGAN HEMT FOR KA BAND RADAR APPLICATIONS

Çakmak, Hüseyin

Doctor of Philosophy, Micro and Nanotechnology

Supervisor: Assist. Prof. Dr. Bilge İmer

Co-Supervisor: Assoc. Prof. Dr. Alpan Bek

December 2020, 128 pages

Gallium Nitride (GaN) based **H**igh **E**lectron **M**obility **T**ransistor (HEMT) is the most powerful alternative for high-power and high-frequency applications due to its unique material properties, such as high breakdown field, high electron drift velocity, high operation temperatures, high radiation resistance. Low ohmic contact resistance (R_c) is critical to enhancing the device performance at high frequency and high output power. Various metal stacks with different metal types have been reported in literature. Annealing these metal stacks at high temperatures (above 800 °C) leads to a deterioration in the metal surface morphology and metal edge acuity which makes it difficult to carry out further operations to form the gate region. On top of increasing the production costs, high annealing temperatures may also result in thermal degradation of the epitaxial heterostructure.

In this work, high temperature annealing of metal stacks was eliminated by the development of MOCVD regrown InGaN layers and ALD grown AZO non-alloyed ohmic contacts, which does not require high temperature annealing of metal pads. These contacts were specifically studied for Ka-band application of GaN-based HEMT devices. To our best knowledge, MOCVD regrown InGaN layers and ALD grown AZO films as non-alloyed ohmic contacts were implemented to GaN-based

HEMT devices for Ka-band applications first time in literature. MOCVD regrown InGaN layers and ALD grown AZO films exhibited degenerate doping ($>10^{19}\text{cm}^{-3}$) low resistivity ($\sim 10^{-3}\ \Omega\cdot\text{cm}$) crucial for ohmic contacts to GaN materials. Improved contacts resistance of non-alloyed regrown InGaN ohmic contacts down to $0.3\ \Omega\cdot\text{mm}$ compared to HEMT with alloyed ohmic contacts was accomplished. Alloyed ohmic contacts were also optimized with varying the barrier metal, metal thicknesses, and annealing conditions for comparison. $0.41\ \Omega\cdot\text{mm}$ contact resistance was achieved for the alloyed ohmic contact with Ni barrier and the corresponding HEMT device yielded $2.80\ \text{W}/\text{mm}$. An almost 7% improvement was observed in both drain-source current (I_{ds}), transconductance (g_{m}), and small-signal performance. Large-signal measurements showed that the output power of the HEMT with non-alloyed regrown InGaN ohmic contact was $3.07\ \text{W}/\text{mm}$ which was 9% higher compared to HEMT with alloyed ohmic contacts. Although, initial trials did not yield expected results due to not optimized recess etching and post-plasma cleaning conditions, there is still room for improvement for the ALD of AZO ohmic contacts.

Keywords: AlGaN HEMT, MOCVD, AZO, ALD, Ohmic Contacts, High Frequency

ÖZ

KA BANT RADAR UYGULAMALARI İÇİN GAN / ALGAN HEMT YAPILARINDA ALAŞIMLI VE ALAŞIMSIZ OHMİK KONTAKLARIN KARŞILAŞTIRILMASI

Çakmak, Hüseyin
Doktora, Mikro ve Nanoteknoloji
Tez Yöneticisi: Dr. Öğr. Üyesi Bilge İmer
Ortak Tez Yöneticisi: Doç. Dr. Alpan Bek

Aralık 2020, 128 sayfa

Galyum Nitrür (GaN) bazlı Yüksek Elektron Hareketlilik Transistörü (HEMT), yüksek kırılma alanı, yüksek elektron sürüklenme hızı, yüksek çalışma sıcaklıkları gibi benzersiz malzeme özellikleri nedeniyle yüksek güçlü ve yüksek frekanslı uygulamalar için en güçlü alternatiftir. Düşük bir omik temas direnci (R_c), yüksek frekans ve yüksek çıkış gücünde cihaz performansını artırmak için kritik öneme sahiptir. Yüksek sıcaklıklarda (800 °C'nin üzerinde) metal yığınlarının tavlama, metal yüzey morfolojisinde ve metal kenar keskinliğinde bozulmaya yol açar ve bu durum aygıt üretiminde başta kapı kontak metal hizalaması olmak üzere sonraki aşamaların gerçekleştirilmesini zorlaştırır. Üretim maliyetlerini artırmanın yanı sıra, yüksek tavlama sıcaklıkları ayrıca epitaksiyel heteroyapı kalitesinde bozulmalara neden olabilir.

Bu çalışmada, Ka-Band uygulamaları için, GaN tabanlı HEMT aygıt üretiminde yüksek sıcaklık tavlama işlemine ihtiyaç duymayan MOCVD yeniden büyütme yöntemi ile üretilen InGaN tabakaları ve ALD yöntemi ile üretilen AZO tabakaları kullanılarak alaşimsız omik kontak geliştirme çalışmaları yapılmıştır. Bu kontaklar

özellikle Ka-Band uygulamaların için üretilen GaN tabanlı HEMT yapıları için uygulanmıştır. Bildiğimiz kadarı ile, Ka-bant uygulamaları için GaN tabanlı HEMT aygıtlarında MOCVD yeniden yöntemi kullanarak InGaN katmanlarının ve ALD yöntemi ile üretilen AZO katmanlarını omik kontak üretiminde uygulayan ilk grup biziz. MOCVD yöntemi ile üretilen InGaN tabakaları ve ALD yöntemi ile üretilen AZO tabakaları GaN malzemelerine omik kontak yapmak için oldukça önemli olan yüksek katkılama düzeyi ($>10^{19}\text{cm}^{-3}$) ve düşük tabaka direnci ($\sim 10^{-3}\ \Omega\cdot\text{cm}$) özelliklerini gösterdiler. Bu çalışmanın en önemli noktaları arasında: alaşımlı omik kontaklı HEMT ile karşılaştırıldığında, alaşımsız ve MOCVD yöntemi ile yeniden büyütülmüş InGaN ohmik kontakların $0.3\ \Omega\cdot\text{mm}$ 'ye kadar iyileştirilmiş kontak direnci yer almaktadır. Karşılaştırma amacı ile alaşımlı omik kontaklar farklı bariyer metali, farklı metal kalınlıkları ve farklı tavlama koşulları kullanılarak üretilmişlerdir. Ni bariyer metali kullanılarak üretilen HEMT yapılarında kontak direnci $0.41\ \Omega\cdot\text{mm}$ çıkış gücü ise $2.80\ \text{W}/\text{mm}$ olarak elde edilmiştir. Hem kaynak-akaç akımı (I_{ds}), hem transkondüktansta (g_m) hem de küçük sinyal performansında yaklaşık % 7'lik bir iyileşme gözlenmiştir. Transistör büyük sinyal ölçümleri, MOCVD yeniden büyütme yöntemi ile üretilen InGaN omik kontaklı HEMT aygıtların çıkış gücünün, alaşımlı ohmik kontaklı HEMT aygıtlara kıyasla % 9 artarak $3.07\ \text{W} / \text{mm}$ olduğu görülmüştür. ALD yöntemi ile üretilen omik kontaklarda ise ilk denemeler optimize edilmemiş girinti aşındırma ve plazma sonrası temizleme koşulları nedeniyle beklenen sonuçları vermedi.

Anahtar Kelimeler: AlGaN HEMT, MOCVD, Omik Kontak, Yüksek Frekans



To my honeys Derin & Eylül

and

my lovely wife, Filiz

ACKNOWLEDGMENTS

I would like to express my deepest gratitude to my supervisor, Assist. Prof. Dr. Bilge İmer for all her guidance, help, and patience in directing me through research on MOCVD of III-Nitrides and ALD films in the past years. Her trust in me has changed all my academic life.

It is a great pleasure to thank my co-supervisor Assoc. Prof. Dr. Alpan Bek for his guidance and comments.

I would like to thank the thesis monitoring committee members Prof. Dr. Burcu Akata Kurç, Prof. Dr. Hakan Ateş, Prof. Dr. Ekmel Özbay, Prof. Dr. Hüsnü Emrah Ünalın, and Assit. Prof. Dr. Bilge İmer for their precious comments.

I hereby present my sincere gratitude to Prof. Dr. Ekmel Ozbay for providing excellent working conditions and encouragement.

I would like to thank to group members; Yıldırım Durmuş, Gökhan Kurt, Doğan Yılmaz, Büşra Çankaya, Hülya Esen and İsmail Kabaçelik for their friendship and helps during my study. All of them calmed me down when I was stressed out, and they helped me sincerely when I was in trouble.

I owe my sincere gratitude and special thanks to Mustafa Öztürk from whom I learned various subjects.

Finally, I am indebted to my lovely wife, Filiz, for her continuous support and care.

This work is partially funded by the Scientific and Technological Research Council of Turkey under grant number 3170935.

TABLE OF CONTENTS

ABSTRACT	v
ÖZ	vii
ACKNOWLEDGMENTS	x
TABLE OF CONTENTS	xi
LIST OF TABLES	xiv
LIST OF ABBREVIATIONS	xx
LIST OF SYMBOLS	xxv
CHAPTERS	
1 INTRODUCTION	1
1.1 Backgrounds	1
1.2 III-Nitride Materials	4
1.2.1 Crystal Structure	7
1.2.2 Polarization in III-Nitrides	9
1.3 Advantages and Disadvantages of GaN	12
1.4 GaN for RF Applications	14
1.5 Research Aim	16
1.6 References	17
2 PROCESS TECHNOLOGIES FOR ALGAN/GAN HEMT	21
2.1 AlGaN/GaN HEMT Structure	21
2.2 Principle of HEMT	24
2.3 Semiconductor-Metal Contacts	30

2.3.1	Ohmic Contact to GaN	33
2.3.2	Schottky Contacts to GaN.....	39
2.4	References	41
3	COMPARISON OF ALLOYED AND NONALLOYED OHMIC CONTACTS IN ALGAN/GAN HEMTs.....	47
3.1	Ohmic Contacts to AlGa _N /Ga _N HEMTs	50
3.1.1	Varying Al Thicknesses.....	51
3.1.2	Alternative Barrier Metals	57
3.2	Non-Alloyed Recessed Ohmic Contacts to AlGa _N /Ga _N HEMTs	60
3.3	Fabrication of AlGa _N /Ga _N HEMT for Ka Band Applications.....	63
3.3.1	Device Description and Process Technology.....	63
3.4	DC Characterization of HEMT with Alloyed and Nonalloyed Ohmic Contacts.....	81
3.5	RF Characterization of HEMT with Alloyed and Nonalloyed Ohmic Contacts.....	84
3.6	Results and Discussions	89
3.7	References	93
4	ALD GROWTH OF ALUMINUM DOPED ZINC OXIDE (AZO) AS A NON-ALLOYED RECESSED OHMIC CONTACT FOR GAN HEMT STRUCTURES.....	97
4.1	ALD Growth of AZO Films.....	97
4.1.1	Initial ALD of AZO Trials	97
4.1.2	Optimization of AZO films for Non-Alloyed Ohmic Contacts	102
4.2	Non-Alloyed Recessed AZO Ohmic Contacts in Ga _N HEMTs	107
4.2.1	Side-Wall Issues	113

4.2.2	Effect of Post-Plasma Conditions.....	115
4.3	Results and Discussions.....	116
4.4	References.....	118
5	CONCLUSION AND FUTURE PLAN	121
5.1	Conclusions.....	121
5.2	Future Plan.....	123
5.3	References.....	125
	CURRICULUM VITAE.....	126



LIST OF TABLES

TABLES

Table 1.1 Material Properties for Common Semiconductors at 300K	3
Table 1.2 (continued)	4
Table 1.3 Common Semiconductor Material for RF Application [16].....	9
Table 1.4 Spontaneous Polarization (P_{SP}) in III-Nitrides affected by Lattice Non-Ideality	10
Table 1.5 Common Semiconductor Material for RF Applications	15
Table 2.1 Recent Progress for GaN-based HEMT Devices	30
Table 3.1 Ohmic Metal Stacks with varying Al Thicknesses and Corresponding Contact Features	53
Table 3.2 Ohmic Metal Stacks and Corresponding Contact Features	58
Table 3.3 Non-Alloyed Ohmic Contacts and Corresponding Contact Features	62
Table 3.4 GaN HEMT for K_a Band [12]	67
Table 3.5 TLM Results of Alloyed and Non-Alloyed Ohmic Contacts	77
Table 3.6 Comparison of Output Characteristics of HEMT with Alloyed and Non-Alloyed Ohmic Contacts	83
Table 3.7 Comparison of f_t and f_{max} for AlGaIn/GaN HEMT with Alloyed and Non-Alloyed Ohmic Contacts	87
Table 4.1 Summary of the AZO films grown at 200 °C and 225 °C.....	104
Table 4.2 Summary of the Samples for AZO Ohmic Contact Study	110
Table 4.3 Summary of the Deposition Details and Hall Measurement Results of AZO Samples for AZO Ohmic Contact Study.....	111
Table 5.1 Optimization of ALD of AZO ohmic contacts processes prior to HEMT device fabrication.....	124

LIST OF FIGURES

FIGURES

Figure 1.1. Lattice Constant and Bandgap Energies (E_g) of Common Semiconductor Materials [33].....	2
Figure 1.2. Wurtzite Unit Cell of GaN with Two Polarities. ‘Ga-Face’: Gallium Plane is on the Top of {0001} Plane and ‘N-Face’: Nitrogen Plane is on the top of {0001} Plane [34].....	5
Figure 1.3. Lattice Constant versus Bandgap of III-Nitrides (a), Band Structure of the AlInN/GaN Heterostructure (b) [35].....	6
Figure 1.4. Ga-Face Crystal Structure of Wurtzite GaN [36].....	8
Figure 1.5. Polarization in wurtzite GaN [34]	12
Figure 1.6. Electronic Application of GaN-based devices.....	14
Figure 2.1. Energy Bandgap of Two Semiconductor Before (a) and After Contact (b).....	22
Figure 2.2. Direction of P_{SP} and P_{PE} on different faces on GaN under strain [32]..	23
Figure 2.3. Ga-Polar of AlGaIn/GaN Heterostructure with direction of P_{SP} and P_{PE} (a) and 2DEG formation (b)	24
Figure 2.4. Cross-Section View of GaN-Based HEMT Structures 2D and 3D [2].	25
Figure 2.5. Energy Band Structure of GaN-based HEMT a) Zero bias and b) Negative bias [2].....	26
Figure 2.6. GaN-based HEMT Device Output Characteristics [34].....	27
Figure 2.7. Metal and n-type Semiconductor a) before and b) after contact where ϕ_m is greater than that of ϕ_s [69]	31
Figure 2.8. Metal and p-type Semiconductor a) before and b) after contact where ϕ_s is greater than that of ϕ_m [69]	33
Figure 2.9. Carrier transport mechanisms for lightly, moderate, and highly doped semiconductor/metal interface	35

Figure 2.10. Literature survey of Schottky Barrier Height for different metals as a function of Metal Work Functions [44]	37
Figure 2.11. Changing of contact resistivity with annealing condition a) [65] b) where individual studies were listed by G. Greco in his paper [44].....	38
Figure 3.1. Layer stacks of HEMT structure grown by MOCVD and corresponding 2DEG Properties	47
Figure 3.2. Schematic of patterned metal contacts with (a) TLM structure and measurement of (b) R-d curves with four-point probes [25]	48
Figure 3.3. Microfabrication Process Sequence for TLM Patterns	50
Figure 3.4. SEM images of a) deteriorated surface morphology of ohmic contacts due to high temperature annealing and b) acceptable ohmic contact morphology .	51
Figure 3.5. TLM Measurements of Ohmic Contacts with Different Al Thicknesses a) Contact resistance (R_c) and b) Sheet Resistivity (R_{sh}).....	55
Figure 3.6. TLM Measurements of Ohmic Contacts with Different RTA Conditions	57
Figure 3.7. TLM Measurements of Ohmic Contacts with Different Barrier Metal a) Contact resistance (R_c) and b) Sheet Resistivity (R_{sh}).....	59
Figure 3.8. a) Cross Section of device and b) Schematics of Band Diagram of Junction	60
Figure 3.9. TLM Measurements of Ohmic Contacts with Different Barrier Metal	61
Figure 3.10. Hall Effect Measurement of InGaN Layer Grown on Co-Laded Sapphire Substrate	62
Figure 3.11. Descriptive Process Flow for GaN HEMT with Alloyed and Non-Alloyed Ohmic Contacts	64
Figure 3.12. Microphotograph of a sample HEMT structure with S, D, and G contacts a) SEM image and b) FIB image	66
Figure 3.13. Structure of AlGaIn/GaN HEMT on 3'' SI-SiC by MOCVD.....	68
Figure 3.14. 2DEG Properties of HEMT on 3'' SI-SiC	69
Figure 3.15. a) Al composition and b) emission wavelength of AlGaIn Barrier layer of HEMT structure on 3'' SI-SiC	69

Figure 3.16. 2Theta-Omega Reflection of GaN HEMT on SI-SiC	70
Figure 3.17. a) Omega Scan of 002 and b) 102 reflection of GaN HEMT on SI-SiC	71
Figure 3.18. Schematic illustration of a) Alloyed and b) Non-Alloyed Ohmic Contacts.....	72
Figure 3.19. Microphotograph of Alloyed-Metal Contact Source and Drain a) before and b) after RTA Processes	73
Figure 3.20. Microphotograph of Non-alloyed-Metal Contact Source and Drain a) before and b) after MOCVD Re-Growth of InGaN	73
Figure 3.21. Hall Effect Measurement of Re-Growth InGaN Layer grown on co-loaded 3'' Al ₂ O ₃ substrate.....	74
Figure 3.22. Microphotograph of a) Non-alloyed-Metal Contact with Cr/Au metal and b) Mesa Isolation of Active Region	75
Figure 3.23. TLM measurement of a) Ti-Based alloyed ohmic contacts, b) MOCVD regrown InGaN non-alloyed ohmic contacts, and c) resistance versus contact spacing	76
Figure 3.24. Components of Total Contact Resistances, R _{c-tot} , of MOCVD regrown InGaN nonalloyed ohmic contacts	77
Figure 3.25. Ohmic contact patterns for MOCVD growth of InGaN on sapphire (a) and resistance versus contact spacing (b)	78
Figure 3.26. Microphotographs of 0.15μm Gate Foot patterned by Electron-Beam Lithography	79
Figure 3.27. Microphotographs of 0.15μm Gate Foot patterned by 2-steps of Electron-Beam Lithography.....	80
Figure 3.28. Microphotographs of a) Thickened Metal Pads and b) Air-Bridges by Electroplating Process.....	81
Figure 3.29. DC Characteristic of Alloyed and Non-Alloyed HEMT with L _g =0.15 μm (2x50 μm), S-D Spacing is 2.5 μm.....	82

Figure 3.30. Small Signal RF Performance of a) Non-Alloyed and b) Alloyed HEMT with $L_g=0.15 \mu\text{m}$ and S-D Spacing is $2.5\mu\text{m}$	85
Figure 3.31. Power Performance of a) Non-Alloyed and b) Alloyed $6 \times 75 \mu\text{m}$ HEMT with $L_g=0.15 \mu\text{m}$ and S-D Spacing is $2.5 \mu\text{m}$ at 35 GHz.....	88
Figure 4.1 Cross-section view of the AZO thin films grown by thermal ALD on silicon and quartz substrates.....	98
Figure 4.2 The atomic percentage of Zn, O, Al, C and Si elements, deposited at 200°C , as a function of depth from the surface as determined by depth-profiling XPS (left) and Al percentage of AZO thin films deposited at 160°C , 180°C , and 200°C (right).....	99
Figure 4.3 AFM micrograph for AZO thin films deposited at (a) 160°C , (b) 180°C and (c) 200°C and (d) RMS values.....	100
Figure 4.4 The transmission spectrum of AZO thin films (a) and Tauc Plot (b) ..	101
Figure 4.5 Room Temperature Hall Effect Measurement Results of AZO thin films; Carrier Concentration, Mobility and Resistivity with respect to deposition temperature.....	101
Figure 4.6. Cross-section view of the AZO thin films grown by thermal ALD on silicon and quartz substrates.....	103
Figure 4.7. SEM (a) and Stylus Profilometer image (b) of AZO thin films deposited at 200°C after wet etch with diluted HF: DI (1:100)	103
Figure 4.8 E_g of ALD grown AZO films with varying ZnO cycles grown at 200°C and 225°C	105
Figure 4.9 RT Hall Effect Measurement Result of AZO thin films a) Carrier Concentration and Mobility values and b) resistivity values	106
Figure 4.10 a) Cross Section of the device and b) Silvaco Simulations of $\text{In}_{0.12}\text{GaN}$ and c) AZO films	108
Figure 4.11 a) SEM Image of Recessed Samples with an etch depth of $\sim 88\text{nm}$ and b) Thickness of ALD of AZO measured by Stylus profilometer	109

Figure 4.12 SEM Image of Recessed a) AZO and b) Alloyed Metal Ohmic Contacts.....	111
Figure 4.13 TLM Measurement of Recessed Ohmic Contacts – ‘Control Sample’	112
Figure 4.14 Measurement of AZO Ohmic Contacts to GaN HEMT.....	113
Figure 4.15 a) SEM Image of Recessed Samples with an etch depth of ~88nm and b) Thickness of ALD of AZO measured by Stylus profilometer	114
Figure 4.16 Schematics of Photomask (PR) for recess etching of HEMT wafer a) Thick resist b) thinner resist	115
Figure 4.17 Schematic illustration of immobile negative charges under source and drain contacts.....	116

LIST OF ABBREVIATIONS

ABBREVIATIONS

2DEG	two-dimensional electron gas
AFM	atomic force microscopy
Al	aluminum
AlN	aluminum nitride
AlGaN	aluminum gallium nitride
Al ₂ O ₃	sapphire
ALD	atomic layer deposition
AZO	aluminum doped zinc oxide
Ar	argon
Au	gold
BHF	buffered hydrofluoric acid
BJT	bipolar junction transistor
Cl ₂	chlorine
Cu	copper
Cp ₂ Mg	bis cyclopentadienyl magnesium
DI	distilled water
DC	direct current
DH	double-hetero structure
EBL	electron beam lithography

FET	field effect transistor
FZ	float zone
Ga	gallium
GaAs	gallium arsenide
GaAsP	gallium arsenide phosphide
GaN	gallium nitride
Ga ₂ O ₃	gallium oxide
GaInAlN	gallium indium aluminum nitride
H ₂	hydrogen
HCl	hydrochloric acid
HEMT	high electron mobility transistor
HF	hydrofluoric acid
HFET	heterostructure field effect transistor
HR	high resistivity
HVPE	hydride vapor phase epitaxy
ICP	inductively coupled plasma
IGBT	insulated gate bipolar transistor
InGaAs	indium gallium arsenide
InGaP	indium gallium phosphide
InN	indium nitride
InGaN	indium gallium nitride
LED	light emitting diode

LNA	low noise amplifier
MAG	maximum available gain
MBE	molecular beam epitaxy
MEMS	micro electro mechanical systems
MESFET	metal semiconductor field effect transistor
Mg	Magnesium
MMIC	microwave monolithic integrated circuit
MOCVD	metal organic chemical vapor deposition
MODFET	modulation doped field effect transistor
N ₂	nitrogen
NH ₃	ammonia
NH ₄ OH	ammonium hydroxide
Ni	nickel
NiCr	nickel chromium
n.i.d	non intentionally doped
NL	nucleation layer
PA	power amplifier
PAE	power added efficiency
PECVD	plasma enhanced chemical vapor deposition
PL	photoluminescence
PMMA	polymethyl methacrylate
P _{PE}	piezo electric polarization

P _{SP}	spontaneous polarization
Pt	platinum
RF	radio frequency
RIE	reactive ion etching
RT	room temperature
RTA	rapid thermal annealing
SEM	scanning electron microscope
Si	silicon
SiC	silicon carbide
SiCl ₄	silicon tetrachloride
SiGe	silicon germanium
SiH ₄	silane
SiN	silicon nitride
SiO ₂	silicon dioxide
Ti	titanium
TLM	transfer length method
TMAI	trimethyl aluminum
TMGa	trimethyl gallium
TMIIn	trimethyl indium
UV	ultra violet
WBG	wide band gap
XPS	x-ray photoelectron spectroscopy

ZnO	zinc oxide
g_m	intrinsic transconductance
L_g	gate length
W_g	gate width
I_{ds}	drain-source current
f_t	max frequency
f_{max}	max frequency of oscillation
C_{gs}	gate-source capacitance
C_{gd}	gate-drain capacitance
R_{on}	on resistance
R_c	contact resistance
$R_{c-total}$	total contact resistance
R_i	channel resistance
R_g	gate resistance
R_s	source resistance
P_{out}	microwave output power
P_{in}	input power

LIST OF SYMBOLS

SYMBOLS

E_g	Band Gap
μ	mobility
N_s	carrier concentration
v_{sat}	saturation velocity
ϵ_r	carrier concentration
E_c	electrical breakdown field
κ	Thermal conductivity
a_o	lattice constant
c_o	lattice constant
e_x	in-plane stress component
e_y	in-plane stress component
e_z	in-plane stress component
σ	Conductivity
q	elementary charge
η_D	drain efficiency
ϕ_b	Schottky barrier height (SBH)
χ	Electron affinity

CHAPTER 1

INTRODUCTION

1.1 Backgrounds

Silicon (Si) has been utilized as a material of choice for a range of solid-state electronic devices since the birth of the first commercially available silicon transistor in the 1950s. The performance of a power electronics system depends on the operating frequencies and power levels. High switching rates and high breakdown voltages are necessary to have an efficient power electronic system.

Si-based technology has been leading the semiconductor industry for many decades. Increasing demand for electronic devices with higher efficiency operates at elevated powers, temperatures, and frequencies compared to the Si-based devices motivated intense research on new materials with larger bandgap and higher carrier mobility. Several different compound semiconductor materials have been investigated to overcome the limitation of silicon for different applications. For example, InP, GaAs, SiGe based transistors have been investigated and developed for RF applications with the frequency range from a few GHz to several hundred GHz due to their superior properties compared to Si [1-3].

Figure 1.1 shows the bandgap energies and lattice constants of common semiconductor materials. InP, GaAs, and SiGe have lower bandgap compared to III-N semiconductors such as GaN and AlGaN. III-Nitride materials and their alloys have a larger bandgap (E_g) which makes them better to be utilized at high power and high-temperature applications.

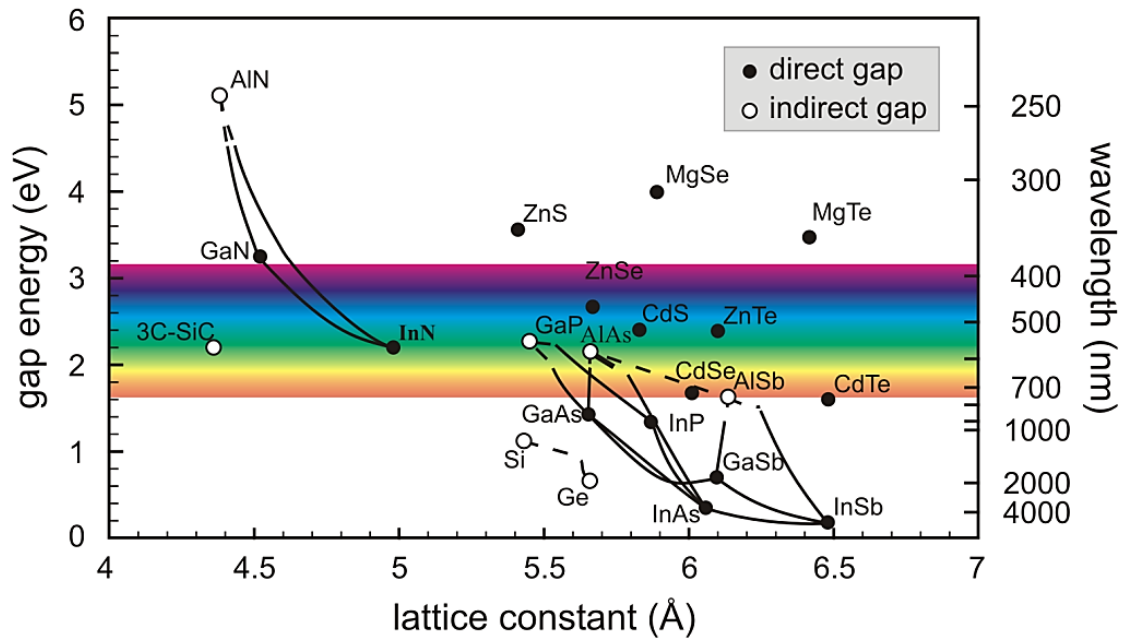


Figure 1.1. Lattice Constant and Bandgap Energies (E_g) of Common Semiconductor Materials [33]

Material properties of the common semiconductors are seen in Table 1.1. for comparison [4-6]. Higher operating voltages require a high electrical breakdown field (E_c) which means that the semiconductor should have larger bandgap energies (E_g). Additionally, it allows us to operate materials at elevated temperatures and provide radiation hardness. For high power and high-frequency operation, materials should have high charge carrier mobility (μ_n) and high saturation velocity (v_{sat}). In power electronics, thermal conductivities of the individual components are crucial. Semiconductors that are used in a power electronic system should have high thermal conductivities to remove dissipated heat through the active region. Failure of the device operation could happen due to poor thermal conductivity. Common semiconductors, like GaAs and InP, are poor thermal conductors which makes them not suitable for high-temperature applications compared to GaN. The relative permittivity (ϵ_r), which reflects the capacitive loading of a transistor, affects the transistor terminal impedances. Lower relative permittivity makes GaN enable 20% more currents and higher microwave output power.

GaN-based (GaN) based **H**igh **E**lectron **M**obility **T**ransistor (HEMT) devices, especially AlGaN/GaN devices, have had a great interest due to their unique material properties which makes them promising candidates for microwave power devices compared to Si and GaAs based devices. Wide bandgap (3.4 eV of GaN and 6.2 eV of AlN), high saturation electron drift velocity ($>2 \times 10^7$ cm/s) and large electrical breakdown strength ($>3 \times 10^6$ V/cm) are suitable for harsh environments. Due to high electron mobility and high critical breakdown field of GaN and high thermal conductivity of SiC, these material systems demonstrate high breakdown voltages, low loss, high-speed switching, and high operating temperatures compared to Si, GaAs, and InP material system. Low loss and high-speed features make GaN-based electronic devices to save energy and reduce the size of electronics. To be more specific, GaN-based devices are utilized in medium voltage applications [7].

Table 1.1 Material Properties for Common Semiconductors at 300K

Properties	GaN AlGaN/GaN	SiC	Diamond	Si	GaAs AlGaAs/ GaAs	InP InAlAs/ InGaAs
Band Gap Energy E_g (eV)	3.44	3.26	5.45	1.12	1.43	1.35
Electric Breakdown Field, E_c (MV/cm)	3.0	3.0	10.0	0.3	0.4	0.5
Saturated Electron Velocity, v_{sat} ($\times 10^7$ cm/s)	2.5	2.0	2.7	1.0	1.0	1.0
Electron Mobility, μ_n ($\text{cm}^2/\text{V}\cdot\text{s}$)	900 2000 ^x	700	4800	1500	8500 10000 ^y	5400 10000 ^z
2DEG Density, N_s ($\times 10^{13} \text{cm}^{-2}$)	1.0	N.A	N.A	N.A	<0.2	<0.2

Table 1.2 (continued)

Properties	GaN AlGa _x N _{1-x} /Ga N	SiC	Diamond	Si	GaAs AlGa _x As _{1-x} / GaAs	InP InAl _x As _{1-x} / InGaAs
Thermal Conductivity, κ (W.cm/K)	1.3 – 2.1	3.7- 4.5	22	1.5	0.5	0.7
Relative Permittivity, ϵ_r	9.0	10.1	5.5	11.8	12.8	12.5

x,y and z values for corresponding heterostructures

1.2 III-Nitride Materials

III-Nitride semiconductors such as aluminum nitride (AlN), gallium nitride (GaN), and indium nitride (InN) and their ternary and quaternary compounds which have wide bandgap (WBG) have a great potential for various semiconductor devices including optoelectronic devices (emitters and detectors) and high-temperature, high-power and high-frequency devices. At ambient conditions, hexagonal wurtzite structure is thermodynamically more stable which consists of two interpenetrating hexagonal close-packed lattices. III-Nitrides including GaN, InGa_xN_{1-x}, or AlGa_xN_{1-x} are grown by metalorganic chemical vapor deposition (MOCVD) or molecular beam epitaxy (MBE). Epitaxial films have typically [0001] orientation with the surface corresponding to Ga-face (Figure 1.2.) when they are grown by MOVPE. Ga-face exhibits a smoother surface compared to N-face GaN epitaxial films.

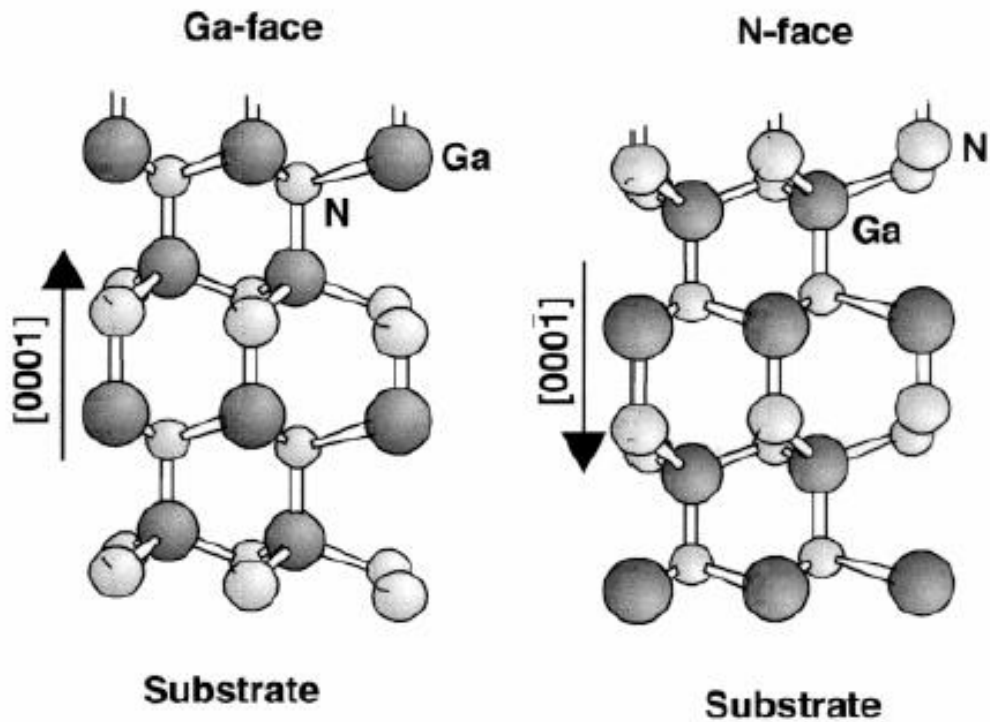


Figure 1.2. Wurtzite Unit Cell of GaN with Two Polarities. ‘Ga-Face’: Gallium Plane is on the Top of $\{0001\}$ Plane and ‘N-Face’: Nitrogen Plane is on the top of $\{0001\}$ Plane [34]

In cubic zinc-blende structure, which is symmetric and non-polar lattices, gathered great interest for optoelectronic devices. Besides, low temperature cubic form of GaN and InN have a direct bandgap, while AlN has an indirect bandgap. On the other hand, the application of electronic devices are based on hexagonal wurtzite crystal structures.

Room temperature band gap values of the III-Nitrides are 3.4 eV, 6.2 eV, and 0.7 eV for GaN, AlN, and InN, respectively. III-Nitrides are polar materials, with both piezoelectric and spontaneous polarization arising from strain and the high electronegativity of gallium and nitrogen atoms.

The polarization direction depends on the crystal orientation. The polarity of GaN depends on the substrate and, growth method, and growth conditions. Polarity plays

a vital role when considering the formation of defects during the material growth of heterostructure and influencing the final device performance.

Figure 1.3 shows the bandgap versus lattice constant of wurtzite III-N materials. The typical III-Nitride heterostructure includes a GaN buffer layer followed by growing a ternary or quaternary barrier layer. At the junction of the two crystal, the difference in polarization between GaN and ternary alloy (barrier layer) increase the carrier concentration in the electrically charged region. Due to the discontinuity of the conduction band at the boundary of two semiconductors, the electron diffusing from the ternary alloy into the GaN buffer layer is confined at the interface called two-dimensional electron gas (2DEG). The thickness of the ternary alloy barrier layer grown on the GaN buffer layer is typically tens of nm thick and has a wider bandgap than GaN, i.e. AlInN and AlGaN. The typical thicknesses of AlGaN are about 10-30 nm with an aluminum composition of about 20-40 %. The aluminum content of AlGaN layers determined by the tensile stress induced by lattice mismatch [32]. AlInN barrier layer, on the other hand, can be grown with 83 % Al composition and lattice match to GaN buffer layer. AlInN barrier layer exhibits large carrier density and hence higher output current densities and high thermal/chemical stability against harsh environments [8].

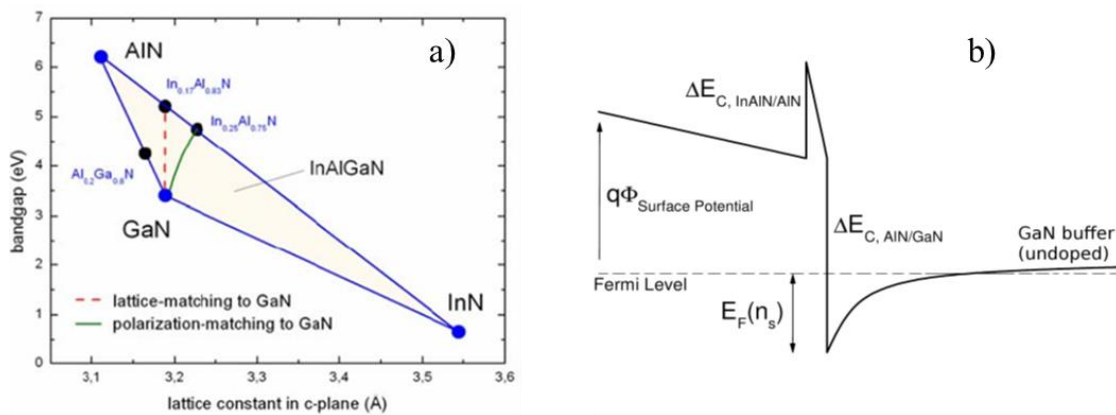


Figure 1.3. Lattice Constant versus Bandgap of III-Nitrides (a), Band Structure of the AlInN/GaN Heterostructure (b) [35]

There are remarkable electrical features of 2DEG in III-Nitrides materials. For example, $\text{Al}_{0.26}\text{GaN}/\text{GaN}$ heterostructures and lattice-matched AlInN/GaN heterostructures show a typical charge carrier concentration of $<1 \times 10^{13} \text{ cm}^{-2}$ and $<2 \times 10^{13} \text{ cm}^{-2}$, respectively. In general, the 2DEG carrier concentration of GaN-based heterostructures is 10 times higher compared to $\text{AlGaAs}/\text{GaAs}$ heterostructures. AlGaIn/GaN heterostructures with the highest electron velocity $3 \times 10^7 \text{ cm/s}$ and the mobility of $2000 \text{ cm}^2/\text{V} \cdot \text{s}$ have been reported [9], which are close to the theoretical simulations [10,11].

Thin native-oxide layers (Ga_2O_3 and Al_2O_3), formed on the top surface, are used as passivation layers and highlight the potential applications for electronic devices. Progress in material growth and microfabrication techniques have been accelerated by the intensive research in the field of optoelectronic device in past decades.

1.2.1 Crystal Structure

GaN has a wurtzite crystal structure that consists of alternating biatomic closely-packed planes of gallium and nitrogen pairs with ABAB sequence [12] see Figure 1.4. Choosing proper substrate and tuning epitaxial growth conditions can however result in metastable cubic zinc-blende structures. Most of the research is however focused on hexagonal wurtzite GaN structures due to the difficulties with the growth conditions of cubic GaN crystals.

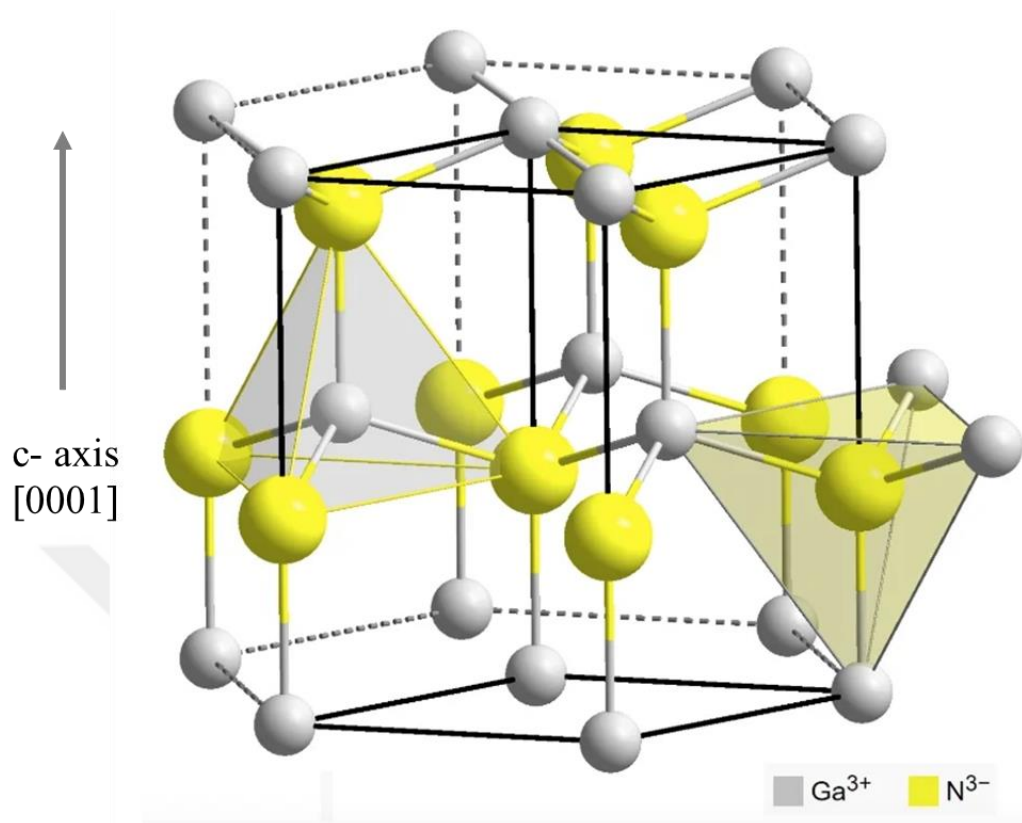


Figure 1.4. Ga-Face Crystal Structure of Wurtzite GaN [36]

The majority of all GaN studies are done on crystals grown along the c -axis ($\langle 0001 \rangle$ direction) which is called Ga-face polarity. Crystals grown in $\langle 000\bar{1} \rangle$ direction is called N-face polarity GaN. The definition of the polarity is coming from the Ga-N bonds parallel to the c -axis. In N-face GaN crystal, nitrogen atoms are below the Ga atoms, where Ga-face GaN has Ga atoms above nitrogen atoms.

The unit cell of wurtzite GaN is hexagonal with tetrahedrally bonded four atoms. The chemical bonds of III-Nitrides are predominantly covalent. There is no inversion symmetry in $\langle 0001 \rangle$ direction called the c -axis which means that the position of an atom with coordinates (x, y, z) is not invariant to the position $(-x, -y, -z)$.

Crystals with different polarity behave differently. For example, N-face crystals have lower crystal imperfections and can be etched chemically [13] whereas Ga-face

crystals have a smoother surface and chemically inert. Almost all HEMTs are based on Ga-face due to better electron transport properties [14].

Crystal parameters which are basal hexagon (a_0), the height of the hexagonal lattice cell (c_0), and the cation-anion bond length ratio (u_0) along with c-axis units of c_0 at 300K defines the wurtzite III-Nitride lattice are seen in Table 1.2. The subscript ‘ u_0 ’ indicates that the values belong to the lattice at the equilibrium state. An ideal wurtzite crystal exhibits a c_0/a_0 ratio of $\sqrt{\frac{8}{3}}=1.633$ and u_0 is 0.375 [15].

Table 1.3 Common Semiconductor Material for RF Application [16]

Parameter	Ideal	AlN	GaN	InN
a_0 (Å)	-	3.112	3.189	3.540
c_0 (Å)	-	4.982	5.185	5.705
c_0/a_0 (exp.)	-	1.601	1.626	1.612
c_0/a_0 (cal.)	1.633	1.619	1.634	1.627
u_0	0.375	0.380	0.376	0.377

1.2.2 Polarization in III-Nitrides

The nitrogen atom makes the GaN-based materials unique when considering GaAs-based and InP-based semiconductors due to its smallest size and highest electronegativity in group V elements. In this regard, nitrogen has a strong influence on the material properties of GaN. The electrons belong to the covalent bond affected

by the Coulomb forces of the nitrogen nucleus. This covalent bond has stronger ionicity compared to other III-V materials which result in polarization if the crystal has a lack of inversion symmetry.

As mentioned in section 1.2.1, wurtzite III-N materials do not possess inversion symmetry along the c-axis. Without having inversion symmetry and ionicity of metal-N bonds result in a strong polarization along the c-axis which is called ‘Spontaneous Polarization’ occurred in strain-free III-N lattice [16].

Not only the strong ionicity of covalent bonds but also crystal imperfections also affects the strength of spontaneous polarization. Spontaneous polarization in III-Nitride crystals induced by covalent bond along with $\langle 0001 \rangle$ direction. The other three covalent bonds in the crystal structure have equal ionicity and are aligned in opposite directions which are called compensation polarization. Compensation polarization act against the $\langle 0001 \rangle$ direction and causes a decrease in net spontaneous polarization. When the angle between these three bonds increases with decreasing c_a/a_o ratio results in a decrease in compensation polarization which increases net spontaneous polarization [17].

The magnitude of the net Spontaneous Polarization (P_{SP}) increases from GaN to AlN as shown in Table 1.3.

Table 1.4 Spontaneous Polarization (P_{SP}) in III-Nitrides affected by Lattice Non-Ideality

Parameter	Ideal	GaN	InN	AlN
c_o/a_o	1.633	1.626	1.612	1.601
PSP (C/m ²)	-	-0.029	-0.032	-0.081

Table 1.4 clearly shows that increasing crystal non-idealities PSP increases from GaN to AlN.

Due to the externally applied stress to the III-Nitride lattice, crystal parameters a_0 and c_0 change to manage applied stress. As a result, a change in polarization strength is observed. This additional polarization stress arising from strain is called 'Piezoelectric Polarization'.

Piezoelectric coefficient e_{33} and e_{31} are as follows; [18];

$$P_{PE} = e_{33} \varepsilon_Z + e_{31} (\varepsilon_X + \varepsilon_Y) \quad (\text{Eq. 1.1})$$

$\varepsilon_Z = (c - c_0) / c_0$: strain along c-axis,

$\varepsilon_X = \varepsilon_Y = (a - a_0) / a_0$: in-plane strain

a_0 and c_0 are lattice constants at equilibrium. It is assumed that the in-plane strain is isotropic. The relation between different strains;

$$\varepsilon_Z = -2 \frac{c_{13}}{c_{33}} \varepsilon_X \quad (\text{Eq. 1.2})$$

c_{13} and c_{33} are elastic constants and the following equation yields Piezoelectric Polarization with the help of using Eq.1.1 and Eq.1.2

$$P_{PE} = 2 \cdot \frac{a - a_0}{a_0} \left(e_{31} - e_{33} \frac{c_{13}}{c_{33}} \right) \quad (\text{Eq. 1.3})$$

In III-N semiconductor materials the term $(e_{31} - e_{33} \frac{c_{13}}{c_{33}})$ is always be negative since the coefficients e_{31} , e_{33} , and c_{13} are always negative, positive, and positive, respectively. This means that the layers under tensile stress ($a > a_0$) has a negative P_{PE} and the layers under compressive stress ($a < a_0$) has a positive P_{PE} .

Lacking of inversion symmetry in III-N crystal structures leads to a strong electric dipole in each of unit cells along $\langle 0001 \rangle$ direction, see Figure 1.5 (a). The net polarization in III-Nitrides is compensated and a net sheet charge on the top and bottom surface of the layer, see Figure 1.5. (b) [19].

The spontaneous polarization (P_{SP}) is always negative in III-Nitrides which means that P_{SP} and P_{PE} are parallel for layers under tensile stress and anti-parallel for layers under compressive stress [20]. Figure 1.5. shows that strain-induced piezoelectric effect can be used to tune total polarization in the material. The magnitude of the polarization effect in III-Nitride materials is much greater than other common III-V materials such as GaAs and InP [16].

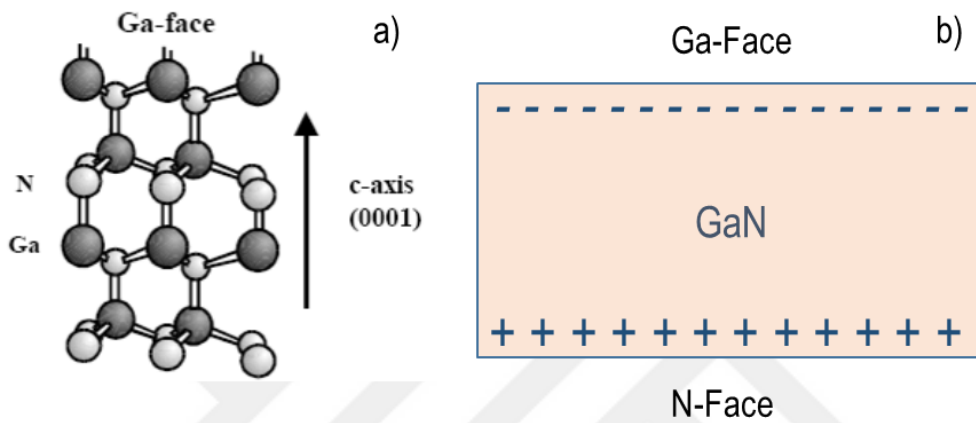


Figure 1.5. Polarization in wurtzite GaN [34]

1.3 Advantages and Disadvantages of GaN

Table 1.1 shows the material properties of common semiconductor materials used in electronics such as GaAs, SiC, GaN, Si, and InP. For electronic applications, wide bandgap (WBG) semiconductors along with high breakdown voltage and high electron velocity make them unique for high-power and high-frequency applications that cannot be realized in the other materials system listed in Table 1.1.

The thermal properties of GaN-based devices are another superior property compared to counterparts. Having higher thermal conductivity of GaN enables them to dissipate power more easily and allows devices to operate with having less degradation compared to GaAs and InP-based devices.

High saturation velocity (v_{sat}) and high charge carrier mobility (μ_n) are desirable when considering a high-frequency and high current operation. When comparing GaAs and InP material system GaN-based transistor suffers from lower mobility. These lower values, on the other hand, are adequate for transistors operating at high power conditions. Although GaN is suffering from low mobility, it has higher saturation velocity and wider bandgap which makes them convenient materials operating at a higher frequency and higher power applications compared to other common semiconductor materials. The drawback of the GaN is having difficulties in finding large wafers and the high cost of the GaN substrates.

There are several figures of merits that have been proposed to make the comparison clearer. These figures of merit utilize the most important material properties considering high-frequency and high-power applications into a number that reflects the relative strength of each semiconductor material. For instance, the Johnson's Figure of Merit (JFOM) takes in to account the saturated electron velocity and breakdown voltage to define a number for a certain semiconductor for high-frequency handling capability [21]. The JFOM for GaN is 93 times compared to GaAs and 728 times compared to Si. Another figure of merit that defines high-power handling capability is Beliga's Figure of Merit (BFOM) is calculated considering electron mobility, relative permittivity, and electric breakdown field [22]. The BFOM for GaN is 11 times compared to GaAs and 133 times compared to Si. JFOM and BFOM clearly show that GaN offers much better performance for high-frequency and high-power applications compared to both Si and GaAs.

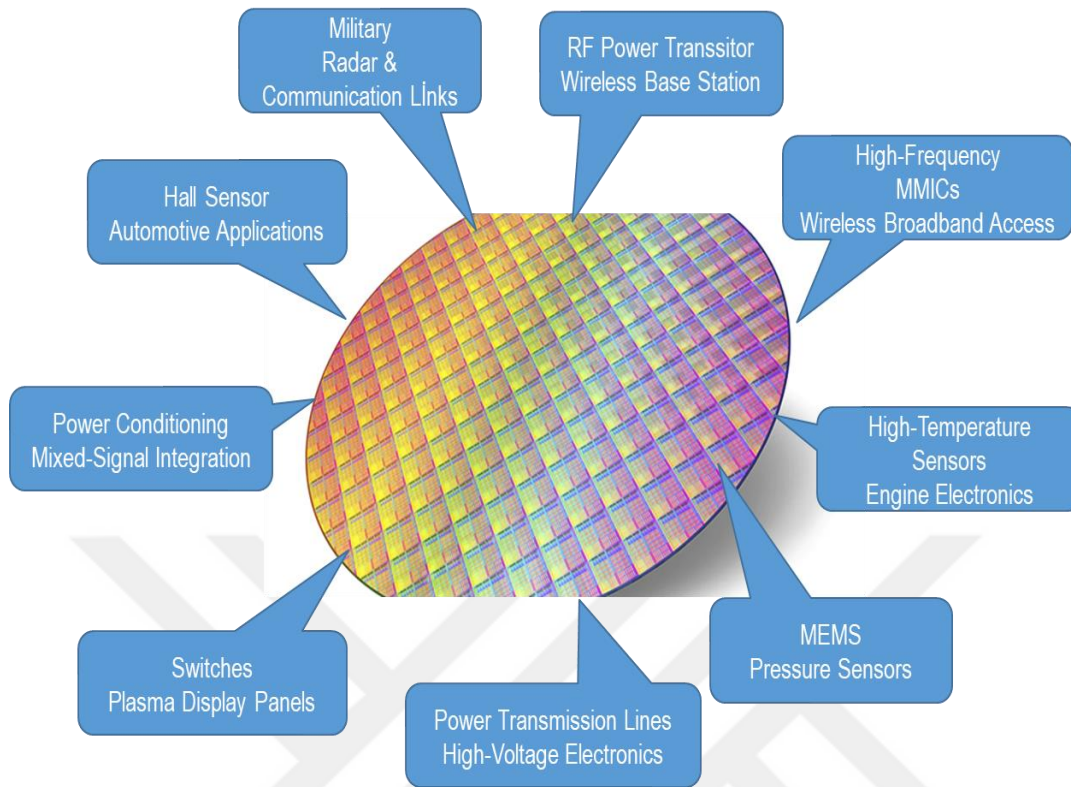


Figure 1.6. Electronic Application of GaN-based devices

1.4 GaN for RF Applications

Energy saving is still the most important concern in recent technologies which implies that high power efficiency and low power loss are detrimental for power devices [23]. Utilizing better materials to develop efficient power devices in modules is an effective way of saving energy. In this respect, power efficiency is vital in RF applications where a large amount of data with high speed and accuracy. For instance, 5G mobile communication needs much bigger data traffic with fast to transmit and receive which requires low loss and low energy consumption [24]. RF module is the main component that consumes a large amount of energy by releasing a large amount of heat.

GaN has a large bandgap (3.4 eV) and high saturation velocity (2.5×10^7 cm/s) which makes it a suitable material for transistors that operates at high-frequency and high

voltage operation compared to common semiconductor materials [25,26]. Si-based transistor devices have been using at low-frequency (<3 GHz). GaAs and InP-based devices can be used at higher frequencies with low operation voltages. Low breakdown fields of these materials limits their RF performances, output powers, and operating voltages. GaN-based transistors show comparable frequency gain at high operation voltage which results in high output power. Unique material properties and outstanding performance of GaN devices make them be utilized in a wide range of RF applications. GaN-based RF devices already have been using in base stations and military applications [27,28]. Although each semiconductor material has more or less suitable, GaN-based transistors can be applied to various applications in different frequencies.

The superior power density of GaN, compared to Si LDMOS, helps wide band gap technology to dominate the RF power devices market. Depending on the bandwidth and power density not only AlGaN/GaN heterostructure but also AlN/GaN, AlInGaN/GaN and, AlInN/GaN alloys can be utilized which shows higher electron mobility due to the large polarization [29,30].

Common semiconductors for suitable RF application are listed in Table 1.4 below [31].

Table 1.5 Common Semiconductor Material for RF Applications

Material	Radar	Military	Wireless	Optical	Wired Broadband
Si	High Peak Power	High Power, High Linearity			
SiGe	Low Noise, High Frequency, High Integration		Low Noise, High Frequency, High Integration	High Speed, Low Noise, High Integration	High Integration
GaAs	Low Noise, High Frequency,	Low Noise, High Frequency,	Low Noise, High Frequency, High Linearity	High Voltage, Low Power, High Linearity	High Linearity

Table 1.5 (continued)

Material	Radar	Military	Wireless	Optical	Wired Broadband
InP				High Speed, High Voltage, Low Power	
GaN	High Frequency, High Power, High Efficiency	High Frequency, High Power, High Efficiency	High Frequency, High Power, High Efficiency		High Linearity, High Efficiency

1.5 Research Aim

Due to its unique material properties, GaN is the most powerful alternative for devices designated at higher power, higher temperature, and higher frequency RF applications. One of the biggest advantages of GaN is the possibility of growing AlGaN/GaN heterostructures which yield high 2DEG density with high electron drift mobility.

In this work, we aimed to develop methods of creating ohmic contacts, which does not require high-temperature annealing of metal stacks, called non-alloyed ohmic contacts for AlGaN/GaN HEMT devices designated for Ka-Band applications. MOCVD regrown InGaN layers and ALD grown AZO films were utilized as non-alloyed ohmic contacts.

The final goal of this research was to optimize alloyed ohmic contacts, develop MOCVD grown of InGaN layers and ALD grown of AZO films as non-alloyed ohmic contacts for GaN-based HEMTs for K_a-band applications. Detailed comparison of GaN-based HEMTs for K_a-band applications with alloyed and non-alloyed ohmic contacts was systematically investigated.

1.6 References

- [1] I. Angelov, L. Bengtsson, and M. Garcia, "Extension of the Chalmers Nonlinear HEMT and MESFET Model," *IEEE transactions on microwave theory and technique*, vol. 44, no. 10, pp. 1664-1674, Oct 1996.
- [2] Thin Film Substrates: Thin Film Design Guide for RF and UWave Substrates," Vishay.
- [3] J. Joh, J. A. del Alamo, U. Chowdhury, T.-M. Chou, H.-Q. Tserng, and J. L. Jimenez, "Measurement of Channel Temperature in GaN High-Electron Mobility Transistors," *IEEE Transactions on Electron Devices*, vol. 56, no. 12, pp. 2895-2901, Dec 2009.
- [4] R. T. Kemerley, H. B. Wallace, and M. N. Yoder, "Impact of wide bandgap microwave devices on DoD systems," *Proceedings of the IEEE*, vol. 90, pp. 1059-1064, June 2002.
- [5] L. M. Tolbert, B. Ozpineci, S. K. Islam, and M. S. Chinthavali, "Wide bandgap semiconductors for utility applications," in *Proc. Power and Energy Systems*. ACTA Press, USA, Feb. 2003.
- [6] R. J. Trew, "SiC and GaN transistors- Is there one winner for microwave power applications?" *Proceedings of the IEEE*, vol. 90, pp. 1032-1047, June 2002.
- [7] D.H. Kim, "Design and Fabrication of AlGaIn/GaN on Si FETs for Ka Band MMICs", PhD Thesis, Graduate School of Electrical and Computer Engineering Seoul National University, 2018
- [8] F. Medjdoub, J. Carlin, M. Gonschorek, E. Feltin, M. A. Py, D. Ducatteau, C. Gaquière, N. Grandjean, and E. Kohn, "Can InAlN/GaN be an alternative to high power/high temperature AlGaIn/GaN devices?" in *IEDM*, pp. 1-4, 2006.
- [9] R. Gaska, J. W. Yang, A. Osinsky, Q. Chen, M. A. Khan, A. O. Orlov, G. L. Snider, and M. S. Shur, "Electron transport in AlGaIn/GaN heterostructures grown on 6H-SiC substrates," *Applied Physics Letters*, vol. 72, no. 6, pp. 707-709, 1998.
- [10] B. E. Foutz, L. F. Eastman, U. V. Bhapkar, and M. S. Shur, "Comparison of high field electron transport in GaN and GaAs," *Applied Physics Letters*, vol. 70, no. 21, pp. 2849-2851, 1997.
- [11] J. D. Albrecht, R. P. Wang, P. P. Ruden, M. Farahmand, and K. F. Brennan, "Electron transport characteristics of GaN for high temperature device modeling," *Journal of Applied Physics*, vol. 83, no. 9, pp. 4777-4781, 1998.
- [12] H. Morkoc, "Nitride Semiconductors and Devices," Springer, New York, 1999.
- [13] J.L.Weyher, P.D. Brown, A.R.A. Zauner, S. Müller, C.B. Boothroyd, D.T. Ford, P.R. Hageman, C.J. Humphreys, P.K. Larsen, I. Grzegory, and S. Porowski, "Morphological and Structural Characteristics of Homoepitaxial GaN Grown by

- Metalorganic Chemical Vapour Deposition (MOCVD)," *Journal of Crystal Growth*, vol. 204, no. 4, p. 419, 1999.
- [14] O. Ambacher, J. Smart, J.R. Shealy, N.G. Weimann, K. Chu, M. Murphy, W.J. Schaff, L.F. Eastman, R. Dimitrov, L. Wittmer, M. Stutzmann, W. Rieger, and J. Hilsenbeck, "Two-Dimensional Electron Gases Induced by Spontaneous and Piezoelectric Polarization Charges in N- and Ga-face AlGa_N/Ga_N Heterostructures," *Journal of Applied Physics*, vol. 85, no. 6, p. 3222, 1999.
- [15] J. I. Pankove and T. D. Moustakas, *Gallium Nitride (GaN) I*. San Diego: Academic Press, 1998, ISBN 0-12-752158-5.
- [16] F. Bernardini, V. Fiorentini, and D. Vanderbilt, "Spontaneous polarization and piezoelectric constants of III-V nitrides," *Phys. Rev. B*, vol. 56, no. 16, pp. R10-024-R10-027, Oct. 1997.
- [17] M.C.J.C.M Krämer, 'Gallium Nitride-based Microwave High-Power Heterostructure Field-Effect Transistors' PhD Thesis, Technische Universiteit Eindhoven, October 2006
- [18] J. I. Pankove and T. D. Moustakas, *Gallium Nitride (GaN) I*. San Diego: Academic Press, 1998, ISBN 0-12-752158-5.
- [19] P.S. Park, "PhD Thesis, University of California Santa Barbara (UCSB), December 2006
- [20] X.-G. He, D.-G. Zhao, and D.-S. Jiang, "Formation of twodimensional electron gas at AlGa_N/Ga_N heterostructure and the derivation of its sheet density expression," *Chinese Physics B*, vol. 24, no. 6, Apr 2015.
- [21] E. O. Johnson, "Physical limitations on frequency and power parameters of transistors," *RCA Review*, vol. 26, pp. 163-177, 1965.
- [22] B. J. Baliga, "Semiconductors for high-voltage, vertical channel FET's," *J. Appl. Phys.*, vol. 53, pp. 1759-1764, 1982.
- [23] J. A. Cooper, JR., and A. Agarwal, "SiC Power-Switching Devices- The Second Electronics Revolution?" *Proceedings of the IEEE*, vol. 90, no. 6, pp. 956-968, 2002.
- [24] T. Kaneko, S. Kazumi, and K. Kunihiro, "Ga_N HEMT High Efficiency Power Amplifier for 4G/5G Mobile Communication Base Stations," *Proceedings of Asia-Pacific Microwave Conference*, pp. 994-997, Nov 2014.
- [25] U. K. Mishra, L. Shen, T. E. Kazior, and W. Yi-Feng, "Ga_N-Based RF Power Devices and Amplifiers," *Proceedings of the IEEE*, vol. 96, no.2, pp. 287-305, 2008.
- [26] S. Mudassir and J. Muhammad, "A Review of Gallium Nitride (Ga_N) based devices for High Power and High Frequency Applications," *Journal of Applied and Emerging Sciences*, vol. 4, no. 2, pp. 141-146, 2013.

- [27] C. Campbell, A. Balistreri, M.-Y. Kao, D. Dumka, and J. Hitt, "GaN Takes the Lead," *IEEE Microwave Magazine*, vol. 13, no. 6, pp. 44- 53, 2012.
- [28] S. Rajan and D. Jena, "Gallium nitride electronics," *Semiconductor Science and Technology*, vol. 28, no. 7, 2013.
- [29] R. Wang et al., "Quaternary Barrier InAlGaN HEMTs With f_T/f_{max} of 230/300 GHz," *IEEE Electron Device Letters*, vol. 34, no. 3, pp. 378-380, 2013.
- [30] G. Li et al., "Two-dimensional electron gases in strained quantum wells for AlN/GaN/AlN double heterostructure field-effect transistors on AlN," *Applied Physics Letters*, vol. 104, no. 19, 2014.
- [31] D.H. Kim, "Design and Fabrication of AlGaN/GaN on Si FETs for Ka Band MMICs", PhD Thesis, Graduate School of Electrical and Computer Engineering Seoul National University, 2018
- [32] K. Kubota, Y. Kobayashi, and K. Fujimoto, "Preparation and properties of III-V nitride thin films," *Journal of Applied Physics*, vol. 66, pp. 2984–2988, 1989.
- [33] H. Ibach and H. Lueth. *Solid-State Physics*. Springer Verlag, 2003
- [34] Li, Xiao and X. Liu. "Group III nitride nanomaterials for biosensing." *Nanoscale* 9 22 (2017): 7320-7341
- [35] J.F.Charlin et al, *Progresses in III-Nitride Distributed Bragg Reflectors and Microcavities Using AlInN/GaN Materials*, ISBN: 978-3-527-40561-9
- [36] https://en.wikipedia.org/wiki/Gallium_nitride



CHAPTER 2

PROCESS TECHNOLOGIES FOR ALGAN/GAN HEMT

2.1 AlGaN/GaN HEMT Structure

Device operation in this thesis is based on the properties of heterostructures. A heterostructure could be formed by using two semiconductors having different energy bandgap (E_g), permittivities (ϵ_r), work functions (Φ_s), electron affinity (χ_s). Figure 2.1 shows the energy band diagram of semiconductors with different material properties.

After making contact with wide and narrow bandgap semiconductors, a discontinuity in the conduction band and valance band is observed. A quantum well is formed at the boundary which is called Two-Dimensional Electron Gas (2DEG) due to discontinuity at the conduction band. Increasing doping of wide bandgap semiconductor causing separation of electrons from donor atoms and collected as 2DEG channel under heterointerface.

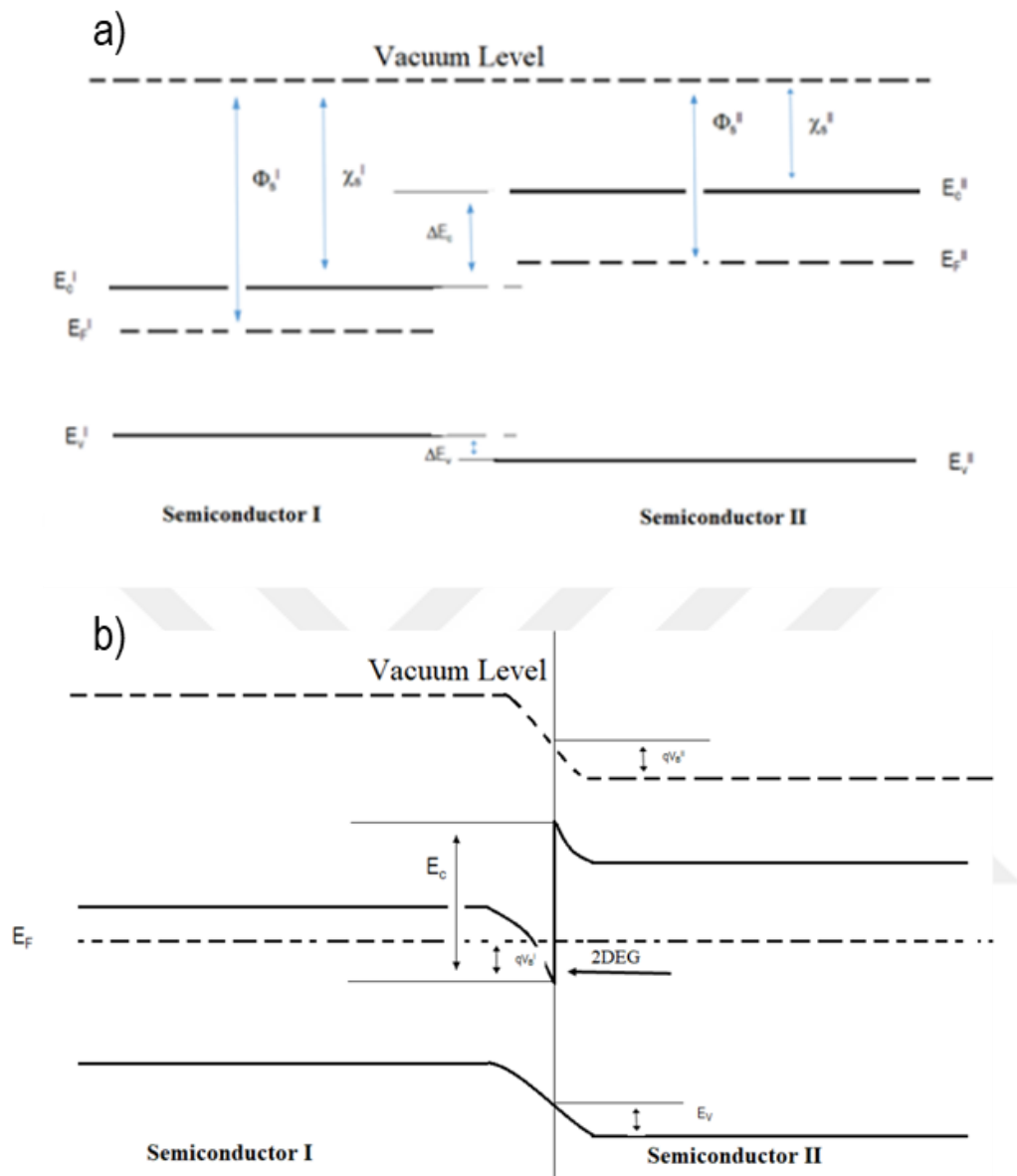


Figure 2.1. Energy Bandgap of Two Semiconductor Before (a) and After Contact (b)

Apart from other III-V semiconductor materials where doping is crucial to induce 2DEG, the AlGa_N/Ga_N heterostructure does not need any doping which means that 2DEG is induced without having any kind of doping. 2DEG is created in AlGa_N/Ga_N heterostructure with the help of spontaneous and piezoelectric polarization which produces very high electron concentration even without having

doping. Doping free mechanism also decreases trap related phenomenon in device performance.

These devices are typically used by forming heterostructure with epitaxial growth of GaN followed by an AlGaN layer results in 2DEG created at the junction in the GaN side.

The effect of strain and growth face on the direction of piezoelectric and spontaneous polarization in III-Nitride heterostructures are seen in Figure 2.2, below.

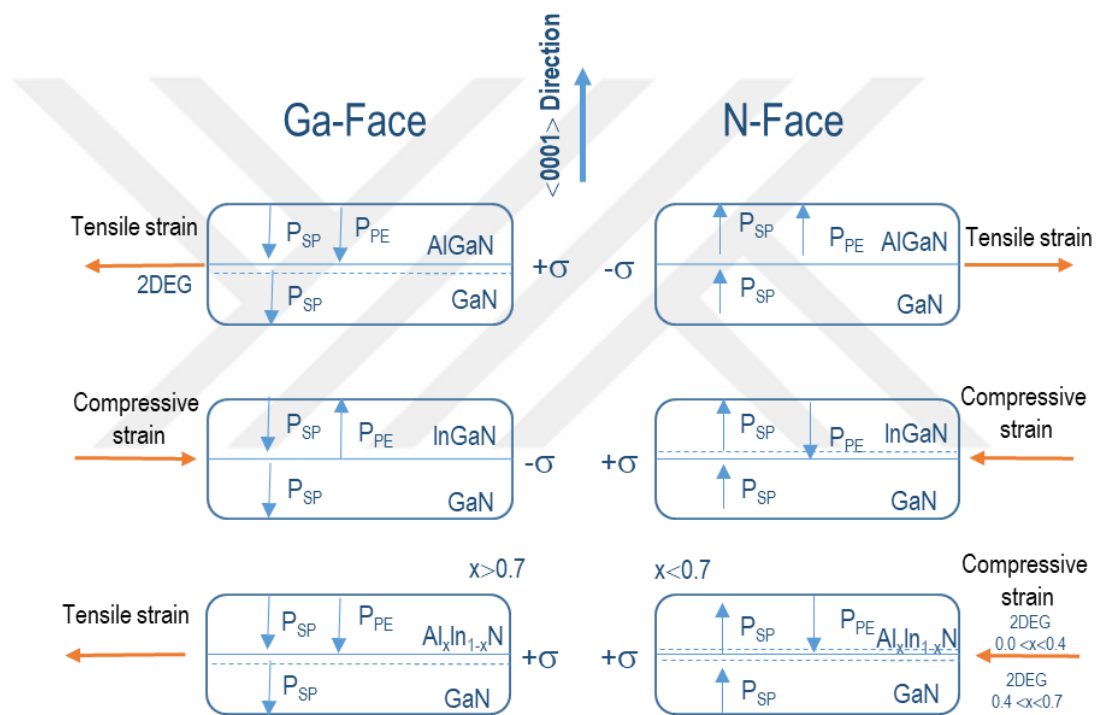


Figure 2.2. Direction of P_{SP} and P_{PE} on different faces on GaN under strain [32]

A relatively thin AlGaN barrier layer on the top of a high resistive GaN layer to create an AlGaN/GaN heterostructure. Due to the differences in bandgap energies band bending occurs and 2DEG created by electrons in the upper side of the GaN layer. Having lack of inversion symmetry in $\langle 001 \rangle$ direction and large ionicity of covalent bond in wurtzite crystal induces a strong spontaneous polarization (P_{SP}) in $\langle 001 \rangle$ direction. Because of the lattice parameter differences, piezoelectric

polarization (PPE) occurs in III-Nitrides which is much larger than traditional III-V semiconductors.

Figure 2.3. below shows the direction of polarization and band diagram of Ga-polar AlGaN/GaN heterostructure. 2DEG is created at the junction in the very top side of the GaN buffer layer.

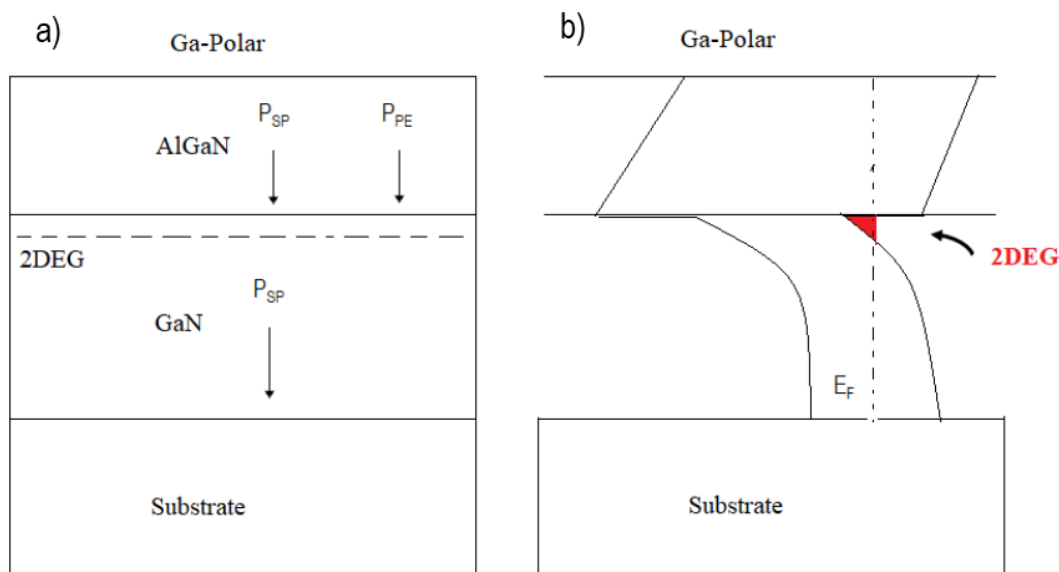


Figure 2.3. Ga-Polar of AlGaN/GaN Heterostructure with direction of P_{SP} and P_{PE} (a) and 2DEG formation (b)

The effects of polarization in III-Nitride are large and it generates 2DEG without any doping. The maximum electron density for such a structure could reach up to about $2 \times 10^{13} \text{ cm}^{-2}$. High electron mobility up to $2000 \text{ cm}^2/\text{V} \cdot \text{s}$ at 300K (77K) is achieved in the 2DEG channel [2].

2.2 Principle of HEMT

The High Electron Mobility Transistor (HEMT) which is also called Modulation Doped Field Effect Transistor (MODFET) gained much interest in high-frequency and high power devices. HEMT is a three-terminal device. The cross-section and

geometry of a typical HEMT structure are seen in Figure 2.4. The current flowing between the drain (D) and source (S) is controlled by applying a voltage to the gate (G) terminal as seen in Figure 2.5. The quality of the 2DEG channel determines the electron transport along with the interface and properties of the final device. 2DEG quality is depending on both substrate, growth method, doping level, and purity of sources that are used for epitaxial growth.

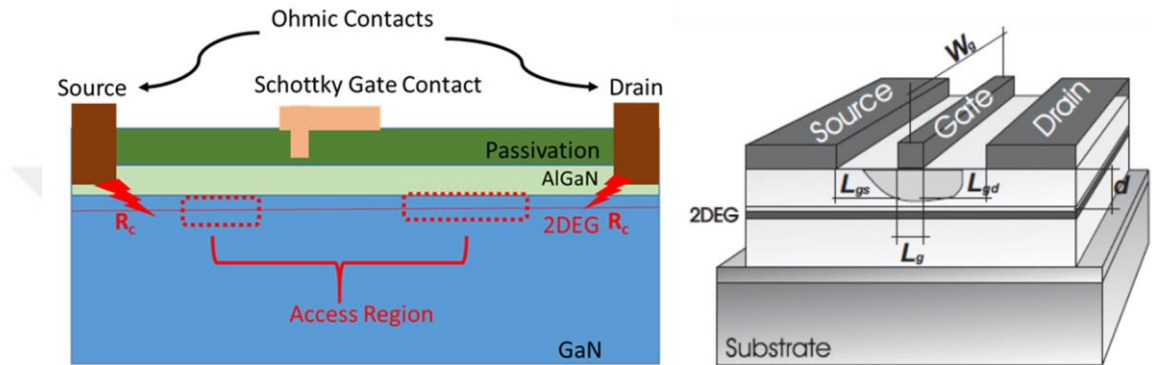


Figure 2.4. Cross-Section View of GaN-Based HEMT Structures 2D and 3D [2]

The 2DEG conductivity is given by [12];

$$\sigma = qn_s\mu \quad (\text{Eq. 2.1})$$

where q is the elementary charge of the electron, n_s is the electron concentration and μ is the mobility of electrons. Channel conductivity of the heterostructure is governed by both mobility and carrier concentration.

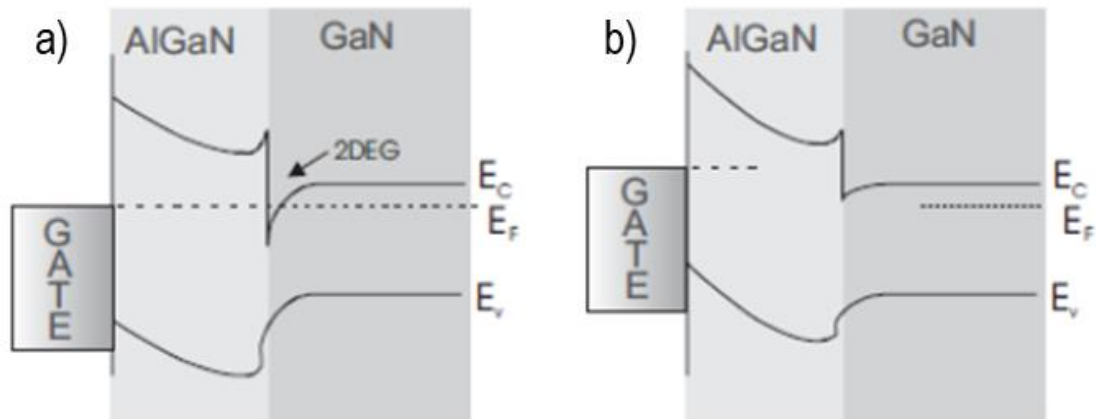


Figure 2.5. Energy Band Structure of GaN-based HEMT a) Zero bias and b) Negative bias [2]

When a positive voltage is applied to the drain contact leads to the flow of current along 2DEG due to the potential drop between drain and source contact. The amount of the current flowing through the source and drain contact is controlled by the gate voltage, V_g . Increasing the gate voltage to higher negative values cause to decrease in the drain current. Further increasing V_g to more negative values cause to channel pinched-off which is called pinch-off voltage.

An electron can flow between the source and drain contact for a certain V_g value above the pinch-off voltage. The saturation drain-source current, I_{DSS} , is defined as the maximum saturation current passing through drain and source ohmic contacts

Typical output characteristics and dependence of I_{DSS} on applied voltage (V_{DS}) of a GaN-based HEMT device is shown in Figure 2.6 below.

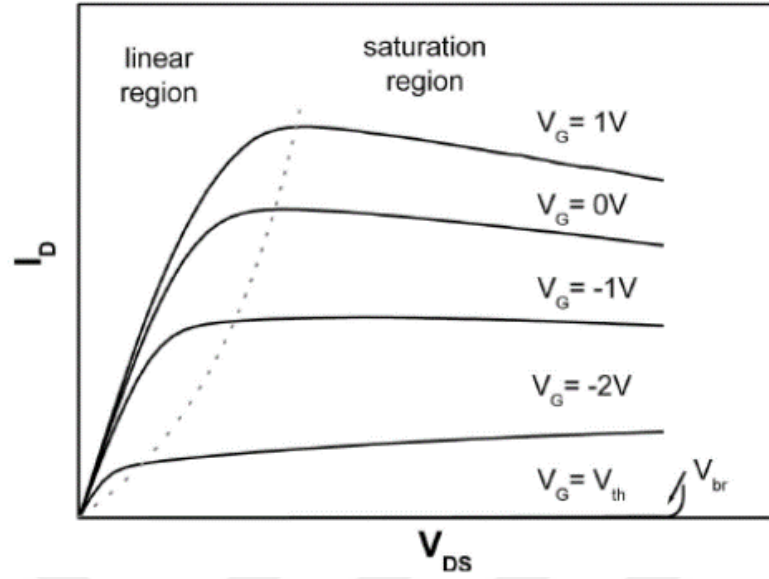


Figure 2.6. GaN-based HEMT Device Output Characteristics [34]

The gate width (W_g) and the gate length (L_g) are the most important physical parameters of the HEMT devices. Other important parameters of the HEMT device is the gate-source distance (L_{GS}) and gate-drain distance (L_{GD}). L_g is crucial in determining the operating frequency and the current flowing through the device depends on the W_g [13]. As a result, narrow gate-width (W_g) devices are utilized for low current and low noise applications whereas the wide gate-width (W_g) is utilized for high power electronic devices.

Some important quantities for electrical characterization of HEMT devices are the saturation current, g_m is the transconductance, f_i is the current gain frequency and the f_m is the maximum oscillation frequency. The output characteristics I_D is a function of V_{DS} and V_{GS} . I_D is proportional to the channel with W_g so that the unit is mA/mm .

$$g_m = \frac{\partial I_D}{\partial V_{GS}} \quad (\text{Eq. 2.2})$$

$$g_{m,ext} = \frac{g_m}{1 + g_m R_s} \quad (\text{Eq.2.3})$$

where g_m is the intrinsic transconductance, R_s is the source resistance which is the sum of the sheet resistance between gate and source contact ($R_{sh,gs}$) and R_c [14].

$$I_{ds} \propto \frac{W_g}{L_g} \quad (\text{Eq.2.4})$$

where W_g and L_g are gate width and gate length, respectively[14].

$$f_t = \frac{v_{sat}}{2\pi L_g} = \frac{g_m}{2\pi(C_{gs}+C_{gd})} \quad (\text{Eq.2.5})$$

where v_{sat} is the electron saturation velocity[14].

$$f_{max} = \frac{f_t}{2\sqrt{2\pi f_t R_g C_{gd} + G_{ds} R_{in}}} \quad (\text{Eq.2.6})$$

where C_{gs} is the gate-source capacitance, C_{gd} is the gate-drain capacitance, G_{ds} is the output conductance, R_g is the gate resistance, R_{in} is the input resistance consisting of the gate, source, and channel components[14].

The first AlGaIn/GaN HEMT was reported by Khan in 1994 [15]. The gate length (L_g) was 0.25 μm exhibited a current I_{DSS} of about 60 mA/mm with a transconductance (g_m) of 27 mS/mm and without any reported microwave performance. Later on, Aktaş [16] et al. reported a device with an L_g of 3 μm and W_g of 40 μm that exhibits an I_{DSS} of about 500 mA/mm with a transconductance of 120 mS/mm on the doped structure [38]. The first power data for AlGaIn/GaN HEMT were reported for a 30 nm thick $\text{Al}_{0.15}\text{GaIn}$ barrier on a thin buffer at UCSB [17]. The power density was 1.1 W/mm with a power-added efficiency (PAE) of 18.6% was obtained at 2 GHz. It was found that output power was limited by heating which results in poor electron transport in the 2DEG channel due to the lower crystal quality. Increasing GaN buffer thickness to 2-3 μm and barrier layer up to 40 nm improved the power density up to 1.57 W/mm at 4GHz [18]. The power performance of $\text{Al}_{0.5}\text{GaIn}$ HEMT with an L_g of 0.25 μm was investigated. An increase in output power was observed from 0.35 W to 1 W at 8 GHz but the power density decreased from 3.3 W/mm to 2 W/mm due to heating effects of the larger device when increasing W_g from 100 μm to 500 μm [19].

Both DC and RF performance of GaN-based devices continue to be improved due to the betterments in both qualities of the materials and microfabrication techniques [20]. High-performance AlGa_N HEMT on sapphire with a gate length of 0.25 μm and transconductance of 400 mS/mm have been reported with f_T of 85 GHz and f_{max} of 151 GHz [21]. To decrease the self-heating effect and improve device performance, several reports have been published on high resistivity SiC substrates [22-23]. HEMT devices on a SiC substrate with an L_g of 0.12 μm yielded an extrinsic transconductance of 217 mS/mm and a current density up to 1.19 mA/mm where the cutoff frequency was 101 GHz and maximum oscillation frequency was 155 GHz [24]. Power densities of 13.8 W/mm at 2 GHz have been published by Lossy et al [25].

The pioneering studies for undoped AlGa_N/Ga_N heterostructures were initiated by Cornell University. The highest output power of 11.2 W/mm at 10 GHz was reported for AlGa_N/Ga_N HEMT grown on SiC substrate after proper surface passivation.

Later on, MBE growth of AlGa_N/Ga_N HEMT on Si substrates with an L_g of 0.5 μm yielded maximum transconductance of 160 mS/mm and current density of 600 mA/mm where f_T and f_{max} were 17 GHz and 40 GHz, respectively [26]. High-performance AlGa_N/Ga_N HEMT devices reported with a power density of 1 W/mm for 150x1 μm gate at 4 GHz where 28 GHz and 50 GHz, respectively [27]. The higher output power of 6.6 W/mm at 2 GHz has been reported [28].

Recent progress for GaN-based HEMT devices has been summarized in Table 2.1. below. As shown in Table 2.1. decreasing the L_g down to sub-100 nm regime with a novel production technology allows improving the frequency performances.

Table 2.1 Recent Progress for GaN-based HEMT Devices

L_g (nm)	I_{DSS} (A/mm)	f_T (GHz)	f_{max} (GHz)	f (GHz)	P_{out} (W/mm)	Substrate	Ref.
20	>4	342	518			SiC	[29]
20		454	444			SiC	[30]
30	1.57	245	13			SiC	[31]
30	1.80	300	33			SiC	[32]
30	1.50	370	30			SiC	[33]
30	1.90	400	33			SiC	[34]
50	2.10	221	290			SiC	[35]
60	2.10	210	55			SiC	[36]
60	1.65	183	191	38	2.70	SiC	[37]
70	1.65	162	176			SiC	[38]
75	1.05	152	149	40	2.00	Si	[39]
75	0.80	170	210			SiC	[40]
80	1.10	114	230	40	1.25	SiC	[41]
80		176	70			Si	[42]

2.3 Semiconductor-Metal Contacts

Production of electronic devices requires putting two or more dissimilar materials (semiconductors, metals, insulators) together. The interface between these materials becomes very important because it affects the electrical properties (transport) of the devices.

In general, contacts in metal-semiconductors could be divided into two types which are Schottky contacts and Ohmic contacts. Metal-semiconductor contacts are characterized by the energy difference between the conduction band edge of the semiconductor and the metal Fermi Level (E_F) which is called ‘Barrier Height’. The design of Schottky or Ohmic contact is quite different. For Schottky contacts, Barrier Height should be high enough to have proper current rectification. On the other hand, in ohmic contacts, the Barrier Height should be as low as possible to have a low resistance connection between semiconductors and metals.

A typical energy band diagram is seen in Figure 2.7 for metal and n-type semiconductors which are isolated and electrically neutral. The work function of semiconductor (ϕ_s) is less than that of the metal work function (ϕ_m), where χ is the electron affinity, E_{fm} is Fermi levels for metal and semiconductor, respectively.

This is the most common case while forming semiconductor-metal contacts. E_c is the conduction band edge, E_v is the valance band edge and E_{fs} and E_{fm} are Fermi levels for metal and semiconductor, respectively. This is the most common case while forming semiconductor-metal contacts.

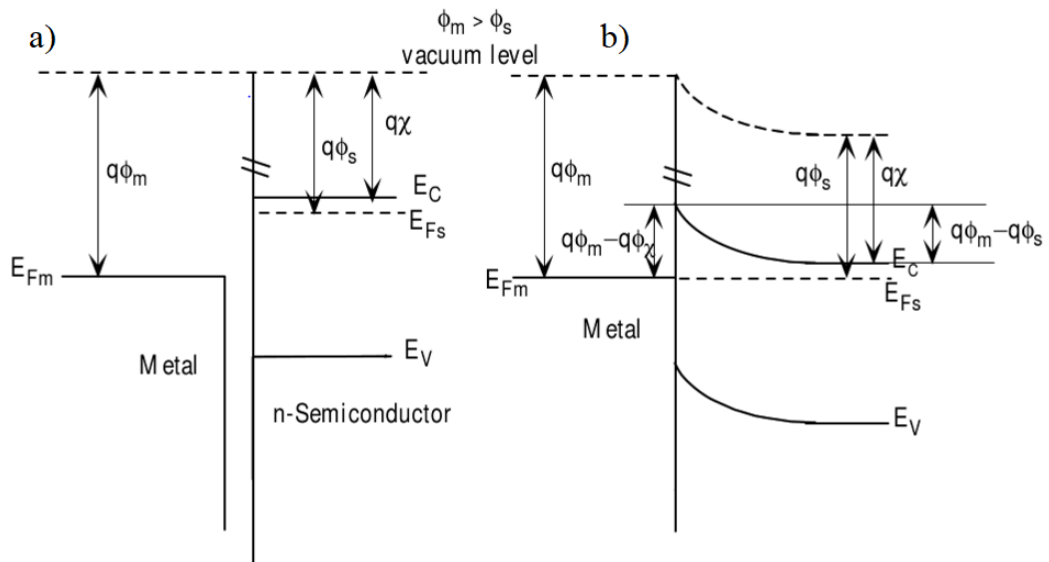


Figure 2.7. Metal and n-type Semiconductor a) before and b) after contact where ϕ_m is greater than that of ϕ_s [69]

The Fermi levels must be equal at thermal equilibrium and the vacuum level should be continuous. These two requirements determine the energy band diagram for the ideal metal-semiconductor contact. For this case, the Schottky Barrier Height (ϕ_b) is given by;

$$\phi_b = q\phi_m - q\chi \quad (\text{Eq.2.7})$$

In this case, the electron starts to move metal until the Fermi Levels are equal. The amount of the band bending is called ‘Built-in Potential’ (V_{bi}) which is a barrier for electrons in the conduction band of semiconductor which is trying to flow into metal.

There are several ways for charge carriers transported through a semiconductor-metal junction is [45];

- i) **Thermionic Emission (TE):** Carriers transport to metal by passing over V_{bi}
- ii) **Thermionic Field Emission (TFE):** Tunneling of hot charge carriers through the top of Schottky Barrier Height (ϕ_b)
- iii) **Field Emission (FE):** Carrier tunneling through the whole Schottky Barrier Height (ϕ_b), which is preferred for Ohmic Contacts

The band alignment for p-type semiconductor and metal is shown in Figure 2.8. The barrier height is $E_g + q(\chi - \phi_m)$ for holes traveling from metal to semiconductor and $q(\phi_s - \phi_m)$ for holes traveling from semiconductor to metal.

As a result, metal with a higher work function is desired to form ohmic contact to the p-type semiconductor whereas metal with lower work function is a good choice to form ohmic contact to the n-type semiconductor.

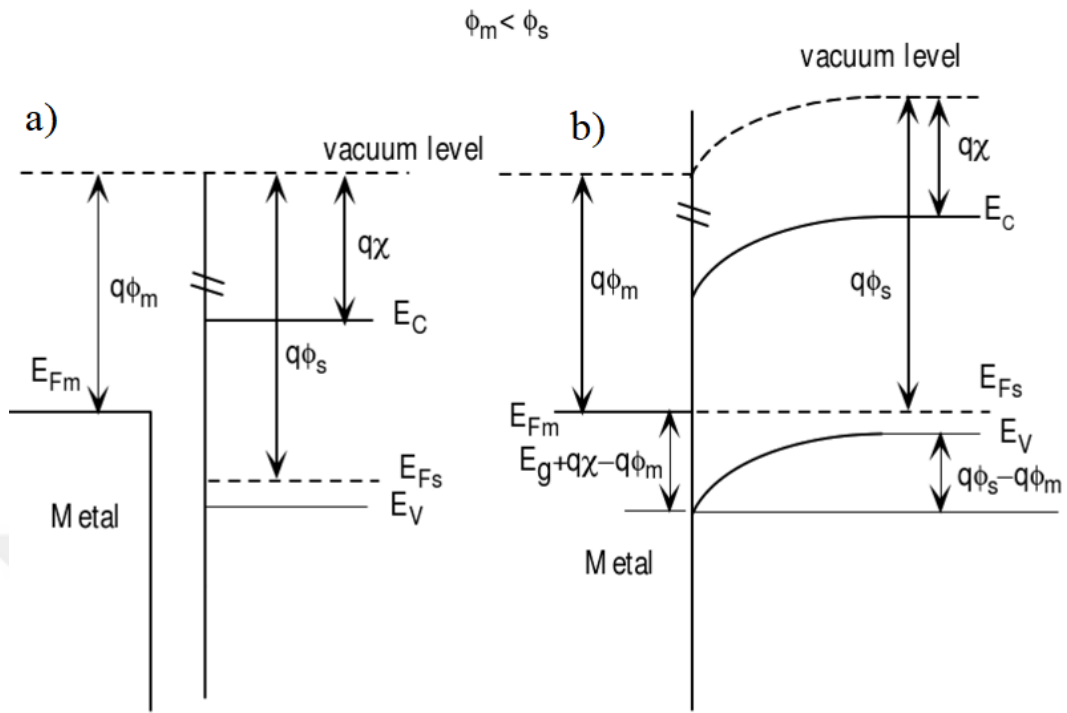


Figure 2.8. Metal and p-type Semiconductor a) before and b) after contact where ϕ_s is greater than that of ϕ_m [69]

2.3.1 Ohmic Contact to GaN

An ohmic contact is a junction between semiconductor and metal that allows charge the carrier to flow on both sides without distortion of the signal. Ohmic contacts obey Ohm's Law;

$$V = IxR \tag{Eq.2.8}$$

which is a linear relationship between current and voltage.

Ohmic contacts are very important parts of the solid-state device since it directly affects the power consumption and internal heating of the device which are key factors when considering device performance. An ideal ohmic contact could be capable of delivering current flow with a negligible drop of voltage across contacts. The current-voltage graph of the contact should be linear and symmetric. Contact

resistance is strongly depending on processing parameters used during microfabrication. As a result, it is very crucial to develop ohmic contacts with low contact resistance before the realization of any device [46,47].

The realization of ohmic contacts requires a thin, highly doped region at the metal-semiconductor junction. To make ohmic contact to GaN material is to use metals with appropriate work functions. High-temperature annealing in nitrogen ambient serves a thin highly doped region as desired for tunnel contact.

The realization of ohmic contacts requires a thin, highly doped layer at the interface. To make ohmic contact to GaN material is to use metals with appropriate work functions. High-temperature annealing in nitrogen ambient serves a thin highly doped region as desired for tunnel contact.

In recent years, much research has been conducted to get low resistance ohmic contacts to AlGaN/GaN heterostructures by universities and companies. The formation of low resistance ohmic contact to GaN is challenging due to the wide bandgap of GaN-based materials. Al [48,49], Ti [50] and Ti/Al [48] metal stacks have been widely used to have lower contact resistance.

A new metallization scheme was introduced by Fan et al. [51] where they used Ti/Al/Ni/Au in which new metals (Ni and Au) were added on the top of Ti/Al layers. This configuration of metals had a specific contact resistivity of $\rho_c \sim 8.9 \times 10^{-8} \Omega \cdot \text{cm}^2$ at the optimal annealing condition. After this report, a standard Ti/Al/X/Au ohmic contact metallization scheme where X is Pt [52], X is Ni [53], X is Mo [54] and some other variants are used for GaN-based heterostructures.

Individual metal has its specific role in metal a stack which are described as follows [50,54];

Ti: Serve as an adhesion layer and reacts with nitrogen in GaN/AlGaN layers and forming TiN which has a lower work function and causes to decrease SBH and help to make proper contact formation. It also generates N-

vacancies within GaN/AlGaN which cause to material highly n-doped and increase tunneling probability of electrons through a thin potential barrier

Al: Reacts with Ti to form Al_3Ti layer that prevents Ti from oxidation. It also reacts with epilayer and forms AlN, resulting in N-vacancies which improves contact resistance.

Pt, Ni or Mo: used as a barrier metal for inter-mixing of Al and Au which forms high resistive Al_2Au phase known as ‘purple plague’. These metal layers play an important role in forming both lower ohmic contact resistance and surface morphology.

Au: To prevent oxidation of Ti and Al during high-temperature annealing and improve contact resistivity

Apart from a metal work function, there are different carrier transport mechanism at the junction of metal-semiconductor materials that depends on the semiconductor doping level as seen in Figure 2.9 below.

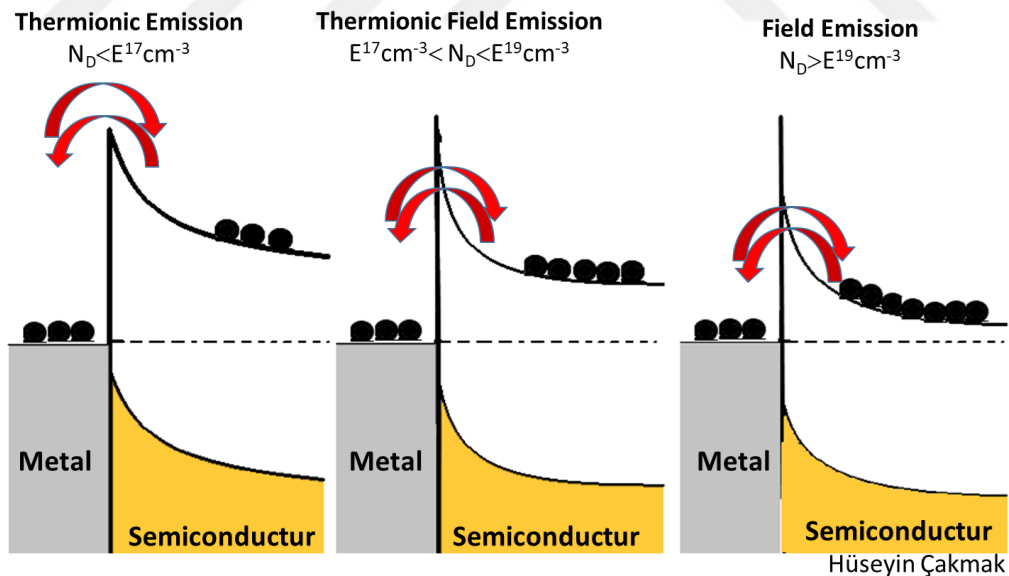


Figure 2.9. Carrier transport mechanisms for lightly, moderate, and highly doped semiconductor/metal interface

In general, the **Thermionic Emission (TE)** is the dominant mechanism for the electrons when the doping level, N_D , of the semiconductor is lower than $1 \times 10^{17} \text{cm}^{-3}$ and ρ_c expressed as follows [44];

$$\rho_c = \frac{k}{qA^{**T}} e^{\frac{q\phi_B}{kT}} \quad (\text{Eq.2.9})$$

where A^{**} is Richardson constant, q is the elementary charge and k is Boltzman Constant

In this case, ρ_c is not dependent on the N_D . W , which is defined as the space charge region is thick enough and electrons should gain enough thermal energy to pass over the Schottky Barrier Height, ϕ_B .

Thermionic Field Emission (TFE) mechanism is dominant when the range of doping in $1 \times 10^{17} \text{cm}^{-3} < N_D < 1 \times 10^{19} \text{cm}^{-3}$. The space charge region W gets sufficiently narrow and permits to tunneling of thermally excited electrons. In this case, ρ_c can be described as follows where E_{00} is the characteristic energy;

$$\rho_c \sim e^{\frac{\phi_B}{E_{00} \coth(\frac{E_{00}}{kT})}} \quad (\text{Eq.2.10})$$

$$\text{where } E_{00} = \frac{qh}{4\pi} \sqrt{\frac{N_D}{\epsilon\epsilon_0 m^*}} \quad (\text{Eq.2.11})$$

Field Emission (FE) is dominant when the semiconductor doping exceeds $N_D > 1 \times 10^{19} \text{cm}^{-3}$. In the Field Emission case, the space charge region W gets very thin and permits the tunneling of the electron through the junction. The contact resistance, ρ_c , could be described as follows;

$$\rho_c \sim e^{\frac{\phi_B}{\sqrt{N_D}}} \quad (\text{Eq.2.12})$$

In the case of Field Emission (FE), Eq. 2.12 clearly shows that the specific contact resistance strongly depends on both ϕ_B and N_D .

Metals with a lower SBH (ϕ_B) are crucial for obtaining low specific contact resistance.

Figure 2.10 shows the SBH of the various metals for both p-type and n-type GaN. Experimental results showed that Ti and Al metals are the best choices when considering ohmic contact to n-type GaN where SBH in the range of 0.4–0.5 eV.

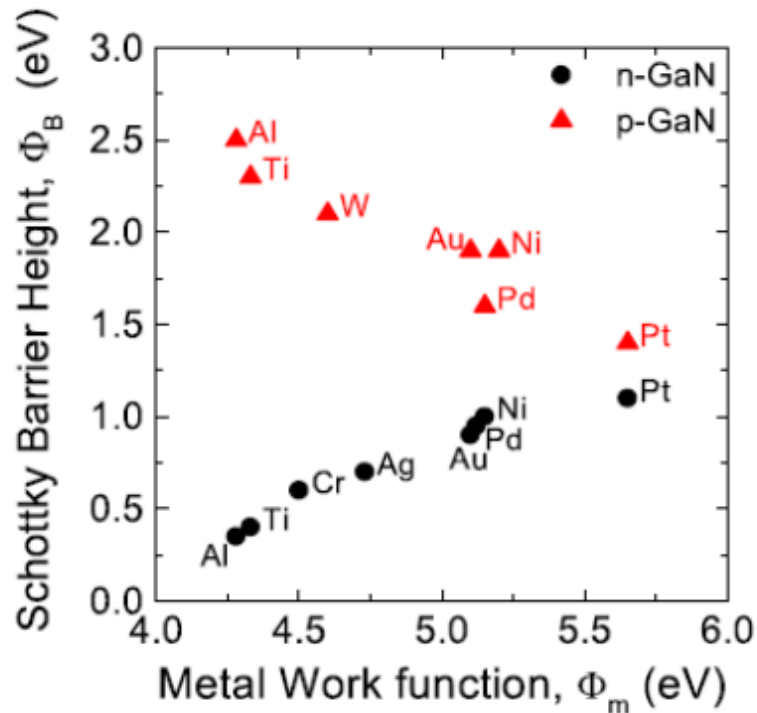


Figure 2.10. Literature survey of Schottky Barrier Height for different metals as a function of Metal Work Functions [44]

Several alternatives (Ta, W, Cr, Pt, ZrB₂, V, etc.) with different combinations and layer thicknesses have been used to form ohmic contacts to n-type GaN where specific contact resistances are in the range of $10^{-2} - 10^{-7} \Omega \cdot \text{cm}^2$. Specific contact resistance depends on various parameters like metal thickness and work function, the doping level of the semiconductor, and annealing conditions as seen in Figure 2.11 [44].

Annealing of metal stacks is an important step for making ohmic contacts. Annealing temperatures have to be tuned to create reliable ohmic contact with a smooth surface. Metal surface roughness is critical for the next coming lithography steps. Ti and Al

can react with GaN and form TiN or thin AlN resulted in lowering barrier height or making direct contact with 2DEG by the generation of N-vacancies under the ohmic contact. These N-vacancies have been introduced that occur electron tunneling through a heavily bent conduction band. However, Ti and Al are sensitive to oxygen which increases their resistivities during high-temperature annealing. Thus, most of the cases adapt cap metals above the Al to suppress oxidation of the under metals, such as molybdenum (Mo) or nickel (Ni) [62,63,64]. These metals also play a role as barrier metals that make gold (Au) cannot diffuse downward when high-temperature annealing is performed.

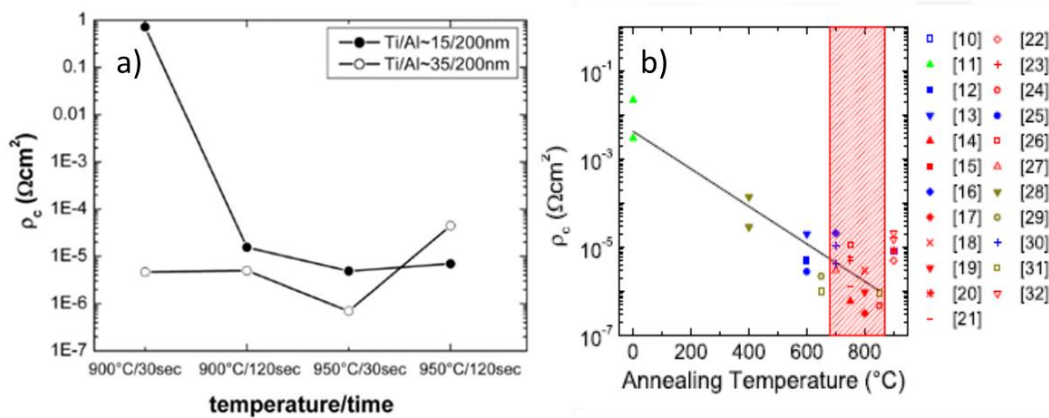


Figure 2.11. Changing of contact resistivity with annealing condition a) [65] b) where individual studies were listed by G. Greco in his paper [44]

Ti/Al/x/Au multilayer, where x could be Pd, Pt, and Mo metals, are widely used and characterized at elevated temperatures in order to have alloyed ohmic contacts to n-GaN and AlGaIn/GaN HEMT structures. The function of the Au metal is to prevent the underlying metal stack from oxidations during high-temperature annealing. Barrier metals (Pd, Pt, and Mo) are used to prevent the mixing of Ti, Al with Au metal and improve the reliability of the ohmic contacts. Decreasing ρ_c with increasing temperatures explained by the thermionic field emission mechanism [66].

2.3.2 Schottky Contacts to GaN

Schottky contacts do not allow any current through them unless a critical voltage is applied. A large amount of current passes through the Schottky contact when critical voltage is applied which is called the forward bias region. When voltage is applied in the opposite direction and no current flows through the device, it is called the reverse bias region. However, if the applied voltage is increased beyond some value, the breakdown occurs, and generally, contact is destroyed by a huge amount of current flow through the contacts.

Schottky contacts are one of the important blocks for HEMT devices. The key parameter of the junction is the Schottky Barrier Height (SBH) (Φ_B) which controls both electron transport across the interface and width of the depletion region in the semiconductors.

When considering the SBH of metal contacts to GaN, it is obvious that barrier height strongly depends on metal work function. However, many researchers have found that Φ_B weakly depends on metal work function [55,56].

Schottky Barrier Heights (SBH) of Pt, Ni, Pd, Au and Ti are 1.04 eV [56], 0.99 eV [57], 0.94 eV [56], 0.94 eV [56], and 0.58 eV [58], respectively, on n-type GaN. Their work functions are 4.3 eV for Ti, 5.1 eV for Au and Pd, 5.15 eV for Ni, and 5.65 eV for Pt. The difference in SBH is smaller than the difference in their work function which implies that the metal work function is not the only factor that determines SBH of metals to n-type GaN. The same situation is also valid for metal p-type GaN.

The suitable gate contacts for microwave devices are Schottky contacts due to their switching speeds between forward and reverse current which is on the order of picoseconds.

Schottky gates designed for microwave applications should have the following features [14];

- Low gate and drain leakage currents

- Low gate resistance
- High breakdown voltages
- Good thermal stability
- Good adhesion

In order to have high breakdown voltage, low drain leakage currents, and low gate leakage currents Schottky Barrier Height (SBH) between the gate metal and AlGaN barrier layer should be as high as possible. The work function of the metal which is used as a gate metal has a stronger influence on the Schottky Barrier Height (SBH). Schottky Barrier Height (SBH) also depends on both defect density of the films used, local stoichiometry variation, process details and etc.

Ni and Ir are known to have the best adhesion to AlGaN and GaN epilayers which is important to avoid any metal peel off during device microfabrication. Good thermal stability is another important parameter for metals that are used for gate metal. Channel temperatures of GaN-based HEMT could reach up to 400 °C, depending on the substrate used, bias condition, and power dissipation [59,60,61]. The resistance of the Schottky gates should be since it determines not only the input impedance but also influence f_{max} , maximum available gain (MAG), and noise figure of the devices. The gate resistance decreased by using a T-shaped gate (mushroom gate) geometry.

2.4 References

- [1] S. Taking, “AlN/GaN MOS-HEMTs Technology”, PhD Thesis, University of Glasgow, 2012
- [2] P. Javorka, “Fabrication and Characterization of AlGaIn/GaN High Electron Mobility Transistor”, PhD Thesis, RWTH Aachen University, 2004
- [3] X. Liu et al., "GaN Schottky Barrier Diodes on Free-Standing GaN Wafer," *ECS Journal of Solid State Science and Technology*, vol. 6, no. 10, pp. N216-N220, 2017.
- [4] J. W. Pomeroy, M. Bernardoni, D. C. Dumka, D. M. Fanning, and M. Kuball, "Low thermal resistance GaN-on-diamond transistors characterized by three-dimensional Raman thermography mapping," *Applied Physics Letters*, vol. 104, no. 8, 2014.
- [5] H. Sun *et al.*, "Temperature-Dependent Thermal Resistance of GaN-on-Diamond HEMT Wafers," *IEEE Electron Device Letters*, vol. 37, no. 5, pp. 621-624, 2016.
- [6] H. P. Maruska and J. J. Tietjen, “The preparation and properties of vapor-deposited single-crystalline GaN,” *Appl. Phys. Lett.*, vol. 15, pp. 327–329, Nov. 1969.
- [7] W. Zhang and B. K. Meyer, “Growth of GaN quasi-substrates by hydride vapor phase epitaxy,” *Phys. Stat. Sol. (c)*, vol. 0, no. 6, pp. 1571–1582, 2003.
- [8] H. M. Manasevit, F. M. Erdman, and W. I. Simpson, *J. Electrochem. Soc.*, vol. 118, p. 1864, 1971.
- [9] F. Ren and J. C. Zolper, *Wide energy bandgap electronic devices*. New Jersey: World Scientific, 2003, ISBN 981-238-246-1.
- [10] S. Keller, B. P. Keller, Y. F. Wu, B. Heying, D. Kapolnek, J. S. Speck, U. K. Mishra, and S. P. Den-Baars, “Influence of sapphire nitridation on properties of gallium nitride grown by metalorganic chemical vapor deposition,” *Appl. Phys. Lett.*, vol. 68, no. 11, pp. 1525–1527, Mar. 1996.
- [11] R. J. Molnar, W. Götz, L. T. Romano, and N. M. Johnson, “Growth of gallium nitride by hydride vapor-phase epitaxy,” *J. Cryst. Growth*, vol. 178, pp. 147–156, 1997.
- [12] S. M. Sze, “*Semiconductor Devices – Physics and Technology*”, New Jersey 1985
- [13] J. Michael Golio, Eric N. Arnold, and William B. Beckwith, *Microwave MESFETs and HEMTs*, Artech House London (1991)
- [14] M. C. J. C. M. Krämer, ‘Gallium Nitride-based Microwave High-Power Heterostructure Field-Effect Transistors’ PhD Thesis, Technische Universiteit Eindhoven, October 2006

- [15] A. Khan, M. J. N. Kuzina, D. T. Olson, W. J. Schaff, J. W. Burm, and M. S. Shur, Microwave performance of a 0.25 μ m gate AlGaIn/GaN heterostructure field effect transistor, *Appl. Phys. Lett.* 65, 1121-2 (1994)
- [16] Ö. Aktas, W. Kim, Z. Fan, S. N. Mohammad, A. Botchkarev, A. Salvador et al, High transconductance-normally-off GaN MOD-FETs., *Electron. Dev. Lett.* 31, 16, 1389-90 (1995)
- [17] F. Y. Wu, P. B. Keller, D. Kapolnek, P. S. Denbaars, and U. K. Mishra, Measured microwave power performance of AlGaIn/GaN MODFET., *IEEE Electron. Dev. Lett.* 17, 455-7 (1995)
- [18] F. Y. Wu, P. B. Keller, P. Parikh, D. Kapolnek, S. P. Denbaars and U. K. Mishra, Bias dependent microwave performance of AlGaIn/GaN MODFET's up to 100V, *IEEE Electron Dev. Lett.* 18, 290-2 (1997)
- [19] U. K. Mishra, F. Y. Wu, P. B. Keller, S. Keller and P. S. Denbaars, GaN microwave electronics 1997 Topical Symp. on Millimeter Waves, Kanagawa, Japan (1997)
- [20] M. Micovic, N. X. Nguyen, P. Janke, W. S. Wong, P. Hashimoto, L. M. McCray and C. Nguyen, GaN/AlGaIn high electron mobility transistors with fT of 110GHz 36, 4 (2000)
- [21] V. Kumar, W. Lu, F. A. Khan, R. Schwindt, A. Kuliev, G. Simin, J. Yang, M. Asif Khan and I. Adesida, High performance 0.25 μ m gate-length AlGaIn/GaN HEMTs on sapphire with transconductance of over 400 mS/mm, *Electron. Lett.* 38, 5 (2002)
- [22] T. S. Sheppard, K. Doverspike, L. W. Pribble, T. S. Allen, W. J. Palmour, T. I. Kehias, et al, High power microwave GaN/AlGaIn HEMTs on semi-insulating silicon carbide substrates, *IEEE Electron Dev. Lett.* 20, 4, 161 (1999)
- [23] G. J. Sullivan, M. Y. Chen, J. A. Yang, Q. Chen, R. L. Pierson, et al, High-power 10-GHz operation of AlGaIn HFETs on insulating SiC., *IEEE Electron Dev. Lett.* 19, 198-9 (1998)
- [24] L. Wu, J. Yang, M. A. Khan, and I. Adesida, AlGaIn/GaN HEMTs on SiC with over 100GHz fT and Low Microwave Noise, *IEEE Trans. Elect. Dev.* 48, 3 (2001)
- [25] R. Lossy, P. Heymann, J. Würfl, N. Chaturvedi, S. Müller, and K. Köhler, Power RF-Operation of AlGaIn/GaN HEMTs Grown on Insulating Silicon Carbide Substrates
- [26] Y. Cordier, F. Semond, J. Massies, B. Dessertene, S. Cassette, M. Surrugue, D. Adam and S. L. Delage, AlGaIn/GaN HEMTs on resistive Si(111) substrate grown by gas-source MBE, *Electron. Lett.* 38, 2 (2002)
- [27] V. Hoël, N. Vellas, C. Gaquière, J. C. De Jaeger, Y. Cordier, F. Semond, F. Natali and J. Massies, High-power AlGaIn/GaN HEMTs on resistive silicon substrate., *Electron. Lett.* 38, 14 (2002)

- [28] R. Behtash, H. Tobler, M. Neuburger, A. Schurr, H. Leier, F. Semond, F. Natali, and Massies, AlGaIn/GaN HEMTs on Si(111) with 6.6W/mm output power density, *Electron. Lett.* 39, 7 (2003)
- [29] K. Shinohara, D. Regan, A. Corrion, D. Brown, Y. Tang, J. Wong, G. Candia, A. Schmitz, H. Fung, S. Kim, et al., “Self-aligned-gate gan-hemts with heavily-doped n+-gan ohmic contacts to 2deg,” in *Electron Devices Meeting (IEDM), 2012 IEEE International*, pp. 27–2, IEEE, 2012.
- [30] Y. Tang, K. Shinohara, D. Regan, A. Corrion, D. Brown, J. Wong, A. Schmitz, H. Fung, S. Kim, and M. Micovic, “Ultrahigh-speed gan high-electron-mobility transistors with f_{max} of 454/444 ghz,” *IEEE Electron Device Letters*, vol. 36, no. 6, pp. 549–551, 2015.
- [31] D. S. Lee, J. W. Chung, H. Wang, X. Gao, S. Guo, P. Fay, and T. Palacios, “245-ghz inaln/gan hemts with oxygen plasma treatment,” *IEEE Electron Device Letters*, vol. 32, no. 6, pp. 755–757, 2011.
- [32] D. S. Lee, X. Gao, S. Guo, D. Kopp, P. Fay, and T. Palacios, “300-ghz inaln/gan hemts with ingan back barrier,” *IEEE Electron Device Letters*, vol. 32, no. 11, pp. 1525–1527, 2011.
- [33] Y. Yue, Z. Hu, J. Guo, B. Sensale-Rodriguez, G. Li, R. Wang, F. Faria, T. Fang, B. Song, X. Gao, et al., “Inaln/aln/gan hemts with regrown ohmic contacts and f_{T} of 370 ghz,” *IEEE Electron Device Letters*, vol. 33, no. 7, pp. 988–990, 2012.
- [34] Y. Yue, Z. Hu, J. Guo, B. Sensale-Rodriguez, G. Li, R. Wang, F. Faria, B. Song, X. Gao, S. Guo, et al., “Ultrascaled inaln/gan high electron mobility transistors with cutoff frequency of 400 ghz,” *Japanese Journal of Applied Physics*, vol. 52, no. 8S, p. 08JN14, 2013.
- [35] P. Murugapandiyan, S. Ravimaran, and J. William, “Static and dynamic characteristics of lg 50nm inaln/aln/gan hemt with algan back-barrier for high power millimeter wave applications,” *Journal of Science: Advanced Materials and Devices*, 2017.
- [36] Y.-K. Lin, S. Noda, C.-C. Huang, H.-C. Lo, C.-H. Wu, Q. H. Luc, P.-C. Chang, H.-T. Hsu, S. Samukawa, and E. Y. Chang, “High-performance gan moshemts fabricated with al₂o₃ dielectric and nbe gate recess technology for high frequency power applications,” *IEEE Electron Device Letters*, vol. 38, no. 6, pp. 771–774, 2017.
- [37] H. Tingting, D. Shaobo, L. Yuanjie, G. Guodong, S. Xubo, W. Yuangang, X. Peng, and F. Zhihong, “70-nm-gated inaln/gan hemts grown on sic substrate with $f_{max} > 160$ ghz project supported by the national natural science foundation of china (no. 61306113).,” *Journal of Semiconductors*, vol. 37, no. 2, p. 024007, 2016.
- [38] D. Geum, S. Shin, M. Kim, and J. Jang, “75 nm t-shaped gate for in_{0.17}al_{0.83}n/gan hemts with minimal short-channel effect,” *Electronics Letters*, vol. 49,

- no. 24, pp. 1536–1537, 2013. [60] B. P. Downey, D. J. Meyer, D. S. Katzer, J. A. Roussos, M. Pan, and X. Gao, “Six /in aln/aln/gan mis-hemts with 10.8 thzv johnson_gure of merit,” *IEEE Electron Device Letters*, vol. 35, no. 5, pp. 527–529, 2014.
- [39] W. Jatal, U. Baumann, K. Tonisch, F. Schwierz, and J. Pezoldt, “High-frequency performance of gan high-electron mobility transistors on 3c-sic/si substrates with au-free ohmic contacts,” *IEEE Electron Device Letters*, vol. 36, no. 2, pp. 123–125, 2015.
- [40] H. Zhou, X. Lou, K. Sutherlin, J. Summers, S. B. Kim, K. D. Chabak, R. G. Gordon, and D. Y. Peide, “Dc and rf performance of algan/gan/sic moshemts with deep sub-micron t-gates and atomic layer epitaxy mgcao as gate dielectric,” *IEEE Electron Device Letters*, vol. 38, no. 10, pp. 1409–1412, 2017.
- [41] W. Jatal, U. Baumann, K. Tonisch, F. Schwierz, and J. Pezoldt, “High-frequency performance of gan high-electron mobility transistors on 3c-sic/si substrates with au-free ohmic contacts,” *IEEE Electron Device Letters*, vol. 36, no. 2, pp. 123–125, 2015.
- [42] X. Liu et al., “GaN Schottky Barrier Diodes on Free-Standing GaN Wafer,” *ECS Journal of Solid State Science and Technology*, vol. 6, no. 10, pp. N216-N220, 2017.
- [43] A. Piotrowska, A. Guivarc'h, and G. Pelous, “Ohmic contacts to III-V compound semiconductors: A review of fabrication techniques,” *Solid-State Electronics*, vol. 26, no. 3, pp. 179–197, 1983.
- [44] G. Greco, “Ohmic Contacts to Gallium Nitride Materials,” *Applied Surface Science*, Volume 383, 15 October 2016, Pages 324-345.
- [45] A. Piotrowska, A. Guivarc'h, and G. Pelous, “Ohmic contacts to III-V compound semiconductors: A review of fabrication techniques,” *Solid-State Electronics*, vol. 26, no. 3, pp. 179–197, 1983.
- [46] Zangwill, A. (1988). *Physics at Surfaces*, Cambridge University Press.
- [47] Zeghbroeck, B. V. (2004). *Principles of semiconductor devices*, Colorado State University.
- [48] B. P. Luther, S. E. Mohny, T. N. Jackson, M. Asif Khan, Q. Chen, and J. W. Yang, “Investigation of the mechanism for Ohmic contact formation in Al and Ti/Al contacts to n-type GaN,” *Applied Physics Letters*, vol. 70, no. 1, pp. 57–59, Jan. 1997.
- [49] L. L. Smith, R. F. Davis, M. J. Kim, R. W. Carpenter, and Y. Huang, “Microstructure, electrical properties, and thermal stability of Al Ohmic contacts to n-GaN,” *Journal of Materials Research*, vol. 11, no. 9, pp. 2257–2262, Sep. 1996.
- [50] B. Van Daele, G. Van Tendeloo, W. Ruythooren, J. Derluyn, M. R. Leys, and M. Germain, “The role of Al on Ohmic contact formation on n-type GaN and

- AlGaIn/GaN," *Applied Physics Letters*, vol. 87, no. 6, pp. 061 905 {061 905 {3, Aug. 2005.
- [51] Z. Fan, S. N. Mohammad, W. Kim, O. Aktas, A. E. Botchkarev, and H. Morkoc, "Very low resistance multilayer Ohmic contact to n-GaN," *Applied Physics Letters*, vol. 68, no. 12, pp. 1672 {1674, Mar. 1996.
- [52] S. Cai, R. Li, Y. Chen, L. Wong, W. Wu, S. Thomas, and K. Wang, "High performance AlGaIn/GaN HEMT with improved Ohmic contacts," *Electronics Letters*, vol. 34, no. 24, pp. 2354 {2356, Nov. 1998.
- [53] B. Jacobs, "Towards integrated AlGaIn/GaN based X-band high-power amplifiers." Ph. D. dissertation, Technische Universiteit Eindhoven, 2004.
- [54] F. M. Mohammed, L. Wang, D. Selvanathan, H. Hu, and I. Adesida, "Ohmic contact formation mechanism of Ta/Al/Mo/Au and Ti/Al/Mo/Au metallizations on AlGaIn/GaN HEMTs," *Journal of Vacuum Science & Technology B: Microelectronics and Nanometer Structures*, vol. 23, no. 6, pp. 2330 {2335, 2005
- [55] P. Hacke, T. Detchprohm, K. Hiramatsu, and N. Sawaki, "Schottky barrier on n-type GaN grown by hydride vapor phase epitaxy," *Appl. Phys. Lett.*, vol. 63, no. 19, pp. 2676–2678, Nov. 1993.
- [56] J. D. Guo, M. S. Feng, R. J. Guo, F. M. Pan, and C. Y. Chang, "Study of Schottky barriers on n-type GaN grown by low-pressure metalorganic chemical vapor deposition," *Appl. Phys. Lett.*, vol. 67, no. 18, pp. 2657–2659, Oct. 1995.
- [57] A. C. Schmitz, A. T. Ping, M. A. Khan, Q. Chen, J. W. Yang, and I. Adesida, "Schottky barrier properties of various metals on n-type GaN," *Semicond. Sci. Technol.*, vol. 11, no. 10, p. 1464, 1996. 85
- [58] S. C. Binari, H. B. Dietrich, G. Kelner, L. B. Rowland, K. Doverspike, and D. K. Gaskill, "Electrical characterisation of Ti Schottky barriers on n-type GaN," *Electron. Lett.*, vol. 30, no. 11, pp. 909–911, May 1994.
- [59] J. C. Freeman, Channel temperature model for microwave AlGaIn/GaN HEMTs on SiC and sapphire MMICs in high power, high efficiency SSPAs. NASA, Hanover, MD, 2004, TM-2004- 212900.
- [60] M. Kuball, J. M. Hayes, M. J. Uren, T. Martin, J. C. H. Birbeck, R. S. Balmer, and B. T. Hughes, "Measurement of temperature in active high-power AlGaIn/GaN HFETs using Raman spectroscopy," *IEEE Electron Device Letters*, vol. 23, no. 1, pp. 7–9, Jan. 2002.
- [61] J. Kuzmik, P. Javorika, A. Alam, M. Marso, M. Heuken, and P. Kordos, "Determination of channel temperature in AlGaIn/GaN HEMTs grown on sapphire and silicon substrates using DC characterization method," *IEEE Transactions on Electron Devices*, vol. 49, no. 8, pp. 1496–1498, Aug. 2002.

- [62] F. Calle *et al.*, *Journal of Materials Science: Materials in Electronics*, vol. 14, no. 5-7, pp. 271-277, May 2003.
- [63] L. Wang, *et al.*, *Journal of Applied Physics*, vol. 101, no. 1, Jan 2007.
- [64] W. Macherzyński *et al.*, *physica status solidi (a)*, vol. 213, no. 5, pp. 1145-1149, Feb 2016.
- [65] P. Javorka, ‘Fabrication and Characterization of AlGaIn/GaN HEMT’ PhD Thesis, RWTH Aachen University, 2004
- [66] S.Zhao, ‘Developing Ohmic Contacts to Gallium Nitride for High Temperature Application’, PhD Thesis, August 2016, Arizona State University
- [67] H.Çakmak ‘GROWTH AND CHARACTERIZATION OF INDIUM RICH INDIUM-GALLIUM-NITRIDE SOLAR CELL EPITAXIAL STRUCTURES BY METAL ORGANIC CHEMICAL VAPOR DEPOSITION’ M.Sc. Thesis, 2012, METU
- [68] H.Çakmak, ‘Indium rich InGaIn solar cells grown by MOCVD’ *J Mater Sci: Mater Electron* (2014) 25:3652–3658
- [69] V. Chakrapani, *Semiconductor Junctions, Solid-Solid Junctions* DOI: 10.1007/978-1-4419-6996-5_44

CHAPTER 3

COMPARISON OF ALLOYED AND NONALLOYED OHMIC CONTACTS IN ALGAN/GAN HEMTs

Entire microfabrication processes were performed in the Nanotechnology Research Center (NANOTAM) at Bilkent University. In this part, the process flow of GaN-based HEMTs is described along with some key factors which are detrimental to process steps.

In this work, epitaxial layers of HEMT structures were grown on both Al_2O_3 and SiC substrates by MOCVD. Figure 3.1. shows the HEMT stack layers grown on Al_2O_3 substrates and the corresponding 2DEG properties determined by Hall Effect measurements.

Cross-Section of HEMT Structures		2DEG Properties	
GaN Cap (~4 nm)		N_s (10^{13} cm^{-2})	1,25
$\text{Al}_{0.25}\text{GaN}$ Barrier (25nm)		μ ($\text{cm}^2/\text{V.s}$)	1748
AlN Spike Layer ~ 1nm		ρ ($\Omega.\text{cm}$)	283
Ud-GaN Buffer (~2 μm)			
Substrate (Al_2O_3 & SiC)			

Figure 3.1. Layer stacks of HEMT structure grown by MOCVD and corresponding 2DEG Properties

Electrical properties of the patterned ohmic contacts were determined using the linear transfer length method (TLM). Typical geometry of the metal contact pads and a sample resistance versus spacing curve are seen in Figure 3.2, below.

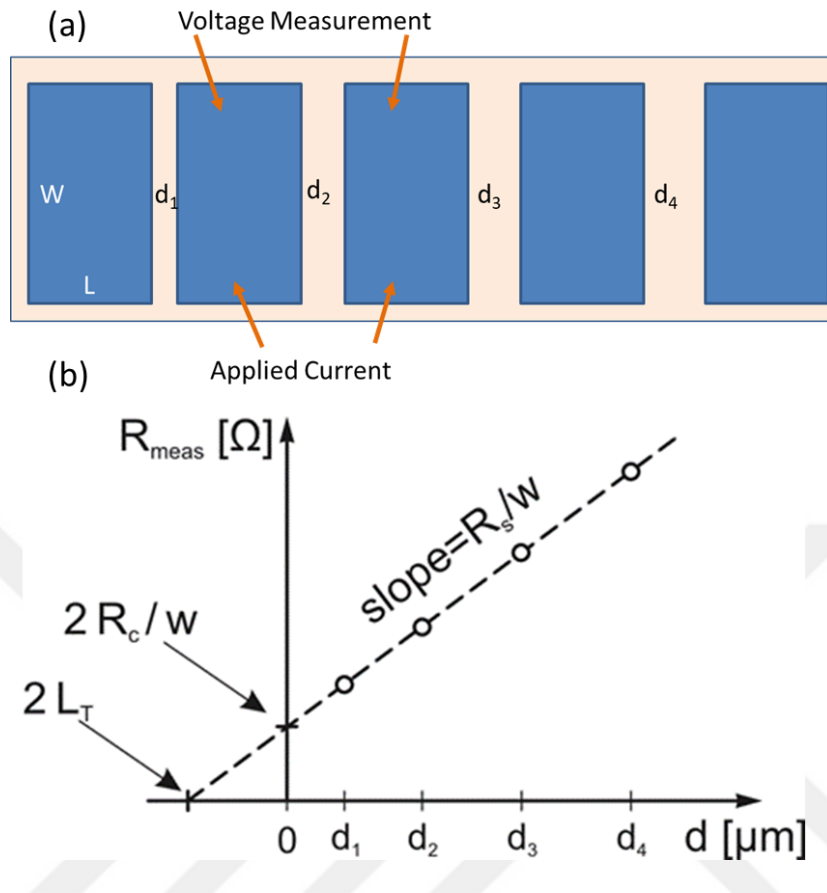


Figure 3.2. Schematic of patterned metal contacts with (a) TLM structure and measurement of (b) R-d curves with four-point probes [25]

The sample was etched down to the GaN buffer layer for device isolation. This is done for isolating conductive epilayers to restrict current flow in the region where TLM metal pads are produced. Predefined metal contact pads were deposited on the wafer in a way that increasing pad spacing. A constant current was passed between metal pads and voltage drop between these two pads was measured and used to obtain total resistance. Separate voltage sense and current source are essential in order to ignore the probe resistance which is important for measurement accuracy when the measured total resistance is relatively low. Then, the same measurements were performed for the successive metal pads. Measured total resistances are plotted on a linear graph as a function of pad spacing, d .

Measured total resistance is $R(d)$, between two successive metal contacts with spacing d , is given by;

$$R(d) = 2R_c + R_{\text{semi}} \quad (\text{Eq. 3.1})$$

Where R_c is the resistance between metal and semiconductor and R_{semi} is the resistance of semiconductor where;

$$R_{\text{semi}} = R_{\text{sh}} \times \frac{d}{W} \quad (\text{Eq.3.2})$$

R_{sh} is the sheet resistance of the semiconductor. Hence, we have;

$$R_{(d)} = 2R_c + R_{\text{sh}} \times \frac{d}{W} \quad (\text{Eq.3.3})$$

By plotting $R(d)$ versus d gives we have R_c and R_{sh} .

$$R_c = (\text{Intercept} \times W)/2 \quad (\text{Eq. 3.4})$$

$$R_{\text{sh}} = \text{slopex}W \quad (\text{Eq. 3.5})$$

Contact resistance depends on the size of the contact. Therefore, specific contact resistivity, ρ_c

$$\rho_c = R_{\text{sh}} \times L_T^2 \quad (\text{Eq. 3.6})$$

where L_T is the current transfer length.

The standard process flow sequence is depicted in Figure 3.3. Epi-wafer was diced into 15 mm x 15 mm pieces and followed by a standard ACE/ISO cleaning. Standart lithography processes were utilized to form TLM patterns with the dimensions of W/L: 200 μm / 100 μm and spacing were 2 μm , 3 μm , 4 μm , 5 μm , 7 μm , 10 μm , 14 μm , and 20 μm between pads. In order to make electrical isolation of the TLM pads Inductively Coupled Plasma – Reactive Ion Etching (ICP-RIE) processes were used to form mesa isolation by etching epitaxial layers down to GaN buffer layer.

In order to optimize the contact resistance, R_c , alloyed ohmic contacts different metal stacks, and Rapid Thermal Annealing (RTA) conditions and recessed non-alloyed

ohmic contacts were fabricated. In this study, AlGaN/HEMT on Al₂O₃ substrates were utilized for determining the quality of fabricated ohmic contacts.

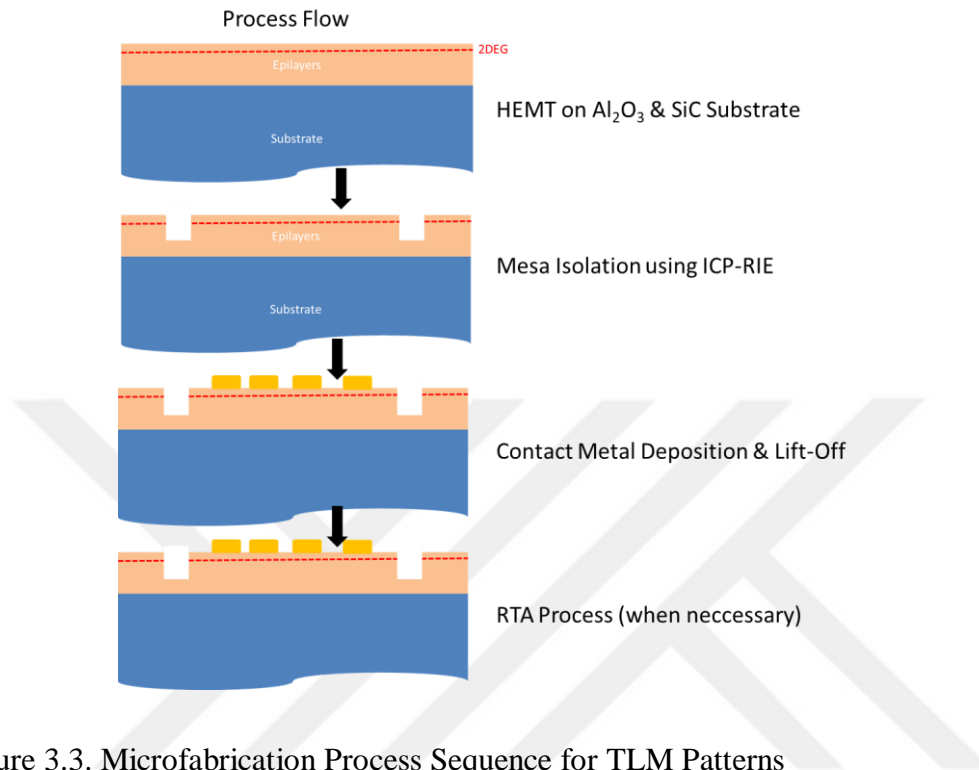


Figure 3.3. Microfabrication Process Sequence for TLM Patterns

3.1 Ohmic Contacts to AlGaN/GaN HEMTs

In alloyed ohmic contacts, a Rapid Thermal Annealing (RTA) process (above 800 °C) is necessary to obtain low contact resistances for Ti-based metal stacks. Thermal degradation of epitaxial layers could be happening at such high annealing temperatures. Deterioration of surface morphology of Ti-based metal schemes after high-temperature annealing decrease edge acuity that affect the accurate alignment of the gate electrodes.

In addition to morphological deterioration, epitaxial degradation could also happen due to the high-temperature annealing that closes to epitaxial growth temperatures. High-temperature processes that are used for microfabrication processes could potentially affect the quality of epitaxial layers which results in an increase of sheet

resistance, R_s . An increase in R_s pushes knee voltage (V_{knee}) to higher values, decreases I_{ds} , and hence kills device performance.

As seen in Figure 3.4., the presence of an unstable edge morphology due to high-temperature thermal annealing (which is above the Al melting point of 660 °C) ultimately affects the device parameters. Any decrease in RTA temperature results in an increase in ohmic contact resistance which kills device performance.

To alleviate this problem, one needs to develop a new way of making ohmic contacts without a need for the RTA process performed at elevated temperatures.

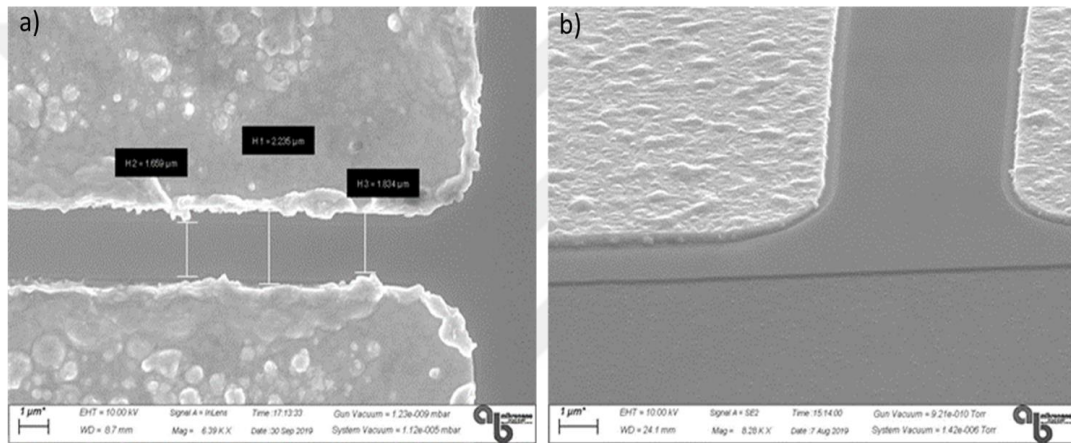


Figure 3.4. SEM images of a) deteriorated surface morphology of ohmic contacts due to high temperature annealing and b) acceptable ohmic contact morphology

3.1.1 Varying Al Thicknesses

An alloyed or planar ohmic contact is the simplest and standard method to fabricate ohmic contact to GaN HEMTs. A planar metal contact is formed by standard microfabrication processes (lithography and metalization) and followed by rapid thermal annealing (RTA) under a suitable condition. It is important to tune RTA conditions (temperature, time and etc.) in order to have well-defined edge profiles which are important for next coming lithography and other microfabrication steps.

In this study, we utilized different metals, metal stacks, and RTA temperatures in order to tune both contact resistance and metal edge profiles.

Ti, Al, Ni, and Au metal were deposited by the e-Beam Evaporation system. Contacts were then annealed at 825 °C for 30 sec in a nitrogen ambient. SEM inspection and TLM measurements were performed using four contact probe on 100 μm x 200 μm contact pads with the spacing of 2 μm, 3 μm, 4 μm, 5 μm, 7 μm, 10 μm, 14 μm, and 20 μm.

Table 3.1 shows the metal stacks deposited by e-Beam and corresponding contact properties including contact resistance and edge definitions. Ohmic contact resistances with varying Al thickness can be seen in Figure 3.5. Increasing Al thicknesses in metal stacks helped to improve contact resistance but surface morphology and edge acuity of the metal pads were worsened.

Table 3.1 Ohmic Metal Stacks with varying Al Thicknesses and Corresponding Contact Features

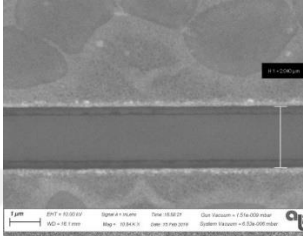
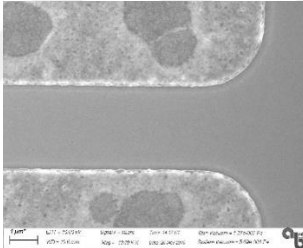
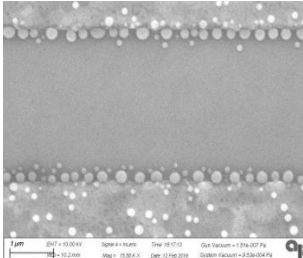
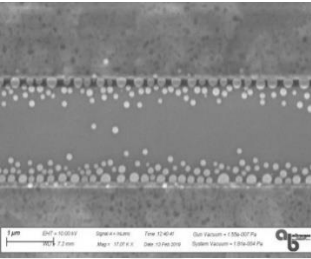
Metal Stacks (nm)	Sample Code	R_c (Ω .mm) R_s (Ω /sq)	Edge Definition (SEM Images)	Remarks
Ti-Al-Ni-Au 20-60-40-50	Al-60	R_c : 1.62 R_s : 440		Acceptable metal surface morphology, clean edge acuity but high contact resistance which is not acceptable
Ti-Al-Ni-Au 20-100-40-50	Al-100	R_c : 0.51 R_s : 371		Acceptable metal surface morphology, clean edge acuity and acceptable contact resistance
Ti-Al-Ni-Au 20-120-40-50	Al-120	R_c : 0.40 R_s : 346		Low contact resistance but not acceptable due to distorted line edges and surface morphology with increasing Al thickness.

Table 3.1 (continued)

Metal Stacks (nm)	Sample Code	R_c (Ω .mm) R_s (Ω /sq)	Edge Definition (SEM Images)	Remarks
Ti-Al- Ni-Au 20- 150 - 40-50	Al-150	R_c : 0.33 R_s : 448		Low contact resistance but not acceptable due to distorted line edges and surface morphology with increasing Al thickness.

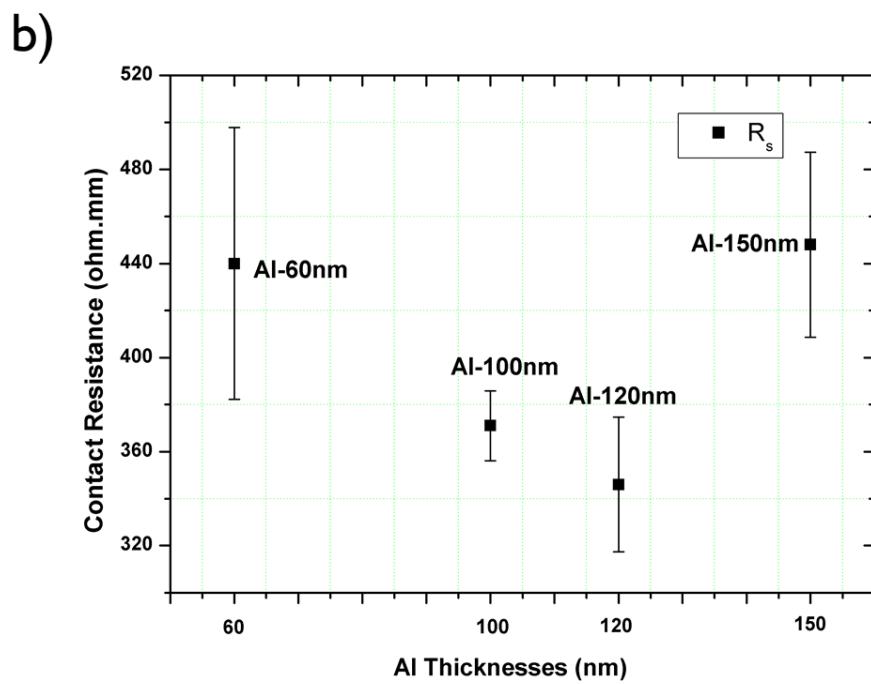
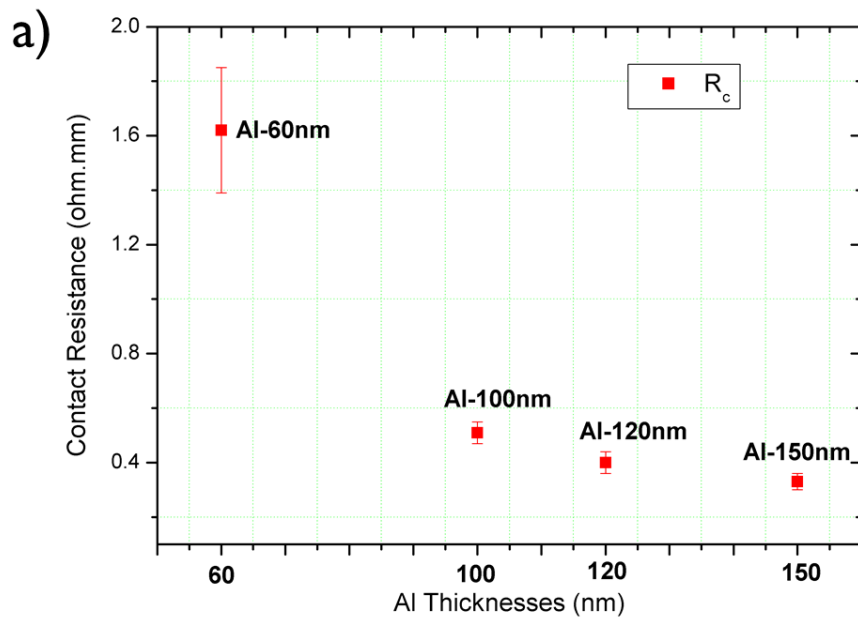


Figure 3.5. TLM Measurements of Ohmic Contacts with Different Al Thicknesses
 a) Contact resistance (R_c) and b) Sheet Resistivity (R_{sh})

Although it helps to improve contact resistances the use of thicker Al metal within metal stacks resulted in distorted metal edge lines and metal balls in the source and drain region due to the low melting of Al which is about 660°C. These problems make the gate lithography difficult to define a proper gate with clean source-drain openings. Al thickness was set to 100 nm in order to have better edge acuity and lower contact resistance which was 0.51 ohm. mm. Apart from the metal stack with 60 nm Al, we obtained almost similar R_c values ranging from 0.3 ohm. mm – 0.6 ohm. mm. It was seen that the ohmic contact morphology of the fabricated devices exhibited a remarkable difference. It is well known that Al metal within metal stacks diffuse in epilayers and forms AlN which results in N-vacancies in the epilayer hence heavily doped interface is formed. This heavily doped region improves tunneling current which is responsible for ohmic contact formation. Increasing Al thickness in our case helped us to improve contact resistance to some extent with reasonable surface morphology. Further increasing Al content in metal stacks resulted in distorted edge definition and metal bumps due to the low melting point of Al metal which is around 660 °C.

The Rapid Thermal Annealing (RTA) process was also optimized in order to improve contact resistivity with the metal stacks where Al thickness was kept at 100 nm. As seen in Figure 3.6., it was observed that contact resistance down to 0.45 ohm.mm with a reasonable surface morphology when increasing RTA temperature up to 850 °C/45 sec. Further increasing RTA temperature helped to improve contact resistance below 0.37 ohm.mm but the contact morphology started to deteriorate.

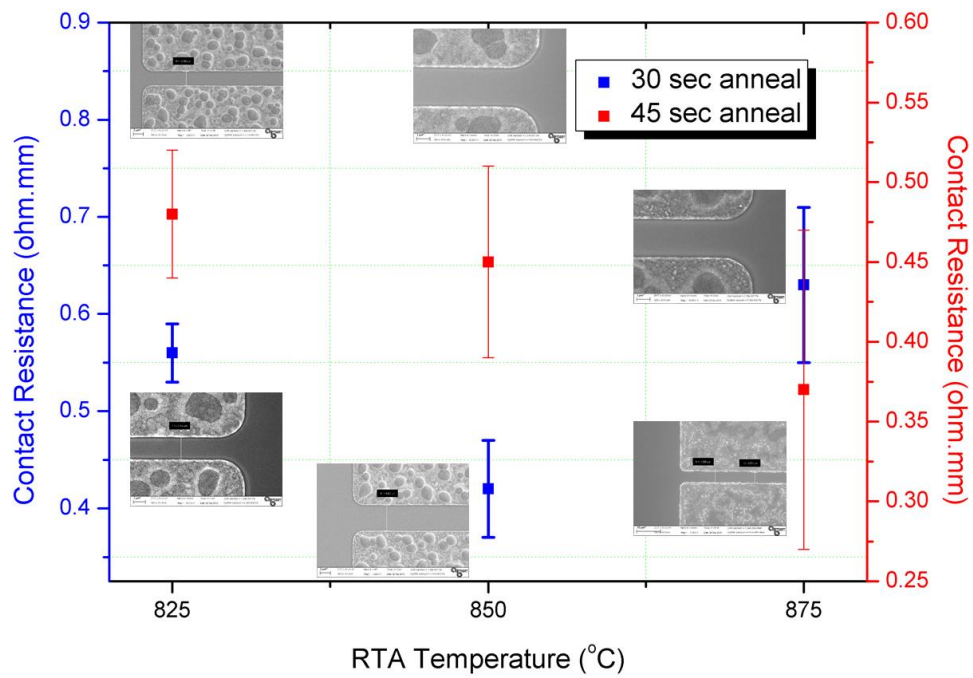


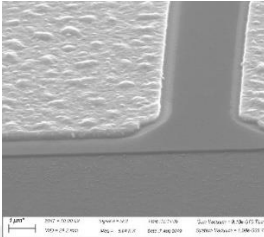
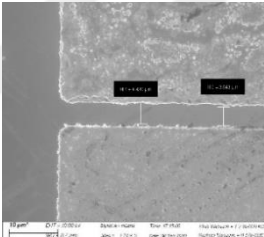
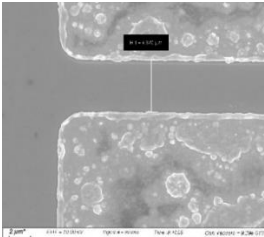
Figure 3.6. TLM Measurements of Ohmic Contacts with Different RTA Conditions

3.1.2 Alternative Barrier Metals

Molybdenum (Mo) is used as a barrier metal in order to avoid intermixing of gold and aluminum. Ti/Al-based alloyed ohmic contacts showed an improved metal line definition and surface morphology. Ga in AlGa_N layer diffuses through the metal leaving behind Al-rich AlGa_N interface and reacts with Mo due to its high reactivity with Mo and hence forming the Ga-Mo₃ phase. Ga vacancies filled by N atoms which cause nitrogen vacancies. The high concentration of N vacancies results in heavy doping and hence reduces contact resistance [1,2].

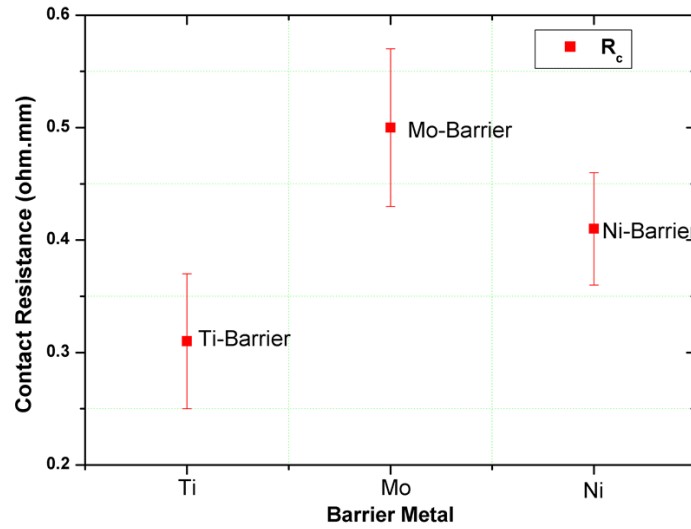
Al diffusion into the Ti barrier, on the other hand, introduces the Al-Ti phase which has a lower resistivity than that of Ti. Low contact resistance can be achieved by using Ti as a barrier metal.

Table 3.2 Ohmic Metal Stacks and Corresponding Contact Features

Metal Stacks (nm)	Sample Code	R_c (Ω .mm) R_s (Ω /sq)	Edge Definition (SEM Images)	Remarks
Ti-Al-Ni- Au 20-100- 40-50	Ni- Barrier	R_c : 0.41 R_s : 451		Smooth metal surface morphology Clear line definition Lower Contact resistance
Ti-Al-Mo- Au 20-100- 40-50	Mo- Barrier	R_c : 0.50 R_s : 424		Metal morphology got worse with Mo contact Line definition is not acceptable Lower Contact resistance
Ti-Al-Ti- Au 20-100- 40-50	Ti- Barrier	R_c : 0.31 R_s : 351		Metal morphology got worse with Ti contact Line definition is not acceptable Lower Contact resistance

Different barrier metals that were annealed at the same RTA condition (850 °C/30 sec) yielded similar contact resistance in between 0.3-0.4 ohm.mm but contact edge definitions were varying (see Figure 3.7.). The best edge definition was achieved using the Ni barrier comparing with Ti and Mo barrier.

a)



b)

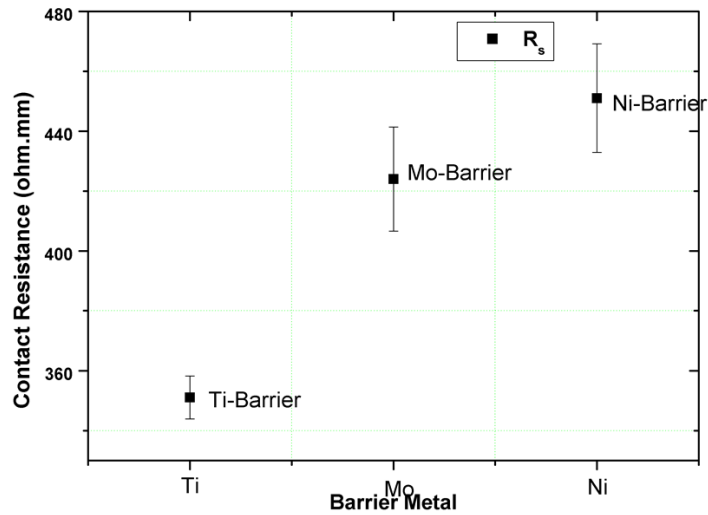


Figure 3.7. TLM Measurements of Ohmic Contacts with Different Barrier Metal a) Contact resistance (R_c) and b) Sheet Resistivity (R_{sh})

3.2 Non-Alloyed Recessed Ohmic Contacts to AlGaN/GaN HEMTs

For the re-growth InGaN process, the SiO₂ mask was deposited by PECVD as a regrown mask. The thickness of the SiO₂ mask was about 400 nm and contact pads were patterned by standard optical lithography using an appropriate resist and proper lithography parameters. Next, the ICP-RIE process was used in order to obtain recessed ohmic patterns. SiO₂ openings and recess etch patterns with a depth of ~80nm were formed for non-alloyed ohmic contacts by CF₄ and BCl₃/Cl₂ plasma, respectively. Wafer was loaded to the MOCVD chamber for re-growth of the InGaN layer with a thickness of about 90 nm. TMGa, TMI_n, and NH₃ sources were used to grown InGaN layers. The growth temperature was set to 825 °C with a pressure of 400 mbar. Following by SiO₂ mask removal and Cr-Au (20 nm-100 nm) evaporation without having any RTA treatment.

The simulation was carried out in order to have a band diagram of the junction at the interface according to experimental results published in our InGaN studies [67-68]. Figure 3.8 shows that In_{0.12}GaN with a carrier concentration above 10¹⁹cm⁻³ has an SBH of around 0.2 eV with a narrow peak profile. This simulation indicates that InGaN could have great potential for re-grown ohmic contact.

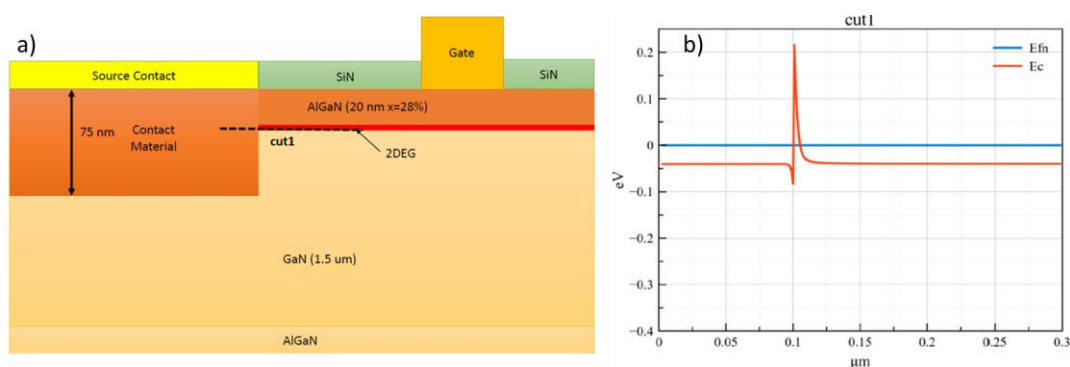


Figure 3.8. a) Cross Section of device and b) Schematics of Band Diagram of Junction

Sequential process flow for obtaining re-growth InGaN ohmic contacts on a patterned wafer is depicted in Figure 3.9, below. A corresponding Hall Effect Measurement of InGaN layers was shown in Figure 3.10.

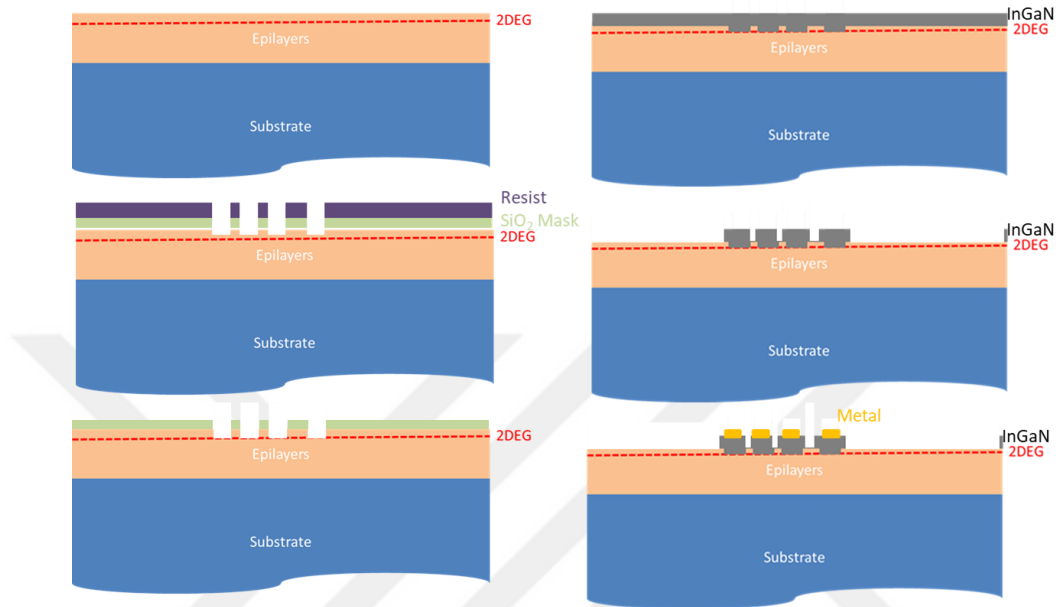


Figure 3.9. TLM Measurements of Ohmic Contacts with Different Barrier Metal

A bare sapphire substrate was co-loaded to the reactor chamber as well in order to obtain electrical properties of the InGaN layer.

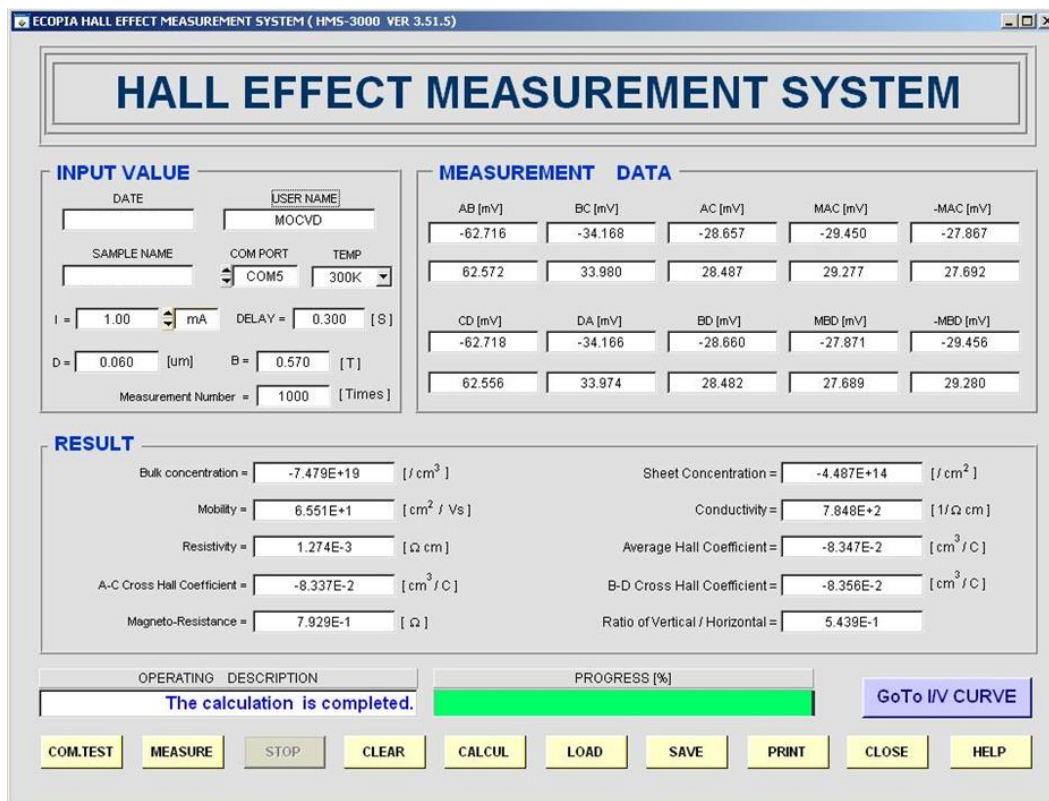


Figure 3.10. Hall Effect Measurement of InGaN Layer Grown on Co-Laded Sapphire Substrate

Table 3.3 Non-Alloyed Ohmic Contacts and Corresponding Contact Features

Metal Stacks	R_c (Ω .mm) R_s (Ω /sq)	Edge Definition
Cr- Au 20 nm- 100 nm	0.33 Ω .mm 471 Ω /sq	

Cr/Au-based metal stacks were used as an ohmic contact metallization for the HEMT structure under investigation. The electron-beam evaporation method was used to form ohmic contacts using standard photolithography methods. RTA process did not apply for non-alloyed ohmic contact which helps to have much better metal morphology as seen in SEM images. TLM measurements revealed that contact resistance was between $0.25 \Omega\cdot\text{mm}$ - $0.40 \Omega\cdot\text{mm}$ which is one of the best ohmic contact resistance achieved during our work. High carrier concentration in InGaN layers resulted in lower contact resistance due to lower and narrow SBH and promote carrier movement through the barrier as discussed in Chapter 2.3.1.

Although being a complicated process that adds several additional fabrication steps (sacrificial SiO₂, MOCVD re-growth, dry etch, etc.) it helps much to decrease contact resistance and improve surface morphology which is crucial for next coming fabrication steps. Non-alloyed ohmic contact process yield excellent edge definition compared to alloyed ohmic contacts which are a result of using the non-RTA process.

3.3 Fabrication of AlGaN/GaN HEMT for Ka Band Applications

Entire microfabrication processes were performed in the Nanotechnology Research Center (NANOTAM) at Bilkent University. In this part, the process flow of GaN-based HEMTs was described along with some key factors which are detrimental to process steps.

The outcome of both alloyed and non-alloyed ohmic contact optimizations which was described in previous Chapters 3.1 & 3.2 was implemented to the GaN-based HEMT processes for Ka-band applications.

3.3.1 Device Description and Process Technology

In this section, the processing steps of the HEMT device was described in detail including MOCVD growth of epilayers of AlGaN/GaN heterostructures on the

various substrate followed by wafer cleaning, ohmic contacts, Schottky contacts interconnect metallizations, passivation, and air-bridge technology.

Microfabrication steps and their sequence was described in detail. The individual step and cross-section of the device are shown in Figure 3.11.

Sample cleaning which is the very first step of the microfabrication process is important not only for photoresist adhesion but also for further microfabrication processing and proper device operation. Considering other III-V semiconductors, GaN and AlGaN have a unique surface. Solvent cleaning and wet etching using common acids/bases do not produce atomically clean surfaces. Cleaning and wet etching are effective in removing oxides and other contaminants.

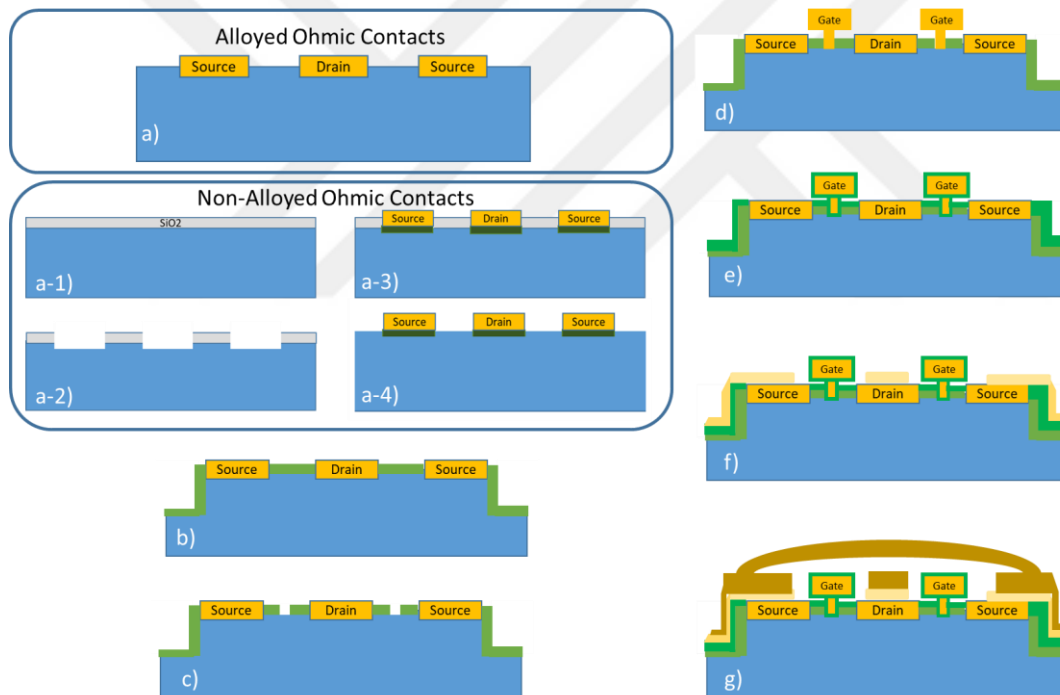


Figure 3.11. Descriptive Process Flow for GaN HEMT with Alloyed and Non-Alloyed Ohmic Contacts

There are organics and inorganics residues and native oxides (i.e. Ga_2O_3) on the surface of the AlGaN/GaN HEMT structure. Standart cleaning procedure with acetone and isopropyl alcohol is used to remove organic contaminants. Oxygen

plasma could be an alternative way of removing organics as well. In order to remove native oxide and inorganic parts NaOH, NH₄OH, and (NH₄)₂S are used. Common acids like HF and HCl are used for removing oxides. There are also some acid mixtures (HCl: H₂O, HCl: H₂O, aqua reggia and etc.) that were investigated in literature and elsewhere.

Microfabrication sequences of HEMT devices is described starting with ohmic contacts, mesa isolation, nitride passivation, gate formation, metal contact thickening, and ending with passivation and air-bridge formation. A sample of SEM photo which shows microphotography of fabricated HEMT with Source (S), Drain (D), Gate (G) contacts and their thickened metal pads.

- a) Alloyed Ohmic Contact Metalization Formation** (includes multiple steps)
- a- Non-Alloyed Ohmic Contact Formation**
 - a-1) SiO₂ Mask by PECVD for Re-Growth InGaN
 - a-2) Patterning of SiO₂ Mask and Recess Etching for Re-Growth InGaN (includes multiple steps)
 - a-3) MOCVD Re-growth InGaN and followed by Cr/Au by E-Beam Evaporator
 - a-4) SiO₂ Mask Removal
- b) Mesa isolation by BCl₃/Cl₂ plasma etching and PECVD Si_xN_y deposition** (includes multiple steps)
- c) T-Gate Lithography** (includes multiple steps)
- d) Gate Metalization by Ni/Au Evaporation by E-Beam Evaporator**
- e) Gate passivation by PECVD Si_xN_y**
- f) Interconnect Metalization**
- g) Air-Bridge Formation** (includes multiple steps)

SEM and FIB images of typical HEMT device fabricated at NANOTAM-Bilkent University with an L_g of 0.15μm and multiple fingers are shown in Figure 3.12.

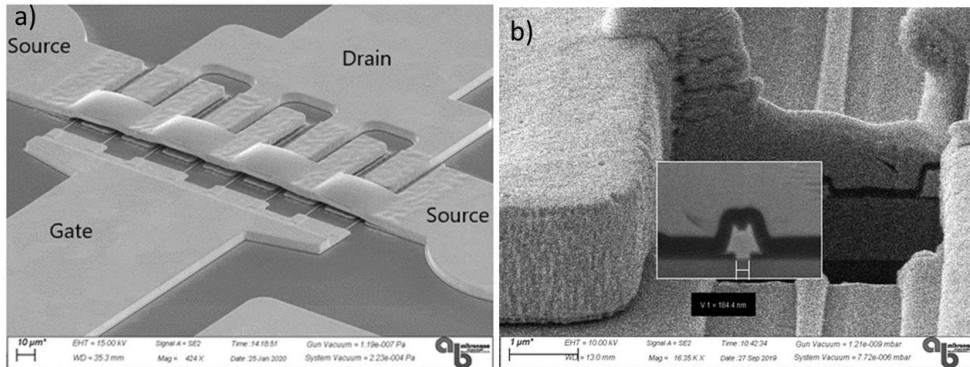


Figure 3.12. Microphotograph of a sample HEMT structure with S, D, and G contacts
 a) SEM image and b) FIB image

3.3.1.1 MOCVD Growth of AlGa_N/Ga_N Heterostructure

To develop an epitaxial layer designed for K_a-band (26.5-40 GHz) is the heart of the HEMT device. Individual layers have to be considered carefully.

AlGa_N/Ga_N HEMT structure normally employs doped Ga_N buffer with carbon or iron to reduce leakage current through unintentionally doped buffer during growth conditions. Trapping effects due to the acceptor level of the dopant carbon or iron atoms alleviated by adding a ‘transition Ga_N buffer’ between 2DEG and doped Ga_N region. There have been several studies reported in literature without using doped Ga_N buffer and a commercial epi-wafer has been also released by SweGa_N [3-6].

More detailed explanations regarding the growth mechanisms of Ga_N on SI-SiC and sapphire have been already reported by A. Grzegorzcyk [7] and Mariusz Rudzinski [8], respectively.

GaN device for the Ka-band application requires a high-frequency response compared to other microwave applications. Special consideration should be given to the determination of the Al composition and layer thicknesses of the AlGa_N barrier. To avoid the short channel effect [9], both gate length (L_g) and thickness of the AlGa_N barrier should be carefully considered. Ga_N HEMT devices require an aspect

ratio (L_g/t_{channel}) over 10 where this value is between 3-6 for GaAs devices [10-11]. Table 3.4 shows the GaN HEMT results of several groups for Ka-band applications.

Table 3.4 GaN HEMT for K_a Band [12]

Groups	% Al	d _{AlGaN} (nm)	L _g (μm)	Aspect Ratio (L _g /d _{AlGaN})	f _{max} @ V (GHz)	Operation f (GHz)	Operation Voltage (V)
HKUST	26	18	0.2	9.5	180 @24	-	-
ETH-Zurich	26	17.5	0.2	10.2	118 @10	40	20
IEMN	26	12.5	0.125	8.6	125 @4	-	-
IEMN	100	6	0.1	16.6	192 @15	40	15
NEDI	28	20	0.15	10	63 @24	35	24
Triquint	31.5	-	0.25	-	-	35	20
Toshiba	30	-	0.18	-	-	31	24
UCSB	32	25>12	0.16	13.3	155 @5	30	30
Toshiba	30	15	0.15	10	140 @24	28	24

In this study, epitaxial structures of AlGaN/GaN HEMTs were grown on SI-SiC substrates using the Aixtron Epilab II MOCVD system. Before starting epitaxial growth a nitridation step was applied for 3 min. A 0.1 μm HT AlN buffer was grown at 1120 °C, followed by a 1.2 μm Fe-doped ud-GaN layer grown at 1050 °C. To prevent 2DEG electrons from trapping and uid-GaN layer was grown between 2DEG and Fe-doped GaN layer with a thickness of 0.7 μm. An ud-GaN channel with a low carbon concentration ($<1 \times 10^{16} \text{ cm}^{-3}$) grown at relatively higher growth pressure with a thickness of 0.2 μm. A 1nm thick AlN spike layer followed by a 20-22 nm Al_{0.29}GaN barrier layer and epitaxial growth ended up a 2 nm thick GaN cap layer. The use of AlN spike layer between the Al_{0.29}GaN barrier layer and ud-GaN channel is to enhance electron mobility and electron confinement in the 2DEG channel.

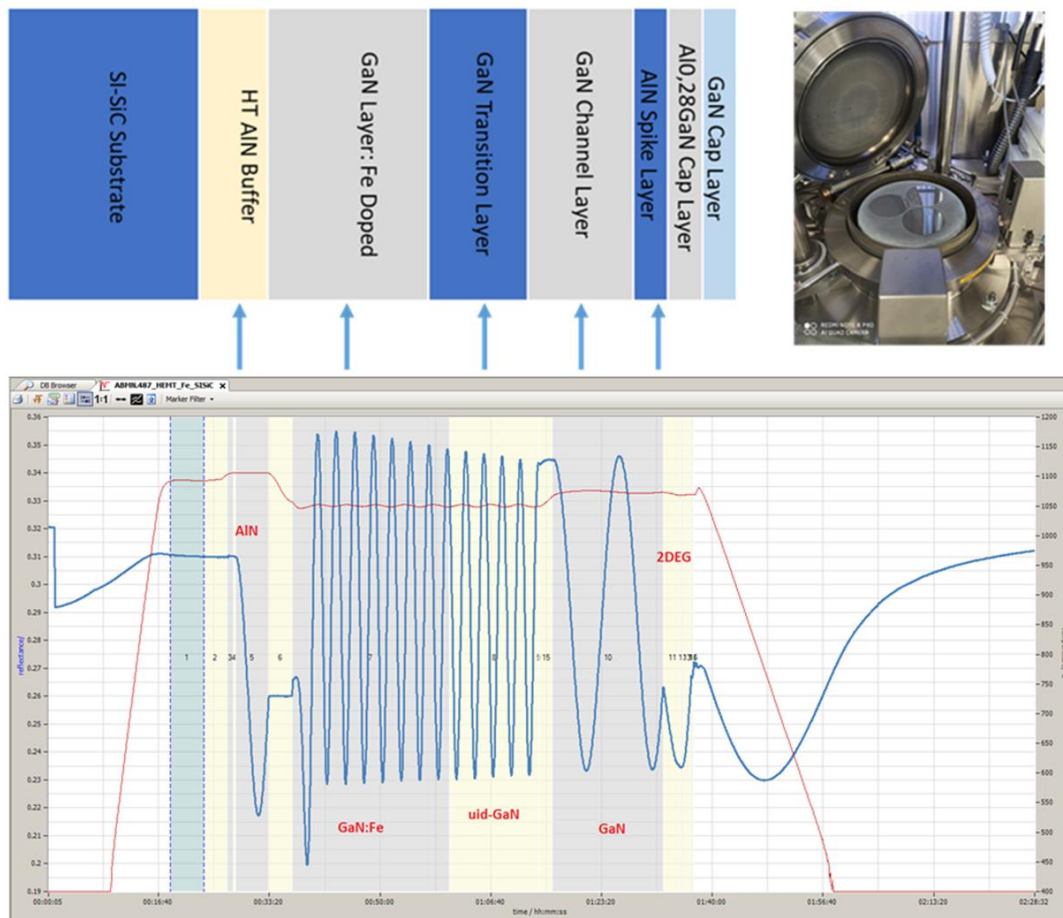


Figure 3.13. Structure of AlGaN/GaN HEMT on 3'' SI-SiC by MOCVD

During growth, in-situ laser reflectance interferometry was performed in order to monitor growth rate, surface roughness, and layer thickness, which is shown in Figure 3.13. Wafer bow was below $5\mu\text{m}$ and curvature was almost zero.

To investigate the material properties of HEMT epi-wafers non-contact and non-destructive measurements were performed. Leighton Contactless Mobility Mapping system was used to investigate 2DEG properties as shown in Figure 3.14. Measurements showed that HEMT on 3'' SI-SiC wafer has a N_b of $1.24 \times 10^{13} \text{ cm}^{-3}$, μ of $1877 \text{ cm}^2/\text{V.s}$, and sheet resistance (ρ) of $256 \Omega/\text{sq}$.

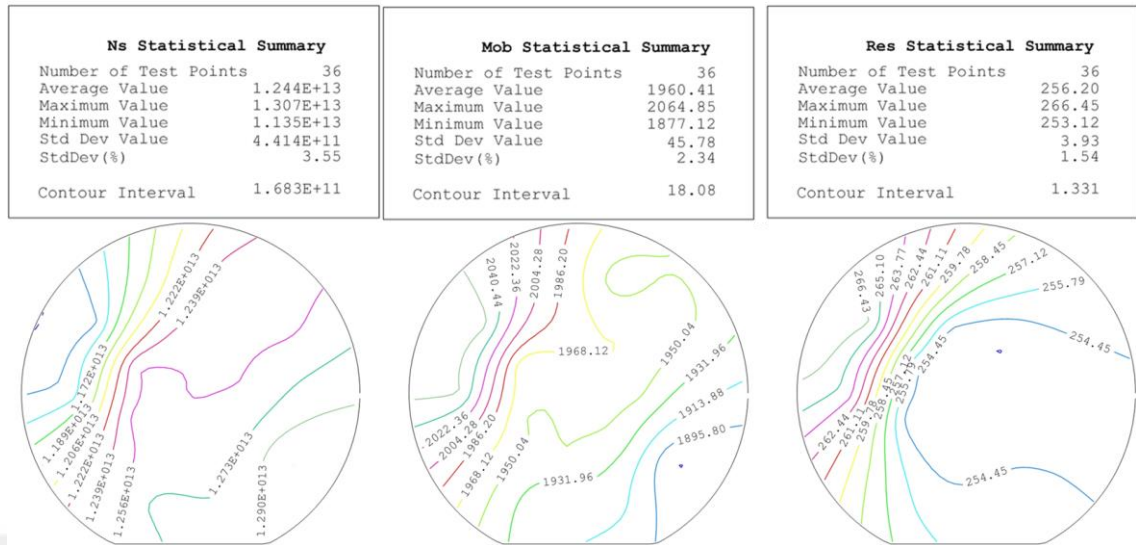


Figure 3.14. 2DEG Properties of HEMT on 3'' SI-SiC

Al content of the AlGa_N barrier layer and its uniformity over 3'' SI-SiC substrate was measured by the Nanometrics PL system which is shown in Figure 3.15. Measurements showed that Al composition was 28.7% and deviation was below 3%. The emission wavelength of the AlGa_N barrier was around 315 nm and the deviation was below 0.4% which indicates that the CCS reactor produces quite uniform epilayers on a 3'' substrate.

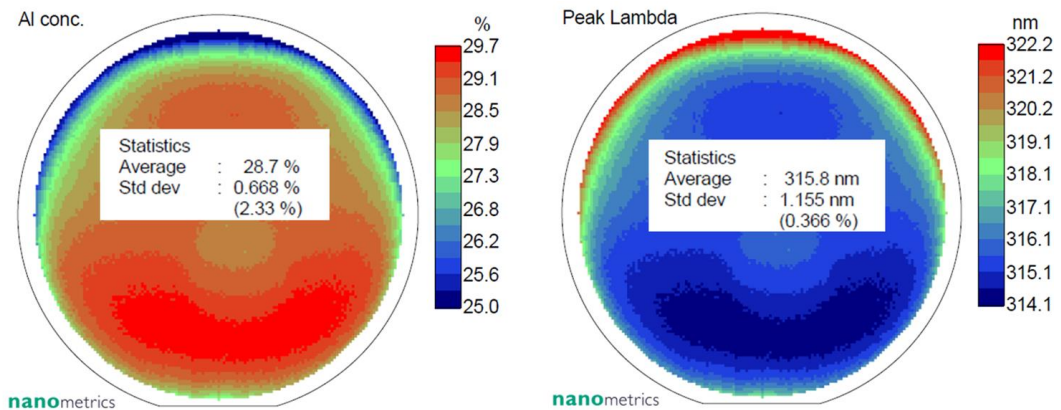


Figure 3.15. a) Al composition and b) emission wavelength of AlGa_N Barrier layer of HEMT structure on 3'' SI-SiC

X-ray analysis was performed to investigate the crystal quality of the AlGaN/GaN HEMT structure. The asymmetric ω - 2θ spectrum is shown in Figure 3.16. Individual peaks are seen in the spectrum and Kiessig fringes [13] are easily seen in the spectrum which is evidence of the smooth surface of the grown epilayers. AlN (002) and GaN (002) reflections are seen at 34.5° and 36° , respectively.

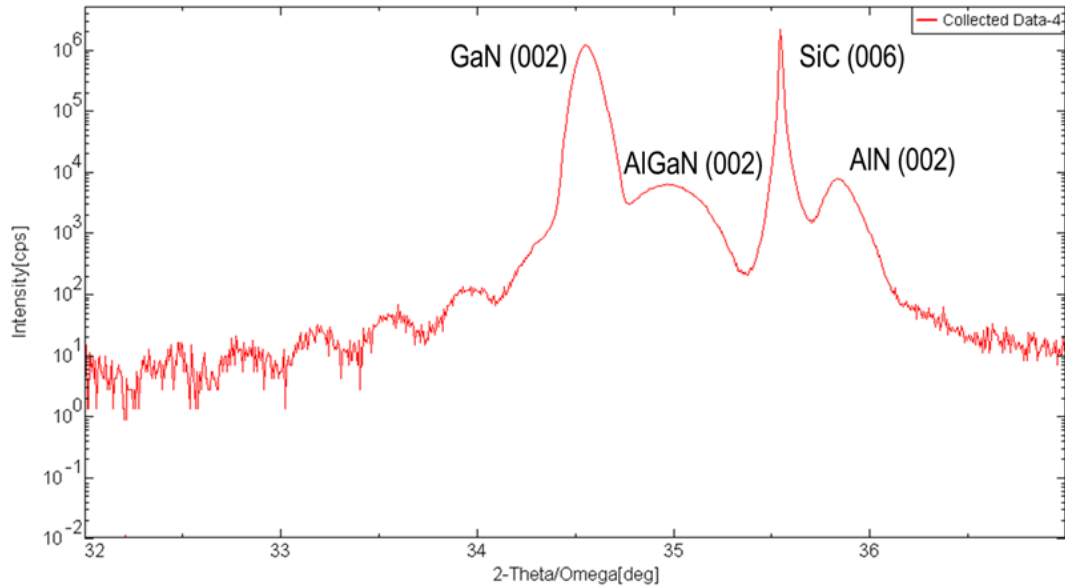


Figure 3.16. 2Theta-Omega Reflection of GaN HEMT on SI-SiC

In order to assess the crystal quality symmetric (002) and asymmetric (102) scans were performed which is a reliable method for film quality. Screw and mixed time threading dislocations (TD) results in a broadening of FWHM of (002) scans while FWHM of (102) are affected by all types of dislocations [14-15].

As seen in Figure 3.17, the rocking curves were measured around the (002) and (102) reflections of the GaN layers and exhibited a FWHM of 209 arcsec and 284 arcsec, respectively. Such low FWHM values indicate that GaN grown on SI-SiC has low dislocation density which is important for GaN RF devices.

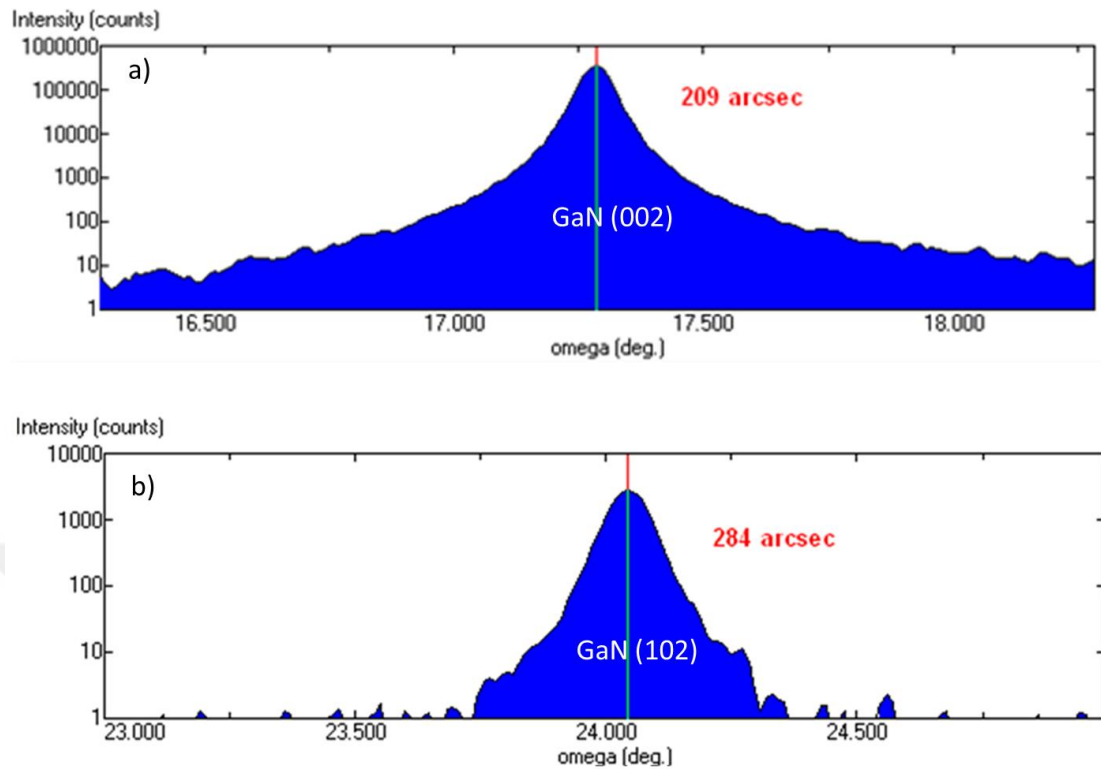


Figure 3.17. a) Omega Scan of 002 and b) 102 reflection of GaN HEMT on SI-SiC

3.3.1.2 Alloyed and Nonalloyed Ohmic Contacts

Quality of the ohmic contacts of the HEMT device is one of the most important parameters that affect device performance. Since HEMTs are small voltage and large current devices, transconductance and saturation currents depend on the quality of metal contacts and hence their resistance. It is very important to have lower ohmic contact resistance for HEMT devices where the 2DEG region is approximately 20-30 nm deep from the surface. Due to its wide bandgap nature, it is important to choose proper metal for both lower Schottky Barrier height to AlGa_N (GaN) and good adhesion. Schematic illustration of both alloyed and non-alloyed InGa_N regrown ohmic contacts are shown in Figure 3.18, below.

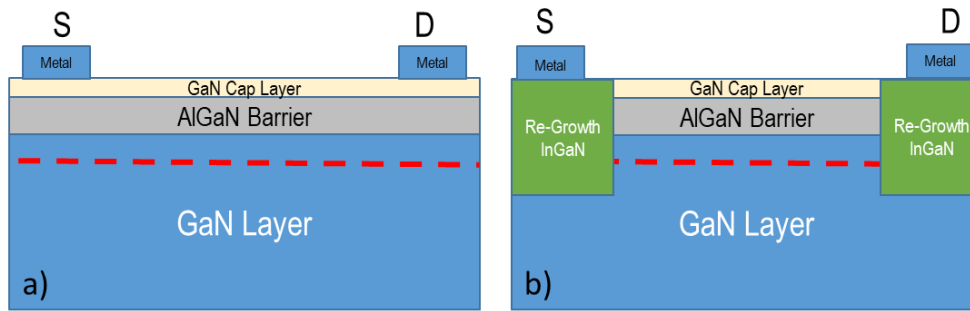


Figure 3.18. Schematic illustration of a) Alloyed and b) Non-Alloyed Ohmic Contacts

In the case of alloyed ohmic contacts, microfabrication starts with wafer cleaning with solvent or acids, ohmic contact pads were formed by optic lithography using an appropriate resist and proper lithography parameters for alloyed ohmic contacts. Contacts were deposited on the patterned surfaces via e-beam lithography. The metal stacks were arranged according to lower ohmic contact resistance and better edge acuity. Ti-Al-Ni-Au metals were evaporated with a thickness of 20 nm, 100 nm, 40 nm, and 50 nm, respectively. The Source-Drain spacing is 2.5 μm . Metal contacts were annealed at 850 $^{\circ}\text{C}$ /30 sec under N_2 ambient. TLM measurements were showed that contact resistance (R_c) was 0.43 $\Omega\cdot\text{mm}$.

Figure 3.19 shows the micrograph of patterned metal contacts before and after RTA processes. It is important to obtain smoother surface morphology of metal contacts for the next coming process steps. Deterioration in edge acuity of metal contact not only affects microfabrication processes but also affects the device performance.

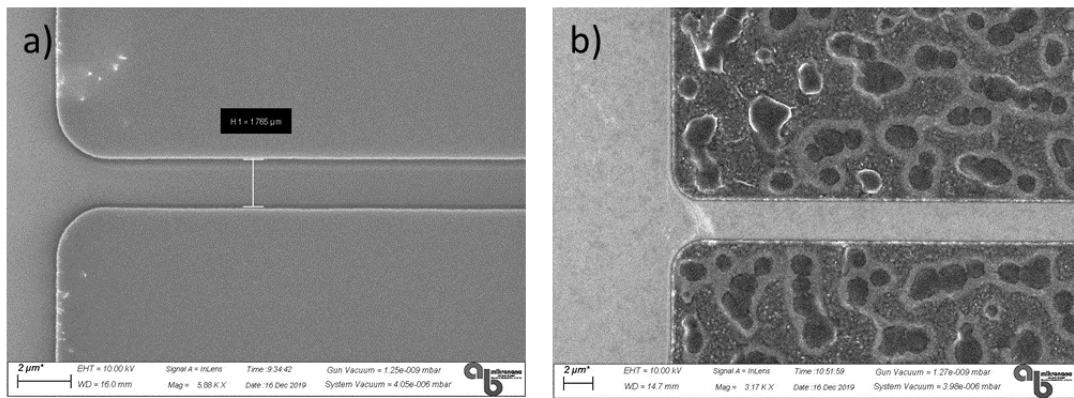


Figure 3.19. Microphotograph of Alloyed-Metal Contact Source and Drain a) before and b) after RTA Processes

Non-alloyed ohmic contacts, microfabrication starts with wafer cleaning with solvent and acids in order to remove surface contaminants and followed by SiO_2 mask which was deposited with PECVD. The thickness of the SiO_2 mask is about 400 nm and contact pads were patterned by optic lithography using an appropriate resist and proper lithography parameters. Next, the ICP-RIE process was used in order to obtain recessed ohmic patterns. SiO_2 openings and recess etch patterns with a depth of ~ 80 nm were formed for non-alloyed ohmic contacts by CF_4 and BCl_3/Cl_2 plasma, respectively. Wafer was loaded to the MOCVD chamber for re-growth of the InGaN layer with a thickness of about 90 nm.

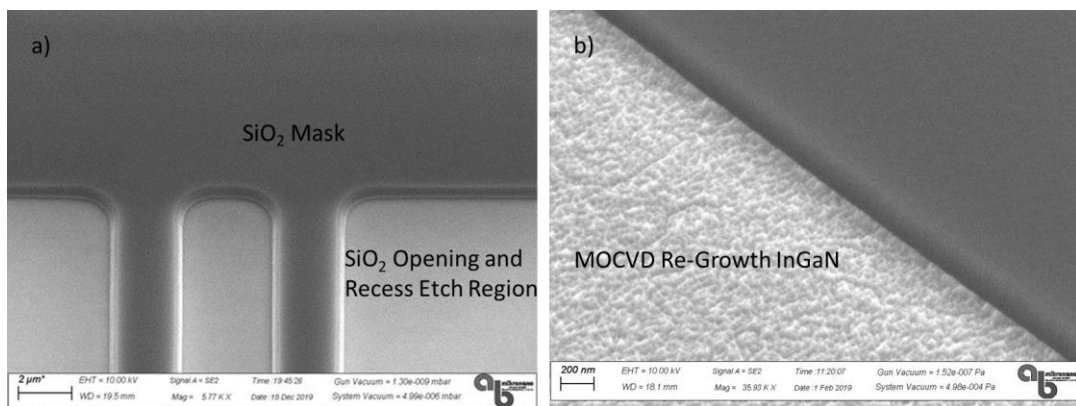


Figure 3.20. Microphotograph of Non-alloyed-Metal Contact Source and Drain a) before and b) after MOCVD Re-Growth of InGaN

Carrier concentrations of MOCVD Re-Growth InGaN Layer were measured by Hall Effect measurement from the co-loaded sapphire (see Figure 3.21) substrate where InGaN thickness was ~90 nm. It is clearly seen that carrier concentration above 10^{20}cm^{-3} which indicates that the layer was degenerately doped. This doping level is desired for pushing fermi level downwards, enhance field emission of charge carriers and results in a decrease of contact resistance.

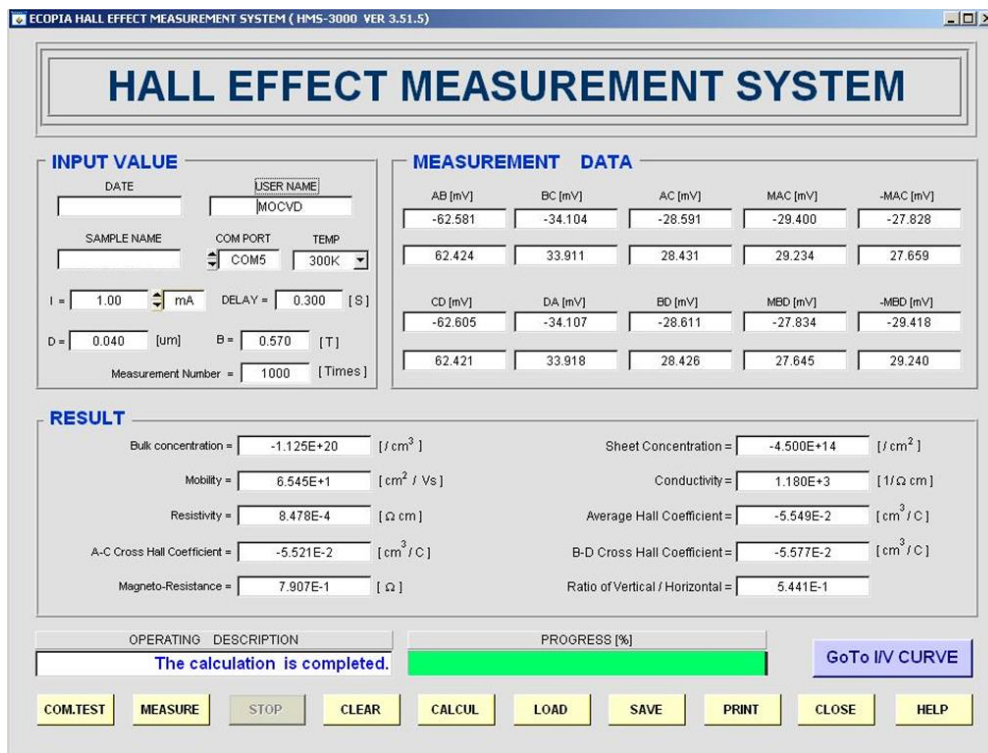


Figure 3.21. Hall Effect Measurement of Re-Growth InGaN Layer grown on co-loaded 3'' Al₂O₃ substrate

Next, the SiO₂ mask was removed by diluted HF, and Cr/Au ohmic contact pads were patterned by optic lithography and followed by evaporation of Cr (10 nm) /Au (100 nm) metals for non-alloyed ohmic contacts. A stabilization bake was performed at 250 °C for 30 sec under N₂ ambient. SEM images of the non-alloyed ohmic contacts with Cr/Au metal can be seen in Figure 3.22, below. Sharp and clear metal edges and smooth surface morphologies are an indication of better alignment of gate metals and enhance device performance.

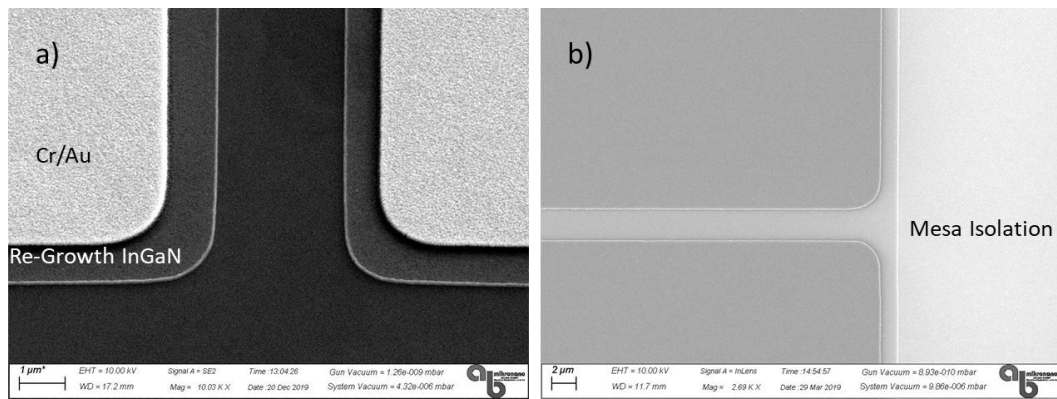


Figure 3.22. Microphotograph of a) Non-alloyed-Metal Contact with Cr/Au metal and b) Mesa Isolation of Active Region

As seen in Figure 3.23., TLM measurements were showed that the total contact resistance ($R_{c-total}$) of non-alloyed ohmic contact was $0.30 \Omega \cdot \text{mm}$ which was well below alloyed ohmic contact resistance of $0.43 \Omega \cdot \text{mm}$.

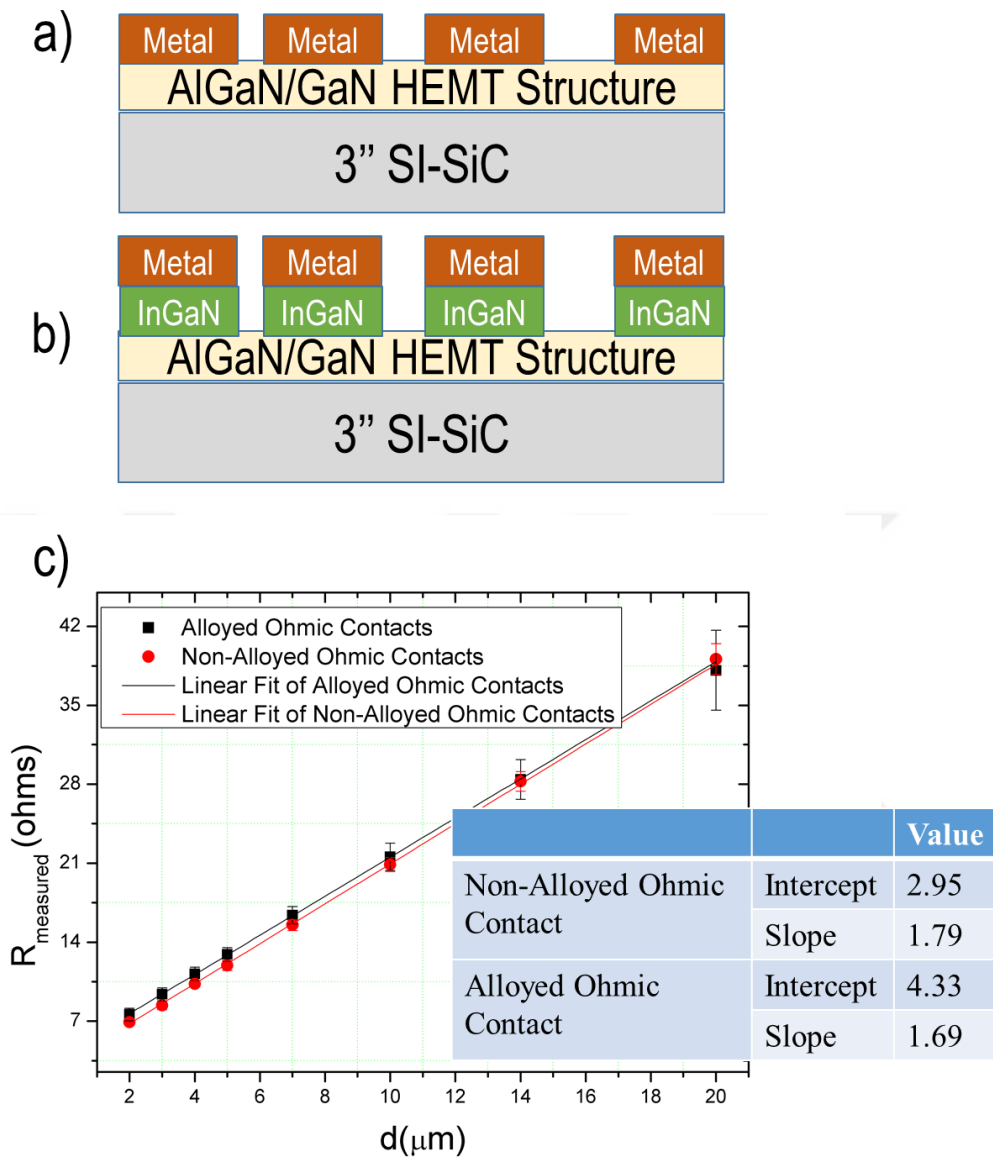


Figure 3.23. TLM measurement of a) Ti-Based alloyed ohmic contacts, b) MOCVD regrown InGaN non-alloyed ohmic contacts, and c) resistance versus contact spacing

Table 3.5. shows the TLM results of both alloyed and non-alloyed ohmic contact. Non-Alloyed ohmic contact yielded not only a smooth surface which is important for the next coming fabrication steps but also a lower $R_{c-total}$ value which is critical for device performance such as I_{ds} , g_m , and f_t .

Table 3.5 TLM Results of Alloyed and Non-Alloyed Ohmic Contacts

Process	$R_{c-total}$ ($\Omega \cdot mm$)	R_{sh} (Ω/sq)
Non-Alloyed Ohmic Contact	0.30	359
Alloyed Ohmic Contact	0.43	339

Additional TLM measurements were also conducted in order to investigate individual components of total contact resistance (R_{c-tot}) for MOCVD regrown InGaN nonalloyed ohmic contacts where metal/InGaN contact resistance R_c , InGaN access resistance R_{InGaN} and InGaN/2DEG interface $R_{interface}$ as shown in Figure 3.24, below.

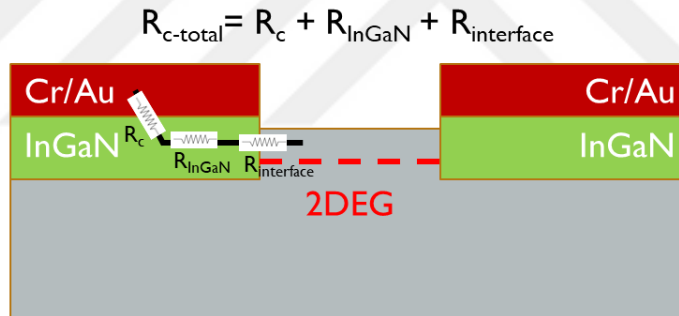


Figure 3.24. Components of Total Contact Resistances, R_{c-tot} , of MOCVD regrown InGaN nonalloyed ohmic contacts

Figure 3.25. shows that the TLM measurement of metal/InGaN layers. The contact resistance (R_c) was around $0.07 \Omega \cdot mm$ and the sheet resistance, R_{sh} , of InGaN $62 \Omega/sq$. The lower value of R_c than other reported values was due to the degenerately doped InGaN layers [17].

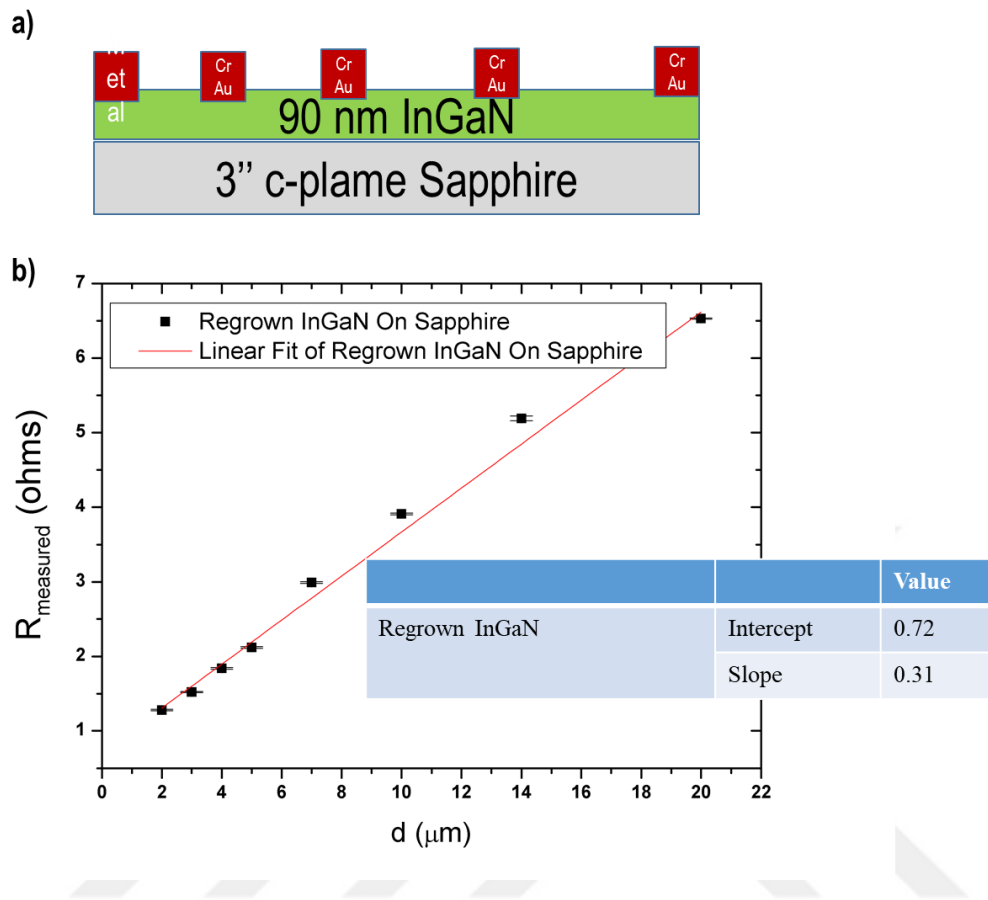


Figure 3.25. Ohmic contact patterns for MOCVD growth of InGaN on sapphire (a) and resistance versus contact spacing (b)

3.3.1.3 Mesa Isolation and Passivation

In order to have mesa isolation, a 100 nm deep mesa etch process was performed by BCl_3/Cl_2 plasma for both alloyed and non-alloyed ohmic contacts. The rest of the process technology for GaN HEMT was identical in order to compare alloyed and non-alloyed ohmic contacts on the performance of HEMT devices for Ka-band applications. Devices were passivated with a PECVD Si_xN_y layer with a thickness of 100 nm.

3.3.1.4 T-Gate Formation and Gate Passivation

In order to have T-shaped gate geometry, two steps of E-beam lithography with PMMA were carried out. The gate length (L_g) was $0.15\ \mu\text{m}$ and the gate head was $0.50\ \mu\text{m}$ (see Figure 3.26.)

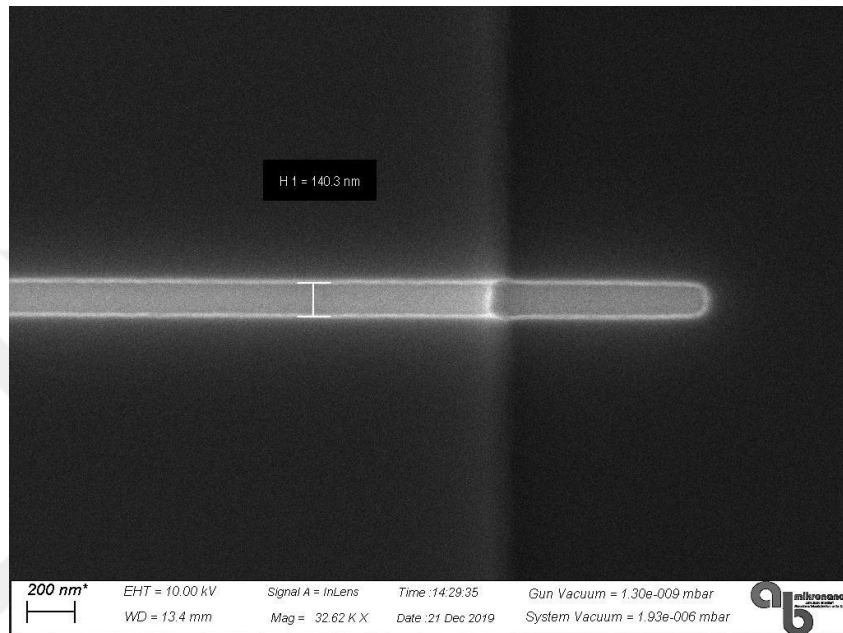


Figure 3.26. Microphotographs of $0.15\ \mu\text{m}$ Gate Foot patterned by Electron-Beam Lithography

A Ni/Au metal stacks were deposited for Schottky contacts. An RTA process was performed at $300\ ^\circ\text{C}$ for 5 min under the N_2 ambient for stabilization. The Source-Drain spacing is $2.5\ \mu\text{m}$ and the Gate was placed at the center between source and drain contacts.

Scanning Electron Microscopy (SEM) images of AlGaIn GaN HEMT with an L_g of $0.15\ \mu\text{m}$ is shown in Figure 3.27, below.

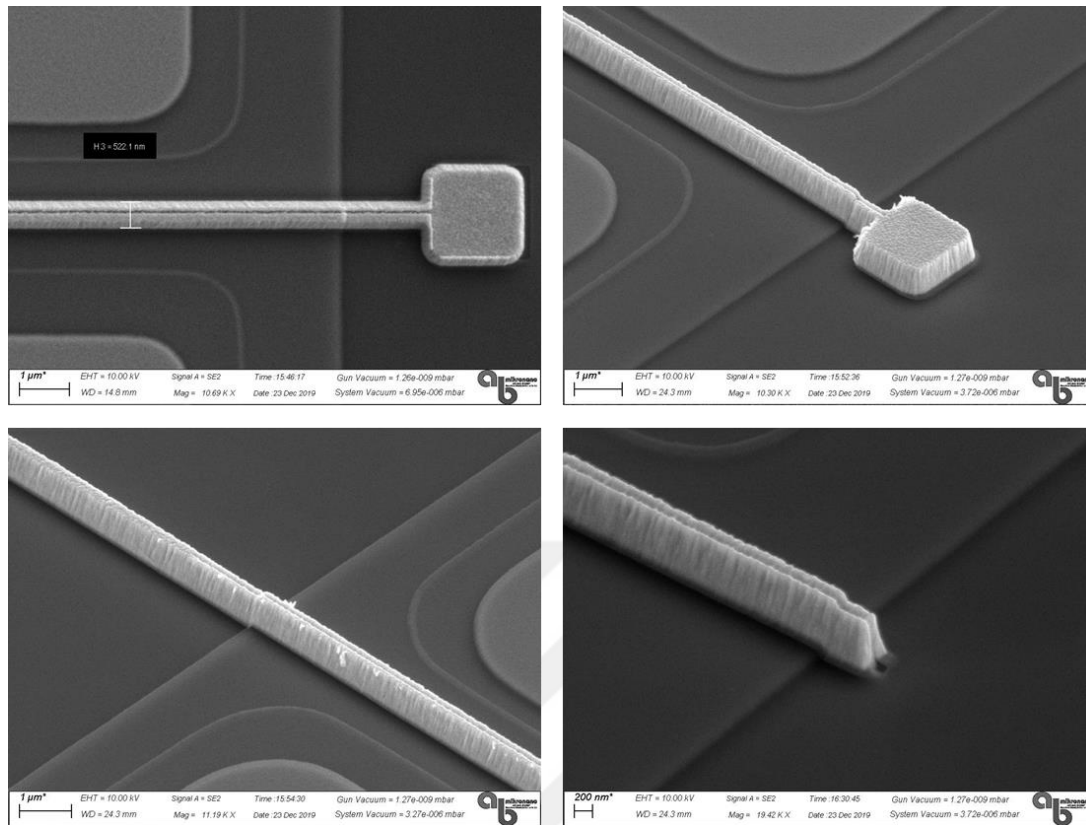


Figure 3.27. Microphotographs of 0.15µm Gate Foot patterned by 2-steps of Electron-Beam Lithography

3.3.1.5 Interconnect Metallization and Air Bridge Formation

Metal pads were thickened by the deposition of Ti/Au metals after necessary optical lithography in order to have better contacts. Lifted metal lines –Air Bridges are necessary to connect multiple sources in our process to make sources in equipotential which are seen in Figure 3.28 below. Air Bridges have defined special lithography processes followed by electroplating of gold metal with a thickness of around 4µm.

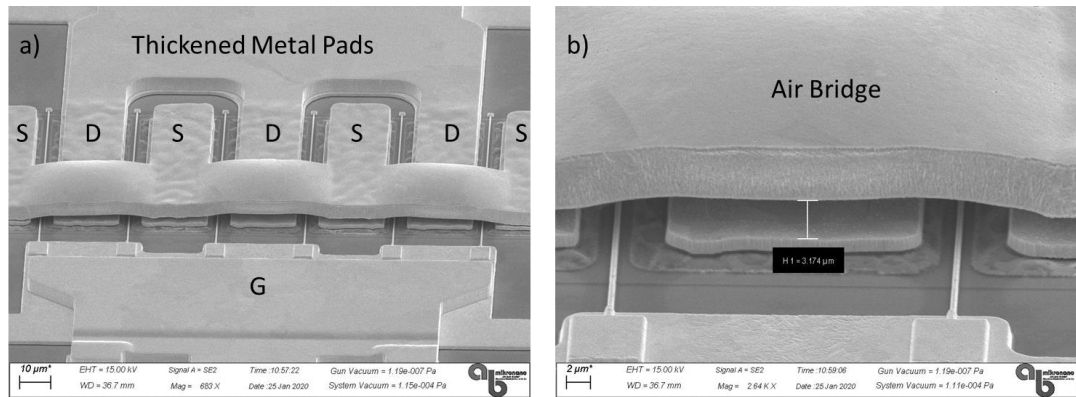


Figure 3.28. Microphotographs of a) Thickened Metal Pads and b) Air-Bridges by Electroplating Process

3.4 DC Characterization of HEMT with Alloyed and Nonalloyed Ohmic Contacts

Typical drain output characteristics are shown in Figure 3.29. The linear region where drain current (I_{ds}) is proportional to the drain-source voltage (V_{ds}) and the saturation region where I_{ds} is quasi-independent of drain-source voltage (V_{ds}).

Output characteristics, which is seen in Figure 3.29, of the fabricated devices with alloyed and non-alloyed ohmic contacts were measured where source-drain spacing (S-D) is $2.5 \mu\text{m}$, and gate length (L_g) is $0.15 \mu\text{m}$.

On resistances (R_{on}) which highly depends on contact resistance, R_c , were extracted from output characteristics. R_{on} obtained corresponding to Non-Alloyed and Alloyed Ohmic contacts are $2.74 \Omega.\text{mm}$ and $3.18 \Omega.\text{mm}$, respectively. In order to decrease power losses, one should need to decrease on-resistance, R_{on} .

Maximum drain current density (I_{ds}) of 0.94 A/mm and 0.88 A/mm were obtained for the sample with non-alloyed ohmic contacts and alloyed ohmic contacts, respectively at $V_{gs}=1 \text{ V}$. It clearly shows that higher contact resistance for alloyed ohmic contacts has significant effects on I_{ds} . It is widely known that the RF output power of a transistor is directly proportional to maximum available drain current

density, I_{ds} . It implies that it is crucial to improve I_{ds} in order to increase the output power of a transistor.

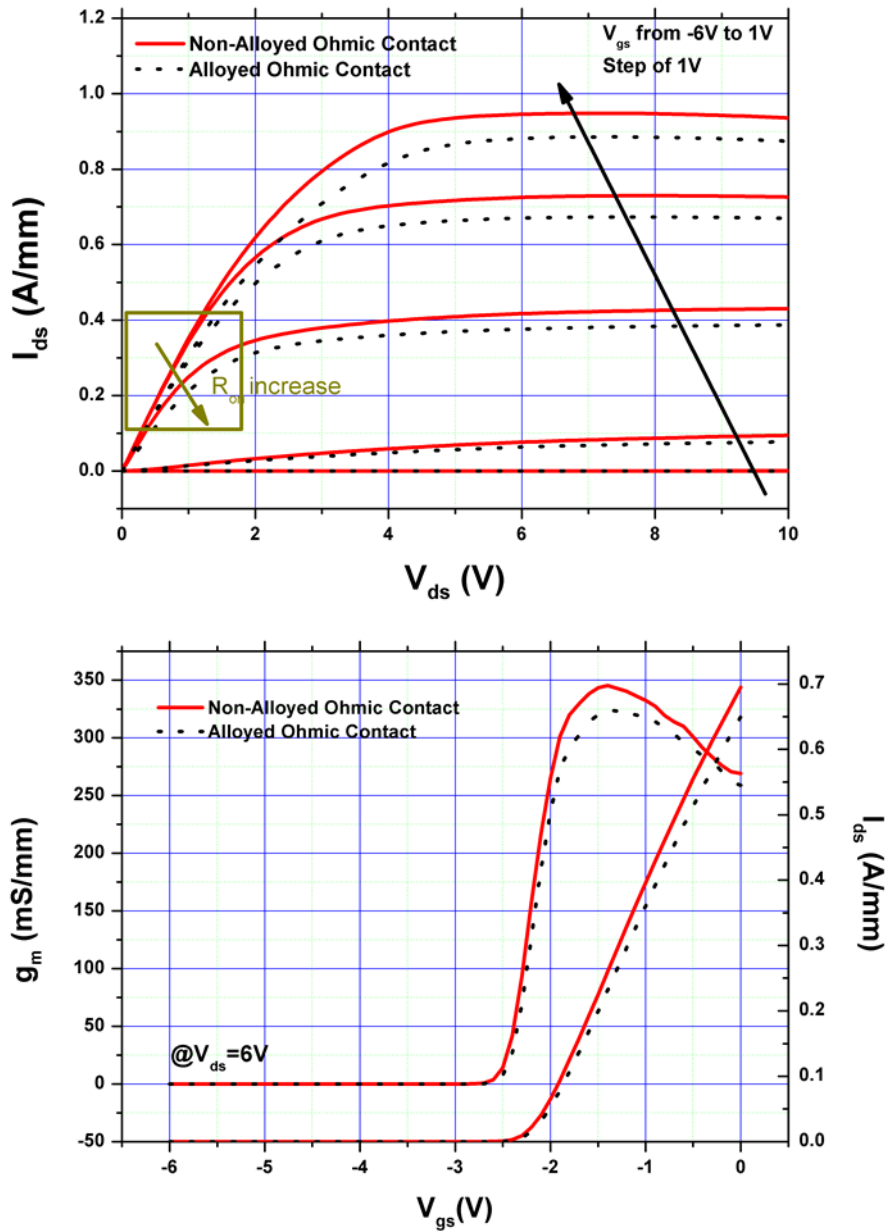


Figure 3.29. DC Characteristic of Alloyed and Non-Alloyed HEMT with $L_g=0.15 \mu\text{m}$ ($2 \times 50 \mu\text{m}$), S-D Spacing is $2.5 \mu\text{m}$

Knee Voltages, V_{knee} , were also extracted from output characteristics which also highly depends on contact resistance. Increasing contact resistance (R_c) increases V_{knee} as well, and results in lower output power as seen in the formula below where P_{out} could be expressed in terms of V_{knee} and $V_{breakdown}$ voltages;

$$P_{out} = \frac{1}{8} \times I_{ds} \times (V_{breakdown} - V_{knee}) \quad (\text{Eq. 3.7})$$

As seen from Eq. 3.7, it is desirable to have lower V_{knee} (V) for better DC and RF performance. V_{knee} voltages were 3.9 V and 4.2 V for non-alloyed ohmic contacts and alloyed ohmic contacts, respectively.

The maximum transconductance, g_m , obtained for non-alloyed ohmic contacts and alloyed ohmic contacts were 337 mS/mm and 314 mS/mm, respectively. The highest value of g_m is important in order to push the cut-off frequency (f_t) to higher values.

$$f_t = [2\pi(\frac{L_g}{v_e} + C_{gs}(R_s + R_d))]^{-1} \quad (\text{Eq. 3.8})$$

Table 3.6 Comparison of Output Characteristics of HEMT with Alloyed and Non-Alloyed Ohmic Contacts

	W (μm)	L_{DS}/L_g (μm)	R_c ($\Omega.\text{mm}$)	R_{on} ($\Omega.\text{mm}$)	I_{ds} (A/mm)	g_m (@6V) (mS/mm)	V_{knee} @ $V_{gs}=1\text{V}$
Non-Alloyed Ohmic Contact			0.30	2.74	0.94	337	3.9
Alloyed Ohmic Contact	2x50	2.5 / 0.15	0.43	3.18	0.88	314	4.2

It is clearly seen that non-alloyed ohmic contacts have significantly improved DC characteristics of the fabricated transistors by decreasing contact resistance, R_c . Lower access resistance and on-resistance improved output characteristics compared

to alloyed ohmic contacts. These results showed the potential of non-alloyed ohmic contacts for improving the high-frequency performance of the transistor.

3.5 RF Characterization of HEMT with Alloyed and Nonalloyed Ohmic Contacts

The cutoff frequency, f_t , and the maximum frequency of oscillation, f_{max} , are two important parameters for evaluating device performance where f_t is the frequency at which the current gain is equal to unity and the f_{max} is the frequency at which the maximum available gain or unilateral power gain U is equal to unity.

Figure 3.30 shows the evolution of the f_t and f_{max} from the magnitudes in decibels versus frequency. The extrapolation by a slope of -20 dB/dec helps to evaluate f_t and f_{max} for devices having alloyed and non-alloyed ohmic contacts.

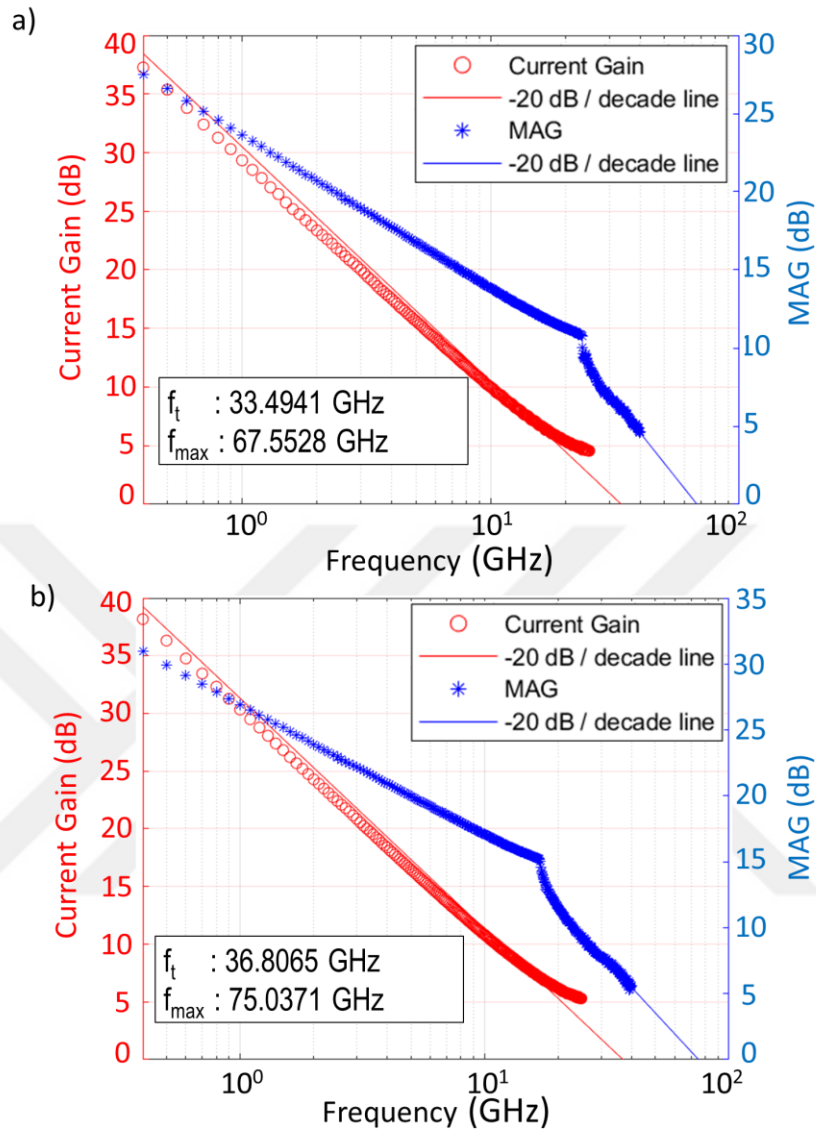


Figure 3.30. Small Signal RF Performance of a) Non-Alloyed and b) Alloyed HEMT with $L_g=0.15 \mu\text{m}$ and S-D Spacing is $2.5\mu\text{m}$

Utilizing non-alloyed ohmic contacts by using MOCVD re-growth of heavily doped InGaN under evaporated metalization allowed us to remove high-temperature annealing. This technique helps us to improve contact resistance of drain and source and surface morphology of the deposited metal pads which is crucial for further device fabrication processes.

The difference in high-frequency performance was attributed to the lower contact resistances (see Eq.3.8) and higher gm. This result is consistent with the well-known expression for the limiting frequency of current amplification f_t . Here, R_s and R_d are resistances of the source and drain, C_{gs} is the gate-source capacitance, and v_e is the drift velocity of electrons. Lower contact and on-resistance, better transconductance, and higher f_t and f_{max} were demonstrated, see Table 3.7, compared to alloyed ohmic contacts.

The dependence of f_{max} to f_t can be expressed as follows;

$$f_{max} \approx \frac{f_t}{2\sqrt{(R_i + R_s + R_g)g_{ds} + (2\pi f_t)R_g C_{gd}}} \quad (\text{Eq. 3.9})$$

R_i , R_s , and R_g are channels, source, and gate resistance, respectively. C_{gd} is the gate-drain parasitic resistance, g_{ds} is the output conductance.

Throughout equations 3.8 and 3.9, the improvement of the frequency performance of the fabricated AlGaIn/GaN HEMT's could be made by improving ohmic contact characteristics.

For alloyed ohmic contacts, a cut of frequency (f_t) of 33.5 GHz and maximum oscillation frequency (f_{max}) of 67.5 GHz were obtained on the gate length of 0.15 μm with a device geometry of 6x75 μm and S-D spacing was 2.5 μm .

For non-alloyed re-grown InGaIn ohmic contacts, a cut of frequency (f_t) of 36,8 GHz and maximum oscillation frequency (f_{max}) of 75.0 GHz were obtained on the gate length of 0.15 μm with a device geometry of 6x75 μm and S-D spacing was 2.5 μm . A notable improvement of small-signal performance, with lower R_{on} and higher g_m , were obtained for non-alloyed re-growth InGaIn ohmic contacts compared to alloyed ohmic contacts.

InGaIn re-growth contacts have been used to have non-alloyed ohmic contacts in AlGaIn/GaN HEMTs for K_a-band applications which improved not only for contact

resistance but also surface morphology which is crucial for next coming alignment steps.

Table 3.7 Comparison of f_t and f_{max} for AlGaIn/GaN HEMT with Alloyed and Non-Alloyed Ohmic Contacts

	W (μm)	L_{DS}/L_g (μm)	F_t (GHz)	F_{max} (GHz)	MAG (dB) @37GHz
Alloyed Ohmic Contact	6x75	2.5 / 0.15	33.5	67.5	5.2
Non-Alloyed Ohmic Contact			36.8	75.0	6.4

Load-pull measurements were done using the on-wafer measurement system from Maury Microwave in order to compare the power performance of the fabricated HEMTs with alloyed and non-alloyed ohmic contacts at 35GHz for the fabricated 6x75 μm (0.45 mm) devices with an L_g of 0.15 μm . The devices were biased at $V_{ds}=20$ V with a quiescent current of 100 mA/mm.

Figure 3.31 shows active load-pull results of both HEMT with alloyed and non-alloyed ohmic contacts. HEMT with alloyed ohmic contacts exhibited a linear gain of above 6.6 dB which is 0.3 dB higher compared to HEMT with alloyed ohmic contacts.

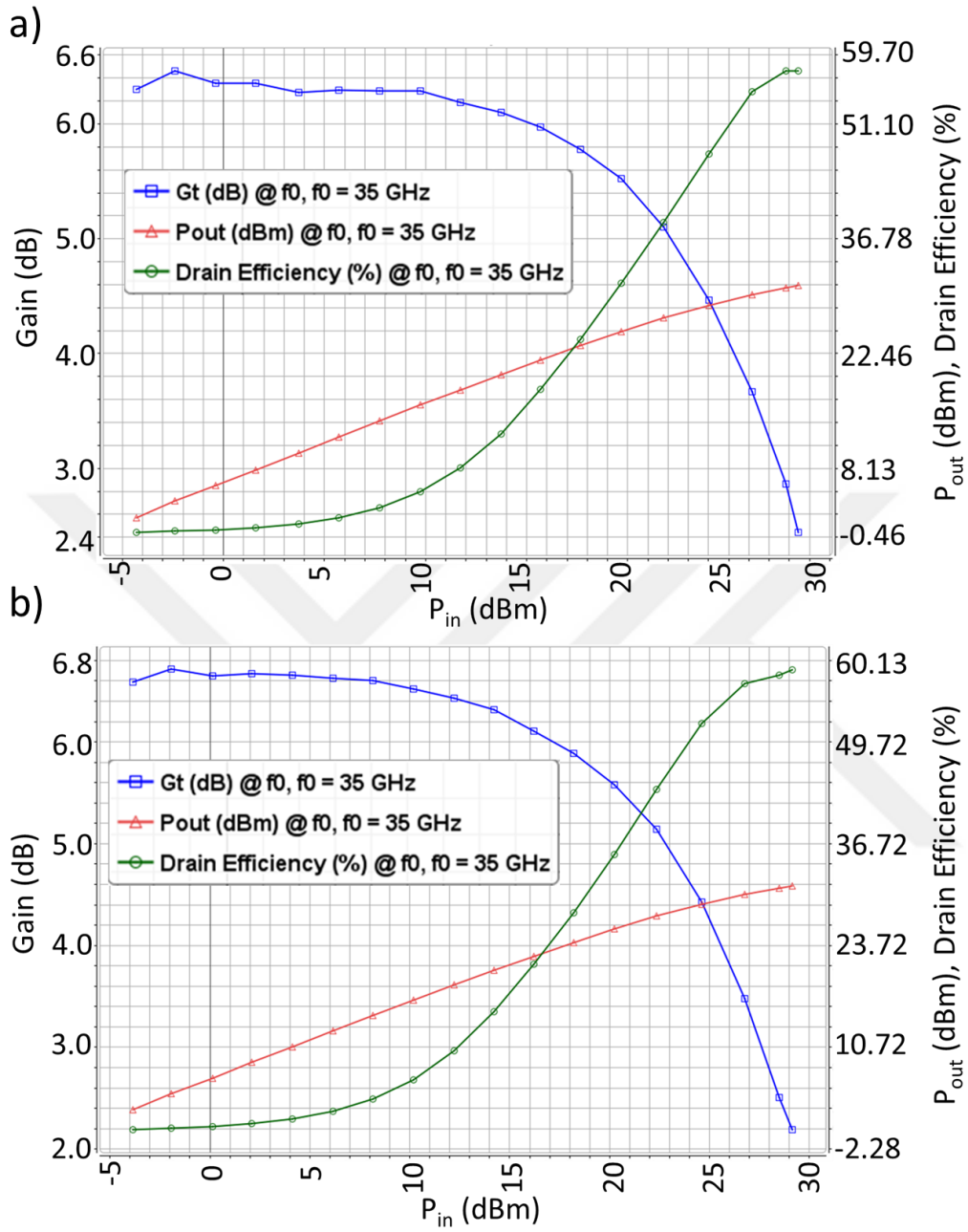


Figure 3.31. Power Performance of a) Non-Alloyed and b) Alloyed 6x75 μm HEMT with $L_g=0.15 \mu\text{m}$ and S-D Spacing is 2.5 μm at 35 GHz

Drain efficiency (η_D) is a measure of how much DC (P_{DC}) power is converted into microwave output power (P_{out}) is defined in Eq.3.10 [16];

$$\text{Drain Efficiency (DE)} = \frac{P_{\text{out}}}{P_{\text{DC}}} \quad (\text{Eq. 3.10})$$

Maximum Drain Efficiency of the fabricated HEMTs with alloyed ohmic contacts has almost 60% which is 3% higher compared to HEMT with alloyed ohmic contacts. At 3 dB compression, HEMT with non-alloyed and alloyed ohmic contacts have 31.42 dBm and 31.02 output power which corresponds to 3.07W/mm and 2.80 W/mm, respectively for the devices with 6x75 μm (0.45 mm) devices with an L_g of 0.15 μm . The improved power performance of the HEMTs with non-alloyed ohmic contacts can be attributed to the increase in I_{ds} , g_m , and reduced contact and on-resistances as tabulated in Table 3.6.

Simulations by Zhao [18] have shown that contact resistances and their temperature coefficients (R_s and R_d) have an impact on the large-signal performance of HEMTs. An experimental study performed by J.S. Moon [24], has shown that decreasing source access resistance significantly improves transistor DC performance which has a great influence on RF performance as well.

3.6 Results and Discussions

Varying Aluminum Thicknesses

Increasing Al thicknesses in metal stacks helped to improve contact resistance, R_c , which is crucial for device performance. But metal droplets were observed in source-drain spacing with increasing Al thicknesses which deteriorates device performance. In this work, clear source-drain spacing with an acceptable contact resistance of 0.51 Ω .mm was achieved with an Al thickness of 100nm.

Lower contact resistance could be also possible by increasing Al thickness within the metal stack without having metal droplets within source-drain spacing. Thermal stress within the metal stack could be decreased by dividing the total thickness of Al into two or more separate Al layers while keeping the total thickness is same. In this method, Ti metal could be used as a separation metal layer for successive Al layers.

Varying RTA Conditions

Different annealing conditions were investigated in order to have lower contact resistance. The contact resistance of 0.45 Ω .mm was achieved with a reasonable metal surface morphology and clear source-drain spacing at 850°C for 30 sec under nitrogen ambient. Increasing annealing temperature yielded deteriorated metal surface morphology that affects gate alignment steps in HEMT production.

Higher annealing temperature not only deteriorates metal surface morphology but also affects the epitaxial quality of the wafer. Researchers tend to have lower annealing temperatures with recess etching technology. This method enables a direct touch to 2DEG region and eliminates the necessity of high-temperature annealing.

Varying Barrier Metals

Ti, Mo and, Ni metals were used as an 'Barrier Metal' in order to prevent intermixing of Au with Al which results in high resistive 'purple plague'. In our study, we did not observe purple-plague in our metal alloys. The contact resistance of 0.41 Ω .mm was achieved with a reasonable metal surface morphology and clear source-drain spacing with Ni barrier metal. The metal stacks with Ti barrier metal yielded lower contact resistance of 0.31 Ω .mm with distorted edge acuity which is not acceptable. Distorted edges not only affected gate alignments but also cause the local variation of source-gate-drain distances which kills device performance.

Recently some other metals (Ta, W, and etc.) have been used within metal stacks. Melting points of these metals are higher compared to Ni and other barrier metals. This implies that special care should be given to the evaporation of these metals.

MOCVD Regrown InGaN Non-Alloyed Ohmic Contact

One of the unique parts of this work is developing MOCVD regrown InGaN non-alloyed ohmic contact for HEMT devices. In this work, degenerate doped In_{0.12}GaN layers were grown on sapphire substrate with doping of $7.4 \times 10^{19} \text{cm}^{-3}$. Silvaco simulations showed that n-doped In_{0.12}GaN layers had only 0.2eV SBH to GaN

HEMT which is much lower compared to Ti metal (~0.4 eV). Non-alloyed recessed ohmic contacts yielded 0.33 Ω .mm with an excellent metal surface morphology and edge acuity compared to alloyed metal contacts. To do the best of our knowledge, it is the first time MOCVD grown n-doped InGaN layers were used as a non-alloyed ohmic contacts to GaN HEMT device.

This process requires recess etching of epitaxial layers in order to direct contact to the 2DEG region. The plasma etching process should be also optimized in order to avoid any etch artifacts which result in higher contact resistance. Contact resistance improvement could be done by removing native oxide right before MOCVD growth.

HEMT Device Fabrication for Ka-Band Applications

Alloyed and non-alloyed ohmic contact technologies developed in this study were successfully implemented in order to fabricate HEMT devices for Ka-Band applications. GaN HEMT epitaxial structures were successfully grown on SI-SiC substrates with an N_b of $1.24 \times 10^{13} \text{ cm}^{-3}$, μ of $1877 \text{ cm}^2/\text{V.s}$, and sheet resistance (ρ) of $256 \text{ }\Omega/\text{sq}$ where Al content of about 28 %. $0.15 \text{ }\mu\text{m}$ gate length (L_g) technology was used in order to operate fabricated HEMT devices in Ka-band. Fabricated HEMT devices yielded contact resistances of 0.30Ω .mm and $0.43 \text{ }\Omega$.mm for MOCVD regrown InGaN non-alloyed ohmic contacts and alloyed ohmic contacts, respectively.

An improvement in both DC and RF performance was observed for the HEMT devices with MOCVD regrown InGaN non-alloyed ohmic contacts. Maximum I_{ds} current of 0.94 A/mm was achieved with a transconductance of 337 mS/mm (@6V) which were attributed to lower contact resistance of MOCVD regrown InGaN non-alloyed ohmic contacts. An improvement in small-signal measurements were also observed. For alloyed ohmic contacts, a cut of frequency (f_t) of 33.5 GHz and maximum oscillation frequency (f_{max}) of 67.5 GHz were obtained. For MOCVD regrown InGaN non-alloyed ohmic contacts, a cut of frequency (f_t) of 36.8 GHz and maximum oscillation frequency (f_{max}) of 75.0 GHz were obtained. Large-signal measurements showed that, at 3 dB compression, HEMT with MOCVD regrown

InGaN non-alloyed ohmic contacts had 31.42 dBm and 31.02 output power which corresponds to 3.07W/mm and 2.80 W/mm, respectively for the devices with 6x75 μm (0.45 mm) devices with an L_g of 0.15 μm . The improved power performance of the HEMTs with non-alloyed ohmic contacts can be attributed to the increase in I_{ds} , g_m , and reduced contact and on-resistances.

To further improve device performances not only ohmic contact resistance need to be reduced but also the epitaxial design of the HEMT structure needs to be improved. For higher frequencies, AlGaN barrier thickness should also be decreased by avoiding 'short channel effects' ($L_g/t_{bar} > 10$).

On the other hands, plasma etching conditions and post-plasma treatments should also be considered in detail. Native oxides is the main root cause of an increase in contact resistance and should be removed prior to MOCVD regrown InGaN layer.

3.7 References

- [1] N. Chaturvedi, 'Development and study of AlGa_N/Ga_N microwave transistors for high power operation', M.Sc. Thesis, TU Berlin, 2007
- [2] D.W. Johnson, 'SI-CMOS-LIKE INTEGRATION OF ALGAN/GAN DIELECTRIC-GATED HIGH-ELECTRON-MOBILITY TRANSISTORS', PhD Thesis, Texas A&M University, 2014
- [3] P.Leclaire, 'AlGa_N/Ga_N HEMTs with very thin buffer on Si (111) for nanosystems applications' *Semicond. Sci. Technol.* 29 (2014) 115018 (9pp)
- [4] R. Pecheux, 'Ga_N-based transistors using buffer-free heterostructures for next generation RF devices' 9th Wide Bandgap Semiconductors and Components Workshop
- [5] Ch. Zervos, 'AlN/Ga_N HEMTs with thin Ga_N/AlN buffer layers on sapphire (0001) substrates' WOCSDICE-2014
- [6] <https://swegan.se/technology.html>
- [7] A. P. Grzegorzcyk, Ga_N grown on sapphire by MOCVD- material for HEMT structures. Ph. D thesis, Radboud Universiteit Nijmegen, 2006
- [8] M. Rudzinski. Ph. D Thesis, Radboud Universiteit Nijmegen, 2006.
- [9] O. Breitschadel, 'Short-channel effects in AlGa_N/Ga_N HEMTs' *materials Science and Engineering B82* (2001) 238 – 240
- [10] D. Guerra, R. Akis, F. A. Marino, D. K. Ferry, S. M. Goodnick, and M. Saraniti, "Aspect Ratio Impact on RF and DC Performance of State-of-the-Art Short-Channel Ga_N and InGaAs HEMTs," *IEEE Electron Device Letters*, vol. 31, no. 11, pp. 1217-1219, Sep 2010.
- [11] G. H. Jessen *et al.*, "Short-Channel Effect Limitations on High-Frequency Operation of AlGa_N/Ga_N HEMTs for T-Gate Devices," *IEEE Transactions on Electron Devices*, vol. 54, no. 10, pp. 2589- 2597, Sep 2007.

- [12] D.H. Kim, “Design and Fabrication of AlGa_N/Ga_N on Si FETs for Ka Band MMICs”, PhD Thesis, Graduate School of Electrical and Computer Engineering Seoul National University, 2018
- [13] M. Leszczynski, T. Suski, J. Domagala, P. Prystawko in: Properties, processing and applications of gallium nitride and related semiconductors, INSPEC, London (1999).
- [14] B. Heying, X. H. Wu, S. Keller, Y. Li, D. Kapolnek, B. P. Keller, S. P. DenBaars, and J. S. Speck, Appl. Phys. Lett. 68, 643 1996.
- [15] H. Yu, ‘Growth of highly crystalline quality semi-insulating Ga_N layers for high electron mobility transistor application’ Journal of Applied Physics 100, 033501 (2006)
- [16] Hek de A. P. (2002). *Design, realisation and test of GaAs-based monolithic integrated X-band high-power amplifiers*. Eindhoven: Technische Universiteit Eindhoven. <https://doi.org/10.6100/IR556152>
- [17] R. S. Pengelly, Microwave field-effect transistors: Theory, design and applications. Research studies press, Letchworth, England, 1986, ISBN 0-86380-040-8.
- [18] X. Zhao, ‘Temperature-Dependent Access Resistances in Large-Signal Modeling of Millimeter-Wave AlGa_N/Ga_N HEMTs’ IEEE TRANSACTIONS ON MICROWAVE THEORY AND TECHNIQUES, digital Object Identifier 10.1109/TMTT.2017.2658561
- [19] S. Joglekar, Impact of recess etching and surface treatments on ohmic contacts regrown by molecular-beam epitaxy for AlGa_N/Ga_N high electron mobility transistors, APPLIED PHYSICS LETTERS 109, 041602 (2016)
- [20] S. Arulkumaran, Improved recess-ohmics in AlGa_N/Ga_N high-electron-mobility transistors with Al_N spacer layer on silicon substrate, P hys. Status Solidi C 7, No. 10, 2412–2414 (2010) / DOI 10.1002/pssc.200983860
- [21] W.S. Lau, Formation of Ohmic contacts in AlGa_N/Ga_N HEMT structures at 500 °C by Ohmic contact recess etching, Microelectronics Reliability 49 (2009) 558–561

- [22] Wen-Kai Wang, Low Damage, Cl₂-Based Gate Recess Etching for 0.3 μ m Gate-Length AlGa_N/Ga_N HEMT Fabrication, IEEE ELECTRON DEVICE LETTERS, VOL. 25, NO. 2, FEBRUARY 2004
- [23] Ching-Hui Chen, Cl₂ reactive ion etching for gate recessing of AlGa_N/Ga_N field-effect transistors, J. Vac. Sci. Technol. B 17.6., Nov/Dec 1999
- [24] J.S. Moon, '55% PAE and High Power Ka-Band Ga_N HEMTs With Linearized Transconductance via n⁺ Ga_N Source Contact Ledge' IEEE EDL, Vol. 29, No. 8, August 2008
- [25] <https://www.pveducation.org/pvcdrom/tlm-measurement>





CHAPTER 4

ALD GROWTH OF ALUMINUM DOPED ZINC OXIDE (AZO) AS A NON-ALLOYED RECESSED OHMIC CONTACT FOR GAN HEMT STRUCTURES

We aimed to develop an alternative way to produce non-alloyed ohmic contact to the MOCVD method for GaN-based HEMT devices. MOCVD re-growth technique requires high temperatures bringing a risk to already formed HEMT epitaxial layers and expensive to operate.

Entire AZO development processes were performed in the Thin Films and Coatings Laboratory at Middle East Technical University (METU). In this part, the process flow of AZO growth by ALD and characterization of AZO thin films along with the characterization on HEMT structures are covered.

4.1 ALD Growth of AZO Films

4.1.1 Initial ALD of AZO Trials

At first, AZO thin films with a fixed cycle ratio of 20:1 were deposited with atomic layer deposition (ALD) at 160 °C, 180 °C, and 200 °C on silicon and quartz substrates to investigate the effect of growth temperature on structural, optical, and electrical properties of the films. To study the effects of Al content on electrical and optical properties, ALD AZO thin films deposited on insulating and transparent quartz glass substrates. ALD AZO thin films deposited on Si wafers for investigating structural properties.

Pulse/purge time sequence for one ZnO cycle was DeZn (15 ms) / purge (10 s) / DI water (15 ms) / purge (10 s). To have a particular Al doping into ZnO, a single layer of Al₂O₃ was inserted after a set of ZnO sequences which is called ‘supercycle’ as seen in Figure 4.1., below. In this work, a supercycle composed of 20 cycles of ZnO

sequence and a single Al_2O_3 layer sequence with pulse/purge time of TMAI (15 ms) / purge (10 s) / DI water (15 ms) / purge (10 s).

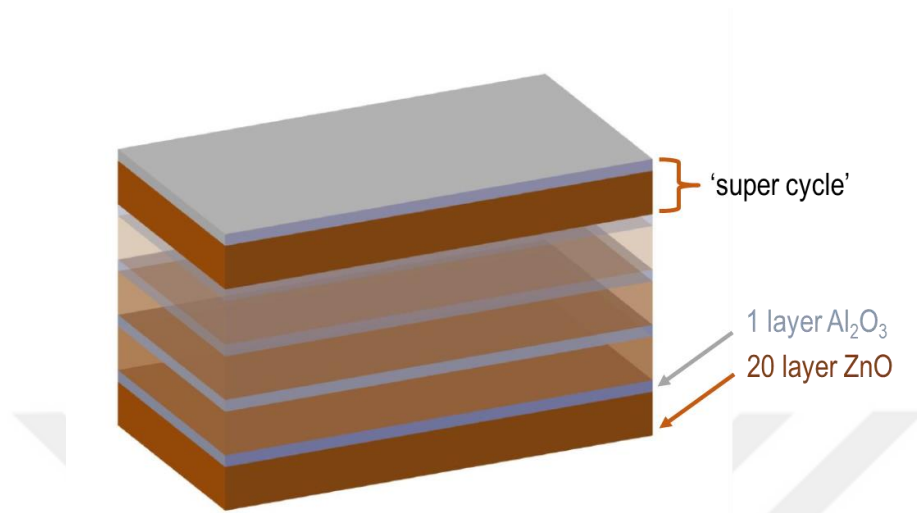


Figure 4.1 Cross-section view of the AZO thin films grown by thermal ALD on silicon and quartz substrates.

The atomic percentage of AZO thin films deposited on Si substrates determined by the XPS depth profile which is shown in Figure 4.2., below. Carbon was only detected on the surface due to possible contamination. The atomic percentage of Al was between 1.5 %- 4.0 % and did not show any systematic behavior at this temperature range. At around 80 nm depth (~12 min sputter time) Zn, O, and Al dropped to zero and the Si signal increased at a certain level which indicates AZO thin films were completely removed from the sputter region.

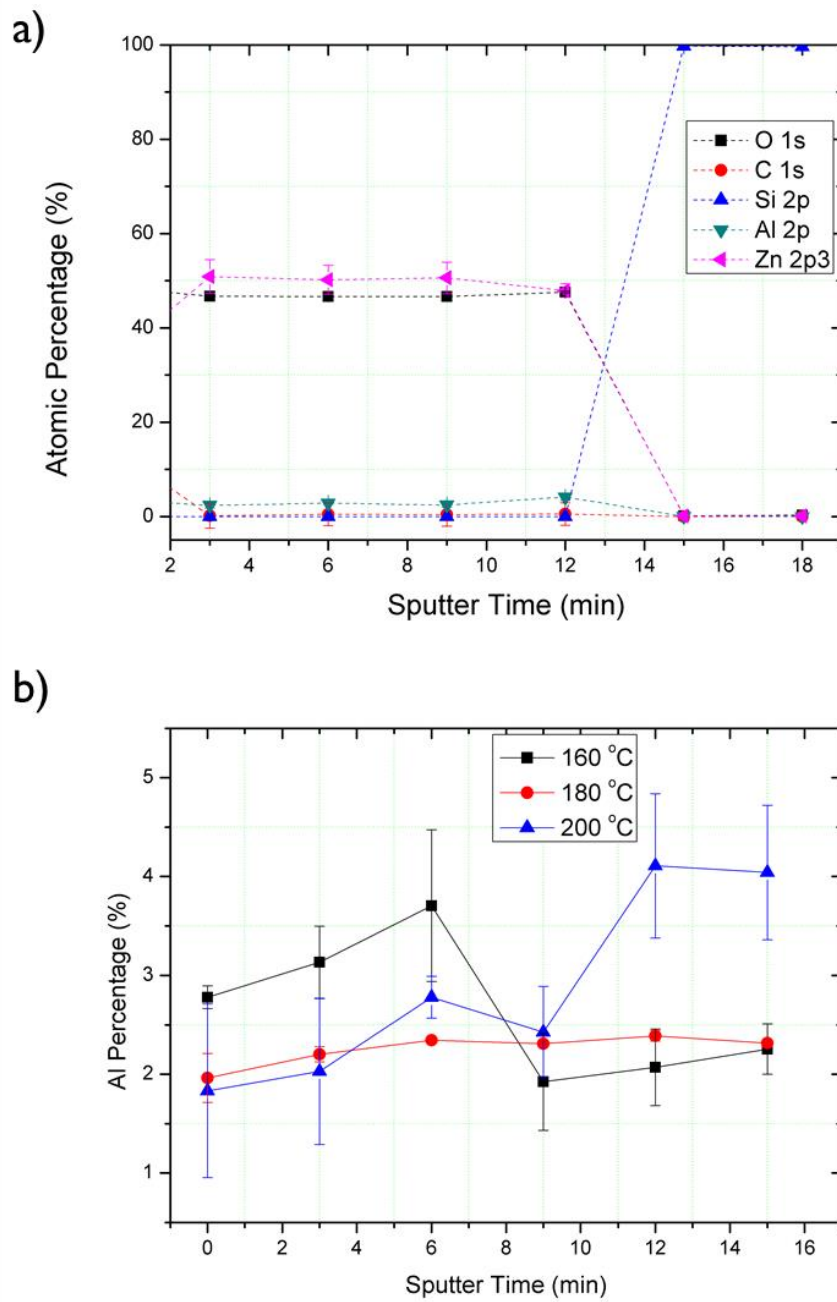


Figure 4.2 The atomic percentage of Zn, O, Al, C and Si elements, deposited at 200°C, as a function of depth from the surface as determined by depth-profiling XPS (left) and Al percentage of AZO thin films deposited at 160 °C, 180 °C, and 200 °C (right)

The surface morphology of the deposited AZO thin films on Si substrate was determined by AFM measurements. As seen in Figure 4.3., it shows that AZO thin film growth at lower temperatures has a smooth surface. This is because of the low mobility of add-atoms at lower deposition temperatures. At increasing temperatures, atoms tend to form more crystalline films, and the surface became rougher.

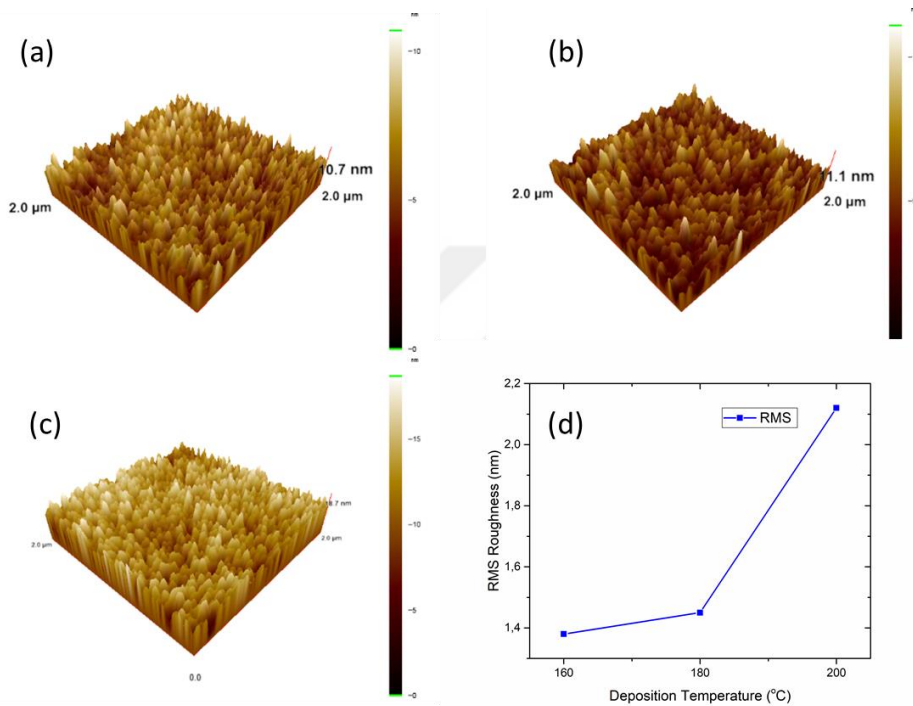


Figure 4.3 AFM micrograph for AZO thin films deposited at (a) 160 °C, (b) 180 °C and (c) 200 °C and (d) RMS values

An increase in E_g was observed in AZO thin films which are believed to be due to the Burstein-Moss Shift [1]. ZnO thin films have n-type conductivity [2] and the addition of Al^{3+} ions pushes the Fermi level into the conduction since all of the deposited AZO thin films exhibited a carrier concentration above $10^{20}cm^{-3}$ which is responsible for the increase in E_g . As seen in Figure 4.4., increasing deposition temperatures pushed E_g from ~3,35 eV to 3,47 eV which is an indication of increasing Al content in AZO films where the ideal bandgap of pure ZnO is 3.27 eV and Al_2O_3 is 8.7 eV.

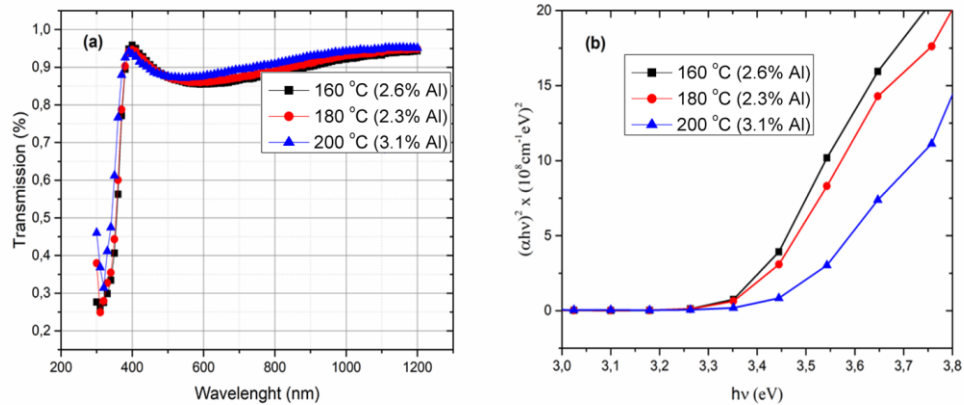


Figure 4.4 The transmission spectrum of AZO thin films (a) and Tauc Plot (b)

Electrical properties were investigated by Hall effect measurements. Figure 4.5 shows the electrical resistivity (ρ), electron mobility (μ_e), and carrier concentration (N_b) of AZO thin films deposited quartz glass substrates at 160 °C, 180 °C, and 200 °C which corresponds to Al compotion of 2.6%, 2.3%, and 3.1%, respectively.

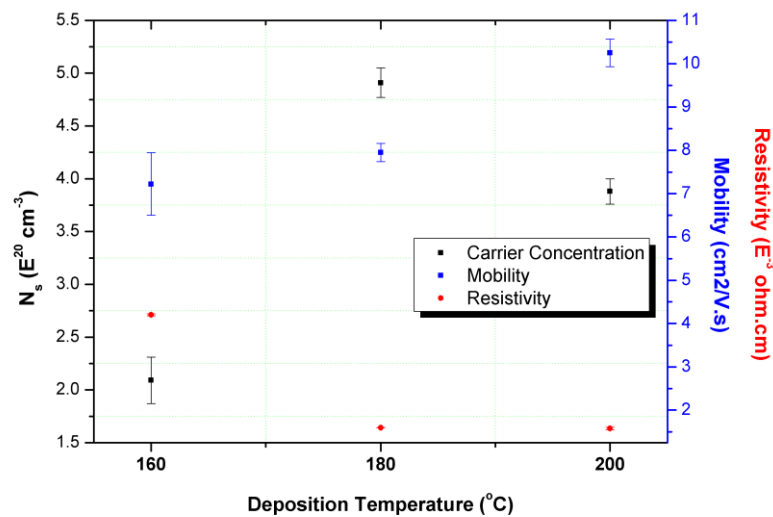


Figure 4.5 Room Temperature Hall Effect Measurement Results of AZO thin films; Carrier Concentration, Mobility and Resistivity with respect to deposition temperature.

It is known that the Al impurities can produce both ionized impurity centers and conduction electrons depending on deposition conditions. Increasing deposition temperature enhances Al diffusion into the ZnO layers and substitution of Al³⁺ into Zn²⁺ sites which results in charge donation and hence decreases resistivity [3-4].

It was observed that Al incorporation in AZO films was slightly increasing in a small range with increasing deposition temperatures which was attributed to change in individual growth per cycle (GPC) for ZnO and Al₂O₃ layers. It is known that GPC for ZnO layers is decreasing with deposition temperatures above 150°C where GPC remains almost the same for Al₂O₃ films deposited in between 160°C and 200°C. The change in GPC with varying deposition temperatures resulted in an increase in Al composition which gave rise to carrier concentration in AZO films. All AZO thin films exhibited high electron concentration above 10²⁰ cm⁻³ and increasing deposition temperature improved resistivity[11].

4.1.2 Optimization of AZO films for Non-Alloyed Ohmic Contacts

After examining the effect of temperature on electrical and optical properties, further fine optimization to AZO growth parameters were made to use in HEMT devices. For this purpose, AZO thin films with varying cycle ratios were deposited with ALD at 200 °C and 225 °C on silicon and quartz substrates to investigate the effect of cycle ratio on the optical and electrical properties of the films. We aimed to observe the deviation of electrical properties of AZO films with varying cycle ratio. The outcome of this study was implemented for AZO ohmic contacts to GaN HEMT devices.

Pulse/purge time sequence for one ZnO cycle was DeZn (15 ms) / purge (10 s) / DI water (15 ms) / purge (10 s). To have a particular Al doping into ZnO, a single layer of Al₂O₃ was inserted after a set of ZnO sequences which is called ‘supercycle’ as seen in Figure 4.6., below. In this work, a supercycle composed of x cycles of ZnO sequence and a single Al₂O₃ layer sequence with pulse/purge time of TMAI (15 ms) / purge (10 s) / DI water (15 ms) / purge (10 s).

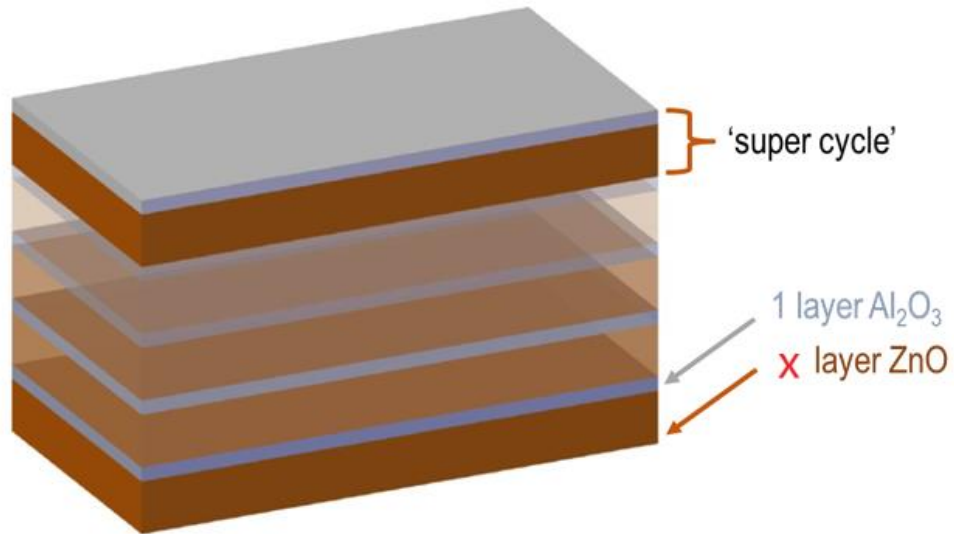


Figure 4.6. Cross-section view of the AZO thin films grown by thermal ALD on silicon and quartz substrates.

The thickness of the AZO films deposited on the Si substrate was determined by the stylus profilometer after the etching surface with diluted HF: DI (1:100) solution for 10sec. In this part, the thickness of the AZO films was fixed to ~100nm by considering previous growth parameters including growth temperature, growth rate, and cycle ratio. As seen in Figure 4.7., a surface profilometer (Dektak) was used in order to determine the thickness of AZO films deposited at 200°C.

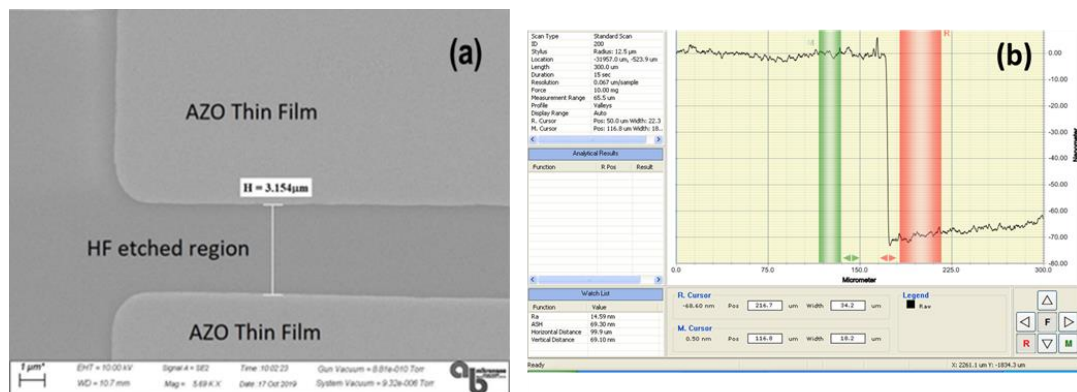


Figure 4.7. SEM (a) and Stylus Profilometer image (b) of AZO thin films deposited at 200 °C after wet etch with diluted HF: DI (1:100)

Details of the growth parameters and corresponding Al content contents are shown in Table 4.1. It is seen that increasing the ZnO cycle resulted in a decrease in Al content within AZO films as expected.

Table 4.1 Summary of the AZO films grown at 200 °C and 225 °C

ALD Deposition Temperature (°C)	Sample Code	ZnO/Al ₂ O ₃ Cycle	Al % (XPS)
200	16:1	16:1	4.15
	18:1	18:1	3.65
	21:1	21:1	3.1
	25:1	25:1	2.8
225	15:1	15:1	3.99
	20:1	20:1	2.66
	27:1	27:1	2.03
	30:1	30:1	1.88

XPS measurements of the AZO samples with different cycle ratios and growth temperature did not produce a significant difference in both Al percentage and E_g values.

As seen in Figure 4.8., increasing deposition temperatures pushed E_g from ~3.30 eV to 3.39 eV which is an indication of increasing Al concentration which was also confirmed by XPS measurements. Transmission measurement also showed all samples exhibited above 85% transmission in the infrared to UV region. It was seen that the degenerate doping in AZO films pushed band gap of ZnO films (~3.27eV) to higher levels of about 3.4 eV which is comparable with GaN (3.44eV).

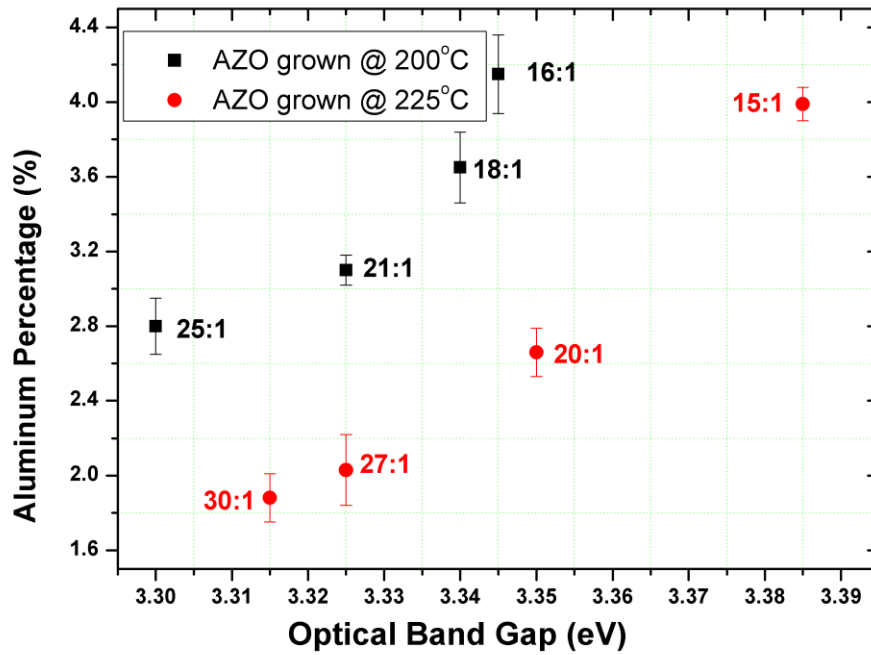


Figure 4.8 E_g of ALD grown AZO films with varying ZnO cycles grown at 200°C and 225°C

Electrical properties were investigated by Hall effect measurements. Figure 4.4. shows the electrical resistivity (ρ), electron mobility (μ_e), and carrier concentration (N_b) of AZO thin films deposited quartz glass substrates at 200 °C and 225 °C.

Hall effect measurements were in good agreement with bandgap values calculated from transmission measurements. It was seen that bandgap of the AZO materials grown in this work was precisely tuned with adjusting cycle ratios and growth temperatures.

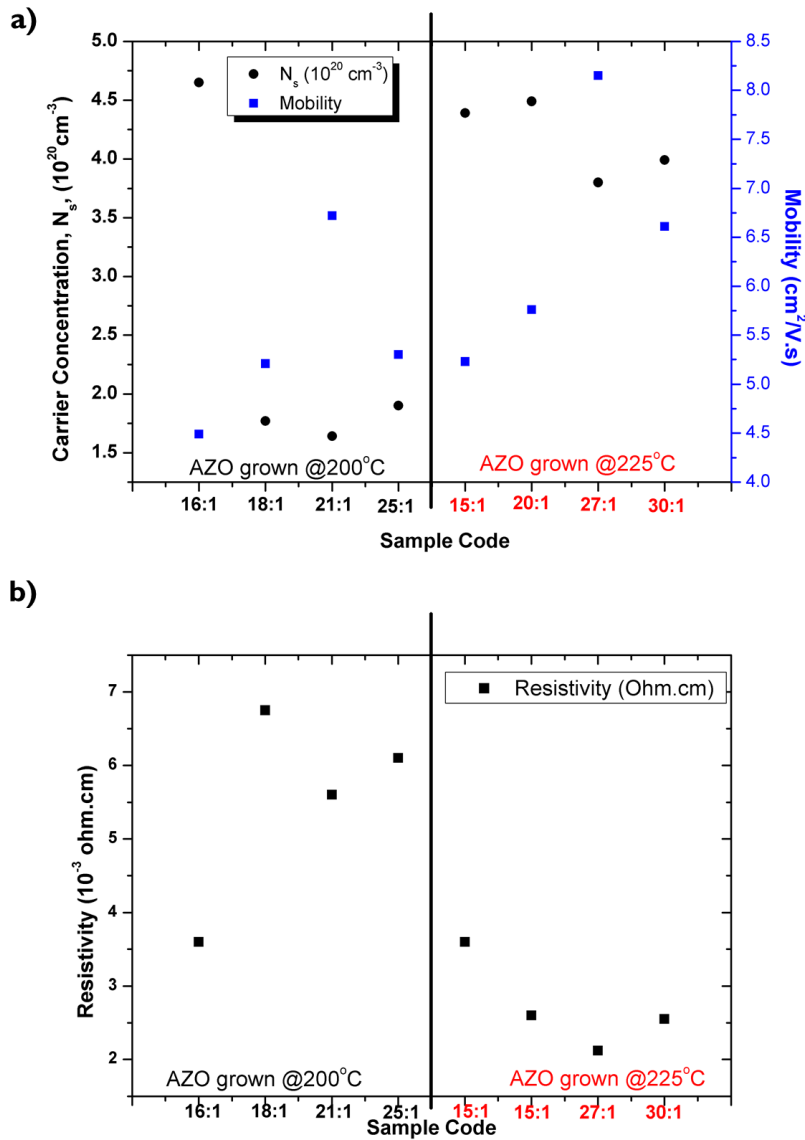


Figure 4.9 RT Hall Effect Measurement Result of AZO thin films a) Carrier Concentration and Mobility values and b) resistivity values

In the case of lower Al doping ($\text{ZnO}:\text{Al}_2\text{O}_3$ ratio $> 25:1$) Al^{3+} impurities are incorporated as interstitials or substitutional into ZnO matrix. Increasing Al doping by decreasing cycle ratio results in the formation of Al_2O_3 clusters which acts as carrier traps and increase resistivity.

It is also known that the Al impurities can produce both ionized impurity centers and conduction electrons depending on deposition conditions. Increasing deposition temperature enhances Al diffusion into the ZnO layers and substitution of Al³⁺ into Zn²⁺ sites which results in charge donation and hence decreases resistivity [3-4]. All AZO thin films exhibited high electron concentration above 10²⁰ cm⁻³ and increasing deposition temperature improved electron mobility.

In our study, AZO growth conditions were selected to have higher carrier concentration and lower resistivity which is comparable with MOCVD growth of In_{0.12}GaN layers. We aimed to utilize ALD grown AZO films as non-alloyed ohmic contacts in GaN-based HEMT devices designed for high-frequency applications.

4.2 Non-Alloyed Recessed AZO Ohmic Contacts in GaN HEMTs

Silvaco simulations were carried out in order to evaluate the band diagram of the AZO contact at the interface according to the characterization results of the AZO thin film grown at 200 °C.

Comparison of both material properties and bandgap diagram of re-grown In_{0.12}GaN and AZO films showing the possibility of the AZO films could be a promising candidate for non-alloyed ohmic contacts. Figure 4.10 showed that the Fermi level of both materials below the conduction band due to degenerate doping which pushes the Fermi level above the conduction band (Burstein-Moss Shift). In the case of AZO contact, there is no SBH is observed where the In_{0.12}GaN layer has 0.2eV barrier height.

Comparing with re-grown InGaN layers which require expensive equipment (i.e MOCVD) and elevated temperature ALD of AZO has several advantages. Conformal coating of AZO films for recessed ohmic contacts, lower process temperatures, simplified processes, and lower costs makes ALD of AZO a promising candidate for non-alloyed ohmic contacts.

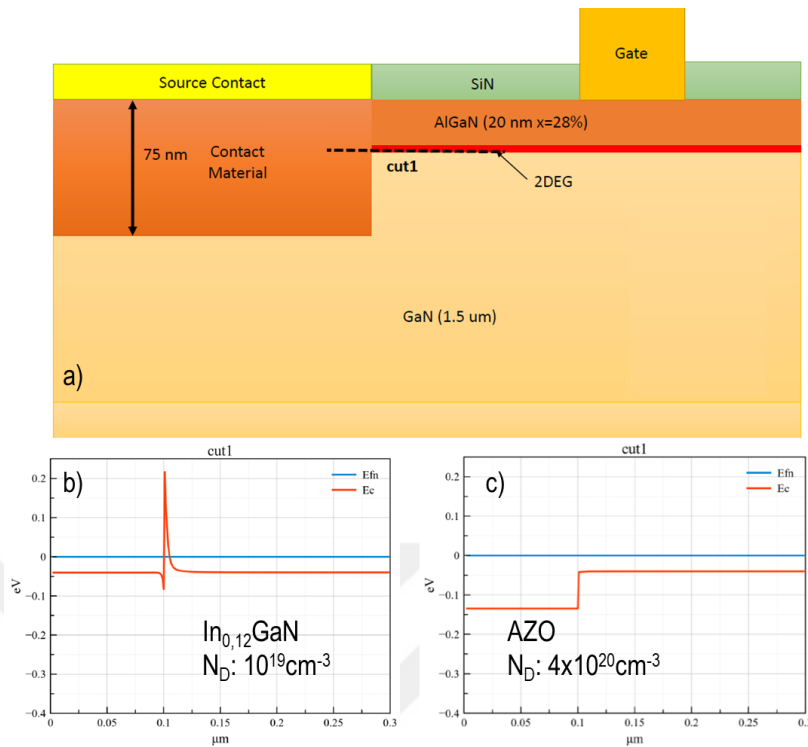


Figure 4.10 a) Cross Section of the device and b) Silvaco Simulations of $\text{In}_{0.12}\text{GaN}$ and c) AZO films

In this part, the same epitaxial structure with an electron concentration of $\sim 1.2 \times 10^{13} \text{ cm}^{-2}$, mobility of $1748 \text{ cm}^2/\text{V.s}$, and sheet resistance of $283 \text{ } \Omega/\text{sq}$ was used in order to have a better insight to the relation between alloyed, recessed alloyed, and recessed AZO ohmic contacts to AlGaIn/GaN HEMTs.

At first, HEMT on the Al_2O_3 substrate was diced into $15\text{mm} \times 15\text{mm}$ chips and TLM patterns were defined by ICP RIE using BCl_3/Cl_2 plasma on chips after standard cleaning processes via ACE/ISO. The recessed etch dept was around $\sim 90 \text{ nm}$ and SEM images were taken in order to confirm the etch depth and profile of the processed samples. In order to check the thickness of ALD of AZO films a control sapphire sample was co-loaded to the ALD chamber and thickness measurement was performed with the help of this control sample after partially etched by diluted HF (HF:DI & 1:100). Figure 4.11 shows both the recess depth of the sample and AZO film thickness acquired by the stylus profilometer.

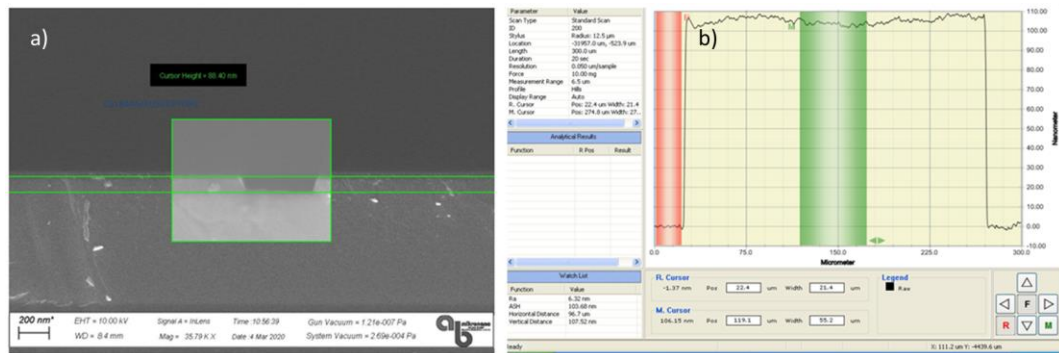


Figure 4.11 a) SEM Image of Recessed Samples with an etch depth of ~88nm and b) Thickness of ALD of AZO measured by Stylus profilometer

A control sample was also processed and alloyed ohmic contacts with Ti-20nm/Al-100 nm/Ni-40 nm/Au-50 nm metals were evaporated and followed by RTA performed at 850 °C/30 sec under N₂ ambient in order to monitor recess etch reliability. Processed samples were summarized in Table 4.2 and 4.3

Table 4.2 Summary of the Samples for AZO Ohmic Contact Study

Sample Code	Purpose
<p>Control Sample</p> <ul style="list-style-type: none"> - 90nm recessed - Oxygen Plasma Ashing @30W for 5min - Diluted HF Treatment for 1 min - Ti(20nm)/Al(100nm)/Ni(40nm)/Au(50nm) - RTA Treatment @850°C for 30sec under N₂ ambient 	<p>In order to control reliability of ICP RIE etch Process and Post Treatments</p>
<p>AZO Ohmic Contact</p> <ul style="list-style-type: none"> - 90nm recessed - Oxygen Plasma Ashing @30W for 5min - Diluted HF Treatment for 1 min - 100 nm ALD of AZO (<i>see Table 4.2 below</i>) - Pulse Times: TMAI: 15msec & DEZn:15msec - Cr(20nm)/Au(100nm) Evaporation - RTA Treatment @250°C for 30sec under N₂ ambient 	<p>6 different AZO growth condition was used to evaluate the AZO films as an non-alloyed ohmic contact</p>

ALD of AZO thin films deposited at 200 °C and 225 °C where the individual recipes were previously optimized. It is known that a small amount of Al (i.e. Zn: Al > 15:1) acts as substitutional or interstitial atoms in the ZnO matrix resulting in a decrease in resistivity. Increasing Al doping causes Al₂O₃ clusters which increase the resistivity of AZO films. Hall Effect measurements were performed for AZO films grown on sapphire substrates and revealed that the resistivity of AZO films was consistent with other reported values in the literature. TLM patterns were transferred to samples via wet etching (HF:DI & 1:100), optic lithography, and e-beam evaporation of Cr-Au metals (20 nm-100 nm). A stabilization bake was performed at 250 °C for 30 sec under N₂ ambient.

Table 4.3 Summary of the Deposition Details and Hall Measurement Results of AZO Samples for AZO Ohmic Contact Study

Sample Code	T_g ($^{\circ}\text{C}$)	ZnO : Al ₂ O ₃ Cycle Ratio	Total AZO Thickness (nm)	Hall Effect Measurement		
				N_s (cm ⁻³)	μ (cm ² /V.s)	ρ (W.cm)
17:1	200	17:1	100	1.46	5.27	8.29
26:1		26:1		1.45	6.78	6.34
35:1		35:1		0.58	2.78	3.81
15:1	225	15:1		2.26	6.09	4.52
18:1		18:1		2.14	8.84	3.30
25:1		25:1		2.29	8.47	3.20

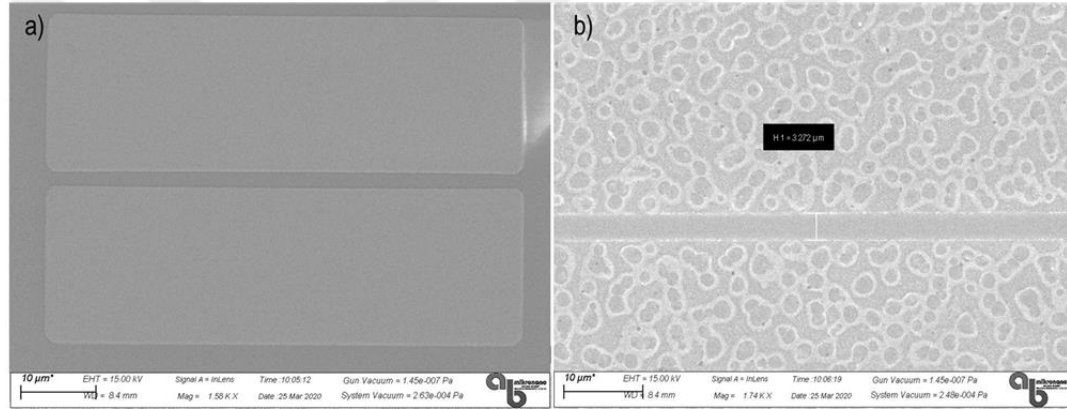


Figure 4.12 SEM Image of Recessed a) AZO and b) Alloyed Metal Ohmic Contacts

The surface morphology of the alloyed ohmic contacts and AZO ohmic contacts are shown in Figure 4.12. The surface morphology of the AZO contacts was much better compared to alloyed ohmic contacts which are important for next coming lithography processes and the line definition is clear which is crucial for transistor reliability.

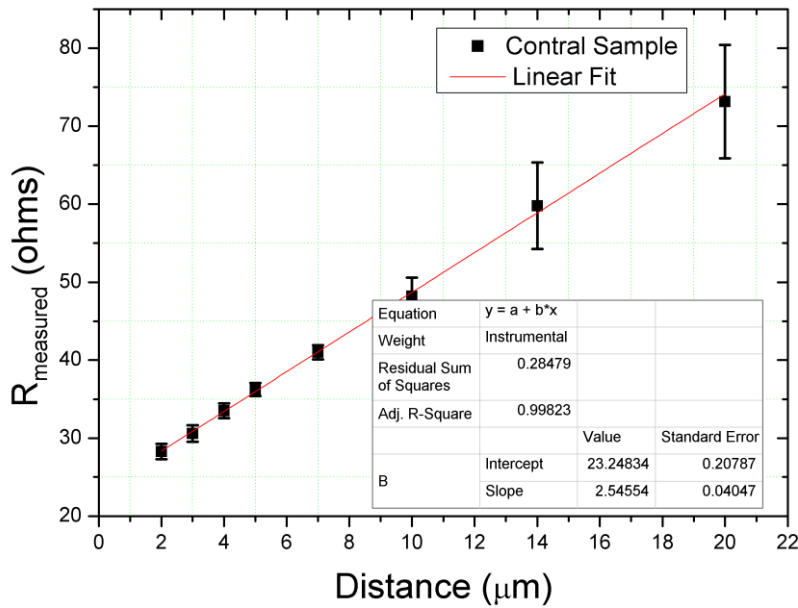


Figure 4.13 TLM Measurement of Recessed Ohmic Contacts – ‘Control Sample’

As seen in Figure 4.13., It was found that the contact resistance of the control sample was $2.34 \Omega \cdot \text{mm}$ which was much higher compared to non-recessed alloyed ohmic contacts. This deviation on contact resistance was attributed to both the ICP-RIE etching process and the not optimized post-treatments. It is well known that plasma etches processes introduce etch residue depending on the used chemistry [5-7]. It was considered that remaining to etch residue on the recessed ohmic region resulted in poor ohmic contact characteristics.

The measured contact resistance of the recessed AZO sample was so high and ohmic characteristics could not be achieved as seen in Figure 4.14. The contacts exhibited Schottky characteristics instead of ohmic characteristics. This was attributed to the much lower process temperature compared to the ‘Control Sample’ which has a contact resistance of $2.34 \Omega \cdot \text{mm}$ and plasma etch damages. In the case of higher RTA treatment for ‘Control Sample’ help to recover etch based damages [8-9].

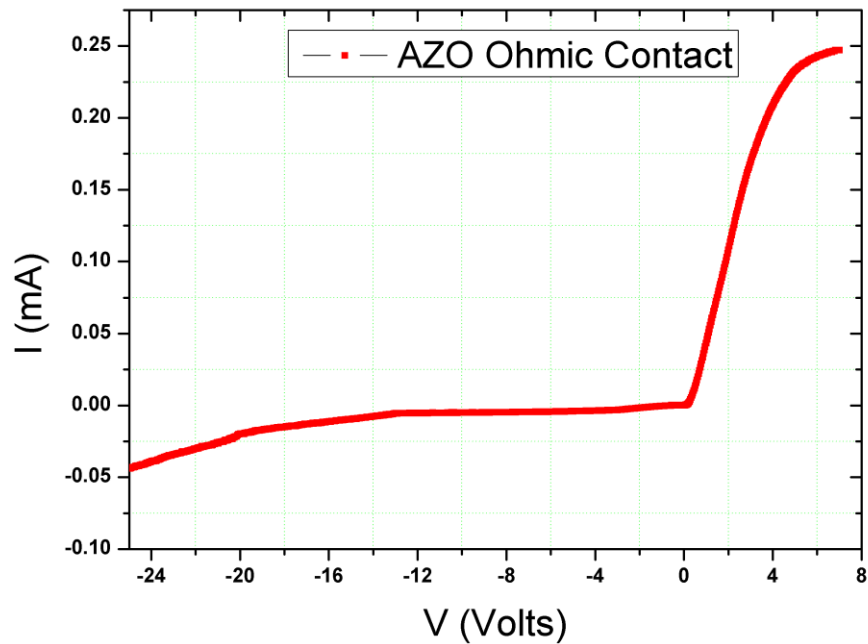


Figure 4.14 Measurement of AZO Ohmic Contacts to GaN HEMT

4.2.1 Side-Wall Issues

SEM images of the etched region prior to AZO deposition is seen in Figure 4.15, below. It is seen that the angle of the side-wall of the etched region was about 65° , which was well below 90° , which means that 2DEG that is created in the GaN buffer layer may be weakened since the AlGaN barrier layer above the said region is partially removed and the thickness of the barrier is not enough to induce electron gas in the region. This could be another drawback in order to have acceptable contact resistance.

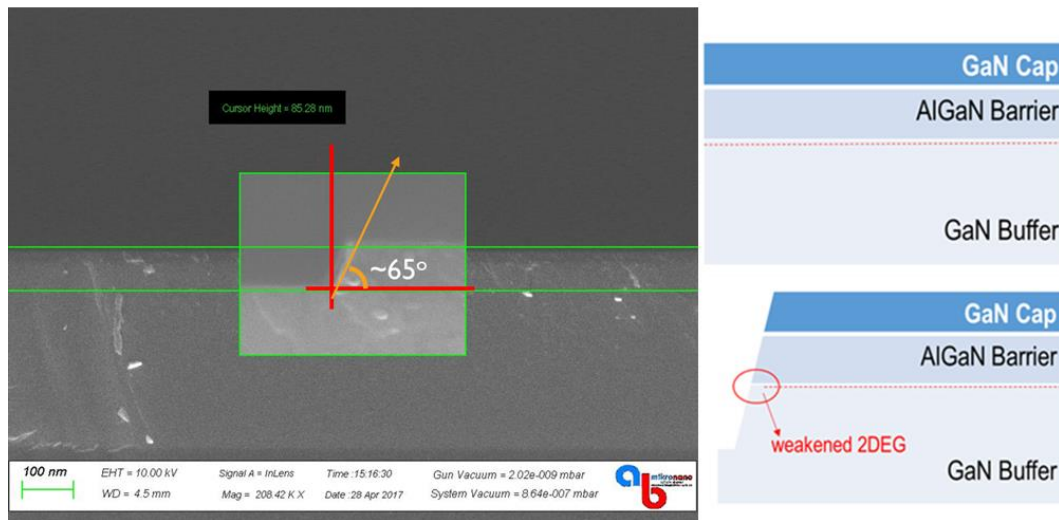


Figure 4.15 a) SEM Image of Recessed Samples with an etch depth of $\sim 88\text{nm}$ and b) Thickness of ALD of AZO measured by Stylus profilometer

It is considered that the origin of the non-vertical side-wall problem was the thickness of the photomask (PR). It is well known that the thickness of the PR mask should be thinner for recess etching. In plasma etching processes both physical and chemical etching takes place and by-products need to be evacuated in a certain time. Increasing PR thickness increase the evacuation time of etching species within the mask opening region and promotes chemical etching which is isotropic. The thickness of the PR mask was about $1.5\mu\text{m}$ for our recess etching processes. Isotropic etch was promoted at the bottom of the mask opening which resulted in an inclined side-wall with $\sim 65^\circ$ as seen in Figure 15.

Figure 16 shows the schematics of a PR mask with two different thicknesses. For recess etching, it is important to use special photoresists, dielectrics or metal masks.

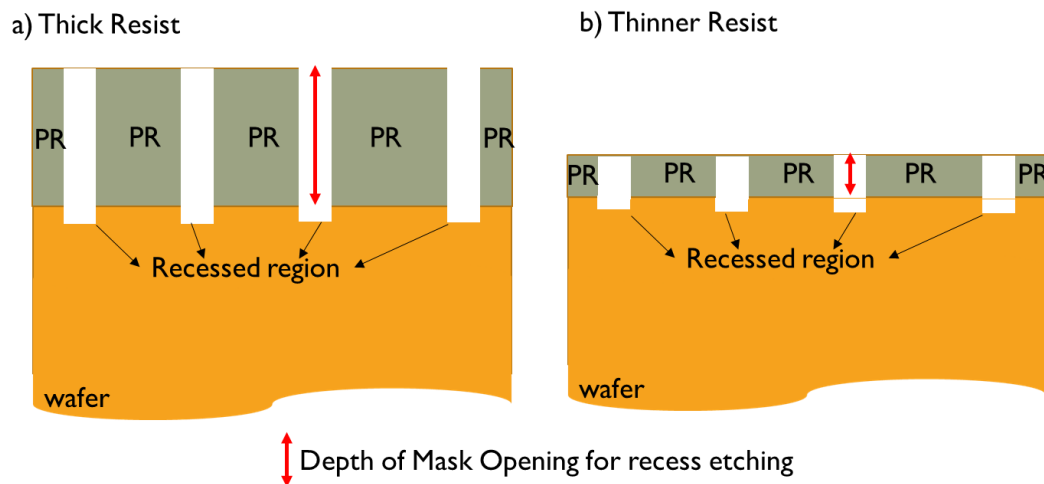


Figure 4.16 Schematics of Photomask (PR) for recess etching of HEMT wafer a) Thick resist b) thinner resist

4.2.2 Effect of Post-Plasma Conditions

In GaN HEMT microfabrication Cl-based plasma is used to etch the desired region. Plasma etchs residues and artifacts are removed by plasma or wet etch processes depending on process needs.

In this work, ICP RIE etching was performed by using $\text{SF}_6 + \text{Ar}$ plasma followed by post-treatment including diluted HF cleaning of the etched regions. HF treatment could potentially induce a defect in GaN materials. Fluorine based plasma cleaning provokes shallow traps in recessed ohmic region and prevent electron flowing over the region [16].

A high concentration of fluorine ions may diffuse into the material and trap the 2DEG electrons which are responsible for ohmic contacts. This may cause a depletion in 2DEG electrons and results in an increase in ohmic contact resistance [10][14][15].

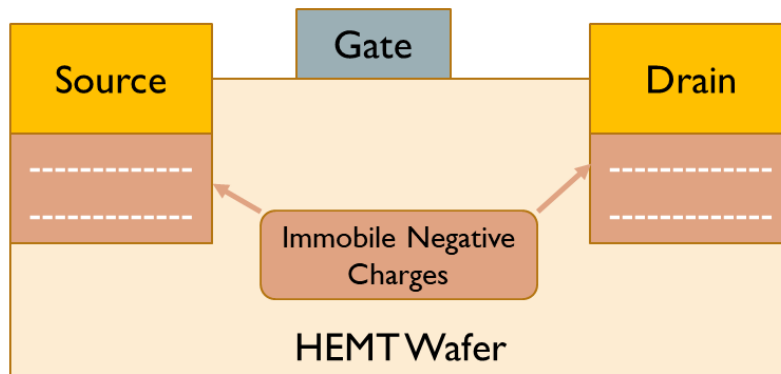


Figure 4.17 Schematic illustration of immobile negative charges under source and drain contacts

4.3 Results and Discussions

Optimization of ALD of AZO growths

In this part, various growth conditions were used in order to investigate the material properties of AZO films. Increasing deposition temperatures resulted in lower GPCs for ZnO layers and corresponding Al contents were increased for AZO films. Substitution of Al^{3+} into Zn^{2+} sites promoted by increasing Al content in AZO films which results in charge donation and increase the carrier concentration. An increase in E_g was attributed to the doping level and be explained by the filling of the lowest levels of the available states in the conduction band.

Varying $\text{ZnO}:\text{Al}_2\text{O}_3$ cycle ratio also at a fixed deposition temperature also affected bandgap of the AZO films. In this case, Al composition of the growing films were modulated by cycle ratio. Increasing $\text{ZnO}:\text{Al}_2\text{O}_3$ ratio resulted in lower Al content in AZO films as expected. For a given deposition temperature, the relationship between $\text{ZnO}:\text{Al}_2\text{O}_3$ ratio and Al content in AZO films was almost linear and inversely proportional as indicated in Table 4.1. It was seen that a two-fold increase in $\text{ZnO}:\text{Al}_2\text{O}_3$ ratio resulted in a a two-fold decrease in Al content in AZO film.

Fine-tune of bandgap values of AZO films within the range 3.30 eV and 3.40 eV was successfully demonstrated by optimizing both deposition temperatures and cycle ratio of growth conditions.

Initial trials showed that AZO films were degenerated doped and film resistivities were in $10^{-3} \Omega\cdot\text{cm}$, the same order in lowest reported values by R.M. Mundle et al [11],[12]. We observed that increasing deposition temperatures caused a slight increase in mobility which was attributed to improved crystal quality compared to AZO films grown on lower deposition temperatures. Electrical and optical characterization of AZO films exhibited similar properties with MOCVD regrown InGaN films.

ALD grown AZO films as Non-Alloyed Ohmic Contact for Gan HEMT

Silvaco simulations revealed that AZO films could be replaced with MOCVD regrown InGaN layer.

Optimized AZO films were implemented in non-alloyed ohmic contact study. Initial trials did not yield expected results and contacts exhibited Schotkky characteristic instead of the ohmic characteristic as seen in Figure 4.14. This was attributed to non-proper etching of side-wall and fluore effect from SF₆ based ICP plasma etching and/or HF based post-etch cleaning processes.

4.4 References

- [1] C.H. Zhai, Effects of Al Doping on the Properties of ZnO Thin Films Deposited by Atomic Layer Deposition, Zhai et al. *Nanoscale Research Letters* (2016) 11:407
- [2] M.Godlewski, ZnO layers grown by Atomic Layer Deposition: A new material for transparent conductive oxide, *Thin Solid Films* 518 (2009) 1145–1148
- [3] A. V. Sing, Doping mechanism in aluminum doped zinc oxide films, *Journal of Applied Physics* 95, 3640 (2004)
- [4] D. S. Y. Jayathilake, Microwave-Assisted Synthesis and Processing of Al-Doped, GaDoped, and Al, Ga Codoped ZnO for the Pursuit of Optimal Conductivity for Transparent Conducting Film Fabrication, *ACS Sustainable Chem. Eng.* 2017, 5, 4820–4829
- [5] R. Sokolovskij, Precision recess of AlGaN/GaN with controllable etching rate using ICP-RIE oxidation and wet etching, *Procedia Engineering* 168 (2016) 1094 – 1097
- [6] S.J. Pearton, A Review of Dry Etching of GaN and Related Materials, *MRS Internet J. Nitride Semicond. Res.* 5, 11 (2000)
- [7] C.Y. Lee, Plasma-Induced Damage and Recovery on Au/n-GaN Schottky Diode in Different Processes, *Japanese Journal of Applied Physics* 51 (2012) 076503
- [8] Q. Fan, Reactive ion etch damage on GaN and its recovery, *J. Vac. Sci. Technol. B* 24,3..., May/June 2006
- [9] H. W. Choi, Plasma-induced damage to n-type GaN, *APPLIED PHYSICS LETTERS VOLUME 77, NUMBER 12 18 SEPTEMBER 2000*
- [10] Y.He et al., 2016. *SSLChina: IFWS*. DOI: 10.1109/IFWS.2016.7803772
- [11] R. M. Mundle, Electrical conductivity and photoresistance of atomic layer deposited Al-doped ZnO films, *J. Vac. Sci. Technol. A* 31(1), Jan/Feb 2013, DOI 10.1116/1.4772665
- [12] B.Sing, Highly conducting zinc oxide thin films achieved without postgrowth Annealing, *APPLIED PHYSICS LETTERS* 97, 241903 _2010, DOI: 10.1063/1.3525575
- [13] H.Huang, Au-Free Normally-Off AlGaN/GaN-on-Si MIS-HEMTs Using Combined Partially Recessed and Fluorinated Trap-Charge Gate Structures, *IEEE ED*, DOI: 10.1109/LED.2014.2310851

- [14] K. Han et al., Employing hole-array recess of barrier layer of AlGa_N/Ga_N Heterostructures to reduce annealing Temperature of Ohmic contact, Semicond. Sci. Technol. 32 105010
- [15] K. Y. Osipov et al., Fabrication technology of Ga_N/AlGa_N HEMT slanted sidewall gates using thermally reflowed ZEP resist and CHF₃/SF₆ plasma etching, CS MANTECH Conference, May 13th - 16th, 2013, New Orleans, Louisiana, USA
- [16] R. Cuerdo et al., The Kink Effect at Cryogenic Temperatures in Deep Submicron AlGa_N/Ga_N HEMTs, IEEE ELECTRON DEVICE LETTERS, VOL. 30, NO. 3, MARCH 2009





CHAPTER 5

CONCLUSION AND FUTURE PLAN

5.1 Conclusions

The objective of this work focused on the ohmic contact process technologies of GaN-based High Electron Mobility Transistors (HEMT) for K_a-band applications. The goal of this work was to develop an ohmic contact technology that does not require annealing of its metal pads. So that resulting ohmic contacts should have the following features;

- The improved surface roughness of the ohmic contacts for the next processing steps
- Improved line definition and removed metal spread for small S-D spacing HEMTs
- Reduced contact resistance for improved RF device performance.

Initially, we optimized both alloyed and MOCVD regrown InGaN non-alloyed ohmic contacts on HEMT on sapphire substrates and achieved;

- alloyed ohmic contact with 0.51 Ω .mm for the ‘Sample Al-100’
- alloyed ohmic contact with 0.45 Ω .mm for the ‘Sample RTA 850°C/30sec’
- alloyed ohmic contact with 0.41 Ω .mm for the ‘Sample Ni Barrier’.
- non-alloyed ohmic contact with 0.33 Ω .mm for the ‘MOCVD regrown InGaN non-alloyed sample’
- excellent metal surface morphology, clear metal edges and clear source-drain spacing for the ‘MOCVD regrown InGaN non-alloyed sample’

In this thesis first time experimented and obtained results:

- MOCVD regrown InGaN layers were utilized as non-alloyed ohmic contacts for GaN-based HEMT devices
- Ohmic contact resistance of $0.33\Omega\cdot\text{mm}$ was obtained with MOCVD regrown InGaN layers for GaN-based HEMT devices for Ka-Band applications
- ALD grown AZO films were utilized for the first time as non-alloyed ohmic contacts for GaN-based HEMT devices

For alloyed ohmic contact ‘Sample Ni-Barrier’ technology was selected for HEMT device processing.

In Chapter 3.3, GaN-based HEMT structures grown on 3” SI 4H-SiC substrates and $0.15\ \mu\text{m}$ gate length and W_g of $75\ \mu\text{m}$ technologies were utilized to fabricate HEMT device for Ka-band applications. HEMT on SI-SiC devices with alloyed ohmic contacts exhibited a contact resistance of $0.43\ \Omega\cdot\text{mm}$ whereas HEMT on SI-SiC devices with non-alloyed MOCVD grown InGaN ohmic contacts exhibited a contact resistance of $0.30\ \Omega\cdot\text{mm}$ with an excellent surface morphology and edge acuity. It is well known that the deviation in S-D spacing results in detrimental effects for HEMT [1-4].

In Chapter 3.4, the DC performance of the fabricated devices with alloyed and non-alloyed ohmic contacts showed a current density, I_{ds} , of $0.94\ \text{A}/\text{mm}$ and $0.88\ \text{A}/\text{mm}$, respectively. The transconductance, g_m , of the fabricated devices with alloyed and non-alloyed ohmic is $337\ \text{mS}/\text{mm}$ and $314\ \text{mS}/\text{mm}$, respectively.

Measured f_t/f_{max} was for alloyed and MOCVD regrown InGaN non-alloyed ohmic contacts were $33.5\ \text{GHz}/67.5\ \text{GHz}$ and $36.8\ \text{GHz}/75.0\ \text{GHz}$, respectively. The maximum available gain at $37\ \text{GHz}$ obtained for alloyed and MOCVD regrown InGaN non-alloyed ohmic contacts was $5.2\ \text{dB}$ and $6.4\ \text{dB}$, respectively. To do the best of our knowledge, MOCVD regrown InGaN non-alloyed ohmic contact technology was used by our group.

At 3dB compression, HEMT devices with MOCVD regrown InGaN non-alloyed ohmic contacts and alloyed ohmic contacts exhibited an output power of 31.42 dBm and 31.02 dBm which corresponds to 3.07 W/mm and 2.80 W/mm, respectively for the devices with $6 \times 75 \mu\text{m}$ (0.45 mm) devices with an L_g of $0.15 \mu\text{m}$.

In Chapter 4, aluminum-doped zinc oxide (AZO) films grown by Atomic Layer Deposition (ALD) were demonstrated, and thin-film characterization was performed. Band gap of AZO films were in the range of 3.3 eV to 3.4 eV and carrier concentration was above 10^{20}cm^{-3} which is comparable with MOCVD growth of InGaN layer. Material properties (carrier concentration, mobility and etc.) of AZO thin films exhibited a potential for non-alloyed ohmic contacts for AlGaN/GaN HEMTs which is supported by the Silvaco simulations in Chapter 4.1.3. Initial attempts for having AZO ohmic contacts for AlGaN/GaN HEMTs were not successful due to non-optimized process conditions including recess etching and post-treatments.

5.2 Future Plan

In this research, MOCVD growth of AlGaN/GaN HEMT on 4H SI-SiC for Ka-band applications and devices technologies focusing on the method of making alloyed and non-alloyed ohmic contacts were described. However, there are some important issues still remaining to be solved. The following action list includes some research topics for future works;

- Fine tune of epitaxial design (Al composition in barrier, barrier thickness, back barriers and etc.)
- More accurate simulations dedicated to the Ka-band epi structure and device geometry should be carried out in order to improve transistor performance.
- Optimization of etching processes for having vertical side-wall. For recess etching of the source and drain contact region it is important to

have vertical side-walls in order not to deplete electrons in 2DEG as seen in Figure 4.13. It is important to use a thin mask for recess etching which helps to have a vertical side-wall profile. This could be accomplished by using proper resist or metal mask as well.

- Fluor-free plasma etch should be selected to avoid unintentional fluorine doping in GaN materials
- Fluor-free post etch treatment. Post-etch treatment is also very important and should be performed prior to AZO growth and treated samples should be loaded to the ALD chamber avoiding the formation of native oxides (i.e Ga₂O₃ or Al₂O₃) between 2DEG and AZO films. 2DEG electrons and results in an increase in ohmic contact resistance [10][11]

Detail of the ALD of AZO work for future studies is shown in Table 5.1 below.

Table 5.1 Optimization of ALD of AZO ohmic contacts processes prior to HEMT device fabrication

Sample	Fotomask	Dry Etching (90° side-wall profile)	Post Treatment	ALD of AZO Growth Condition
AlGaIn/GaN	Photoresist	Recipe_1	Asher + HCl	T _g : 225°C
		Recipe_2		
HEMT	Metal Mask	Recipe_1	<i>Note: HCl should be applied prior to ALD Deposition</i>	Cycle Ratio: 22
		Recipe_2		Super Cycle: 20

5.3 References

- [1] C.H. Zhai, Effects of Al Doping on the Properties of ZnO Thin Films Deposited by Atomic Layer Deposition, Zhai et al. *Nanoscale Research Letters* (2016) 11:407
- [2] M.Godlewski, ZnO layers grown by Atomic Layer Deposition: A new material for transparent conductive oxide, *Thin Solid Films* 518 (2009) 1145–1148
- [3] A. V. Sing, Doping mechanism in aluminum doped zinc oxide films, *Journal of Applied Physics* 95, 3640 (2004)
- [4] D. S. Y. Jayathilake, Microwave-Assisted Synthesis and Processing of Al-Doped, GaDoped, and Al, Ga Codoped ZnO for the Pursuit of Optimal Conductivity for Transparent Conducting Film Fabrication, *ACS Sustainable Chem. Eng.* 2017, 5, 4820–4829
- [5] R. Sokolovskij, Precision recess of AlGaN/GaN with controllable etching rate using ICP-RIE oxidation and wet etching, *Procedia Engineering* 168 (2016) 1094 – 1097
- [6] S.J. Pearton, A Review of Dry Etching of GaN and Related Materials, *MRS Internet J. Nitride Semicond. Res.* 5, 11 (2000)
- [7] C.Y. Lee, Plasma-Induced Damage and Recovery on Au/n-GaN Schottky Diode in Different Processes, *Japanese Journal of Applied Physics* 51 (2012) 076503
- [8] Q. Fan, Reactive ion etch damage on GaN and its recovery, *J. Vac. Sci. Technol. B* 24,,3..., May/June 2006
- [9] H. W. Choi, Plasma-induced damage to n-type GaN, *APPLIED PHYSICS LETTERS VOLUME 77, NUMBER 12 18 SEPTEMBER 2000*
- [10] H.Huang, Au-Free Normally-Off AlGaN/GaN-on-Si MIS-HEMTs Using Combined Partially Recessed and Fluorinated Trap-Charge Gate Structures, *IEEE ED*, **DOI:** 10.1109/LED.2014.2310851
- [11] K. Han, Employing hole-array recess of barrier layer of AlGaN/GaN Heterostructures to reduce annealing Temperature of Ohmic contact, *Semicond. Sci. Technol.* 32 105010

CURRICULUM VITAE

PERSONAL INFORMATION

Surname, Name: Çakmak, Hüseyin

Nationality: Turkish (TC)

Date and Place of Birth: 10 September 1981, Hekimhan

Marital Status: Married

Cell: +90 532 610 78 32

Fax: +90 312 290 35 50

E-mail: e122704@gmail.com

LinkedIn: <https://www.linkedin.com/in/h%C3%BCseyin-%C3%A7akmak-phd-candidate-bb3b2354/>

EDUCATION

Degree	Institution	Year of Graduation
MS	METU Micro&Nano Tech. Department	2013
BS	METU Physics Department	2005
High School	Cumhuriyet High School Science Branch, Tarsus	2000

WORK EXPERIENCE

Year	Place	Enrollment
2019-present	Aselsan & Bilkent Micro & Nano Co. 	Senior Epitaxy Specialist / Team Lead.
2018-2019	GUNAM / METU	Senior R&D Specialist/Team Lead.
2015-2018	Anatek	Sales&Application Manager
2006-2015	Nanotechnology Research Center (NANOTAM) / Bilkent University	Senior Process Engineer/Epitaxy

FOREIGN LANGUAGES

English (Advanced)

PUBLICATIONS

A. Thesis

1. H. Çakmak, M.Sc. Thesis, 2012.

Growth and Characterization of Indium Rich Indium-Gallium-Nitride Solar Cell Epitaxial Structures by Metal Organiz Chemical Vapor Deposition

B. Journal Articles

1. H.Çakmak, M.Ozturk, E.Ozbay and B. İmer, Non-Alloyed Ohmic Contacts in AlGa_N/Ga_N HEMTs with MOCVD Regrowth of InGa_N for Ka-Band Applications, DOI (identifier) 10.1109/TED.2021.3050740, IEEE -TED

2.H. Çakmak, Engin Arslan, M. Rudzinski, P. Demirel, H.E. Ünalın, W. Strupinski, R. Turan, M. Öztürk, E. Özbay ‘In rich InGa_N solar cells grown by MOCVD’ J Mater Sci: Mater Electron, DOI 10.1007/s10854-014-2070-4 (2014)

3.Beyza Sarıkavak-Lişesivdin, Sefer Bora Lişesivdin, Naci Balkan, Gökhan Atmaca, Polat Narin, Hüseyin Çakmak, Ekmel Özbay ‘Energy Relaxation of Electrons in InGa_N Quantum Wells’ Metallurgical and Materials Transactions A, DOI 10.1007/s11661-015-2762-2 (2015)

4.E. Arslan, M.K. Öztürk H. Çakmak, P. Demirel, S. Özçelik, E. Özbay ‘Evolution of the mosaic structure in InGa_N layer grown on a thick Ga_N template and sapphire substrate’, J Mater Sci: Mater Electron (2013) 24:4471–4481, DOI 10.1007/s10854-013-1427-4

5.E. Arslan, H. Çakmak, E. Özbay ‘Forward tunneling current in Pt/p-InGa_N and Pt/n-InGa_N Schottky barriers in a wide temperature range’ Microelectronic Engineering 100 (2012) 51–56

6.Hongbo Yu, Sefer B. Lisesivdin, Basar Bolukbas, Ozgur Kelekci, Mustafa Kemal Ozturk, Suleyman Ozcelik, Deniz Caliskan, Huseyin Cakmak, Pakize Demirel, Ekmel Ozbay ‘Improvement of breakdown characteristics of AlGa_N/Ga_N/Al_xGa_{1-x}N HEMT based on a grading Al_xGa_{1-x}N buffer layer’ Phys. Status Solidi A 207, No. 11, 2593–2596 (2010) / DOI 10.1002/pssa.201026270

7.Hongbo Yu, Mustafa Öztürk, Pakize Demirel, Huseyin Çakmak, Ekmel Ozbay ‘MOCVD growth and optical properties of non-polar (11-02) a plane Ga_N on r-plane (10-12) r-plane sapphire substrate’ Journal of Crystal Growth 312,3438-3442,2010

8. Hongbo Yu, Mustafa Ozturk, Pakize Demirel, Huseyin Cakmak, Basar Bolukbas, Deniz Caliskan, Ekmel Ozbay 'Metalorganic chemical vapor deposition growth and thermal stability of the AlInN/GaN high electron mobility transistor structure' *Semicond. Sci. Technol.* 26 (2011) 085010 (6pp)
9. Engin Arslan, Serkan Bütün, Yasemin Safak, Hüseyin Çakmak, Hongbo Yu, Ekmel Özbay 'Current transport mechanism and trap state investigation in (Ni/Au)-AlGaN/Schottky barrier diodes' *Microelectronic Reliability* 51, 576-580, 2011
10. E. Arslan, P. Demirel, H. Çakmak, E. Özbay 'Mosaic structure characterization of the AlInN layer grown on sapphire substrate' *Advances in Materials Science and Engineering* 2014
11. A Bayraklı, E Arslan, T Fırat, Ş Özcan, Ö Kazar, H Çakmak, E Özbay 'Magnetotransport study on AlInN/(GaN)/AlN/GaN heterostructures' *Physica status solidi (a)* 209 (6), 1119-1123
12. H Yu, M Ozturk, P Demirel, H Cakmak, T Buyuklimanli, W Ou, E Özbay 'Experimental study of two-step growth of thin AlN film on 4H-SiC substrate by Metalorganic Chemical Vapor Deposition' *Journal of optoelectronics and advanced materials* 12 (12), 2406-2412

C. Conference and Meeting Presentations

1. ICMATSE 2020 - Oral Presentation: ALD grown AZO Contacts for AlGaN/GaN HEMT Device Application
2. 17th International Conference on Metalorganic Vapor Phase Epitaxy (ICMOVPE, Lausanne-2014) Poster: In-rich InGaN epilayers and solar cells grown by MOVCD
3. 4th International Symposium on Growth of III-Nitrides (ISGN4, 2012 St. Petersburg, Russia)
Poster: The growth and characterization of In rich InGaN solar cell epitaxial structures by MOCVD
4. European Workshop on Metal Organic Vapor Phase Epitaxy
Wrocklaw/POLAND-2011
5. European Workshop on Metal Organic Vapor Phase Epitaxy
Ulm/Germany-2009
6. National Workshop on Optics, Electro-Optics and Photonics in Turkey
(2008-2009-2010-2011-2012-2013-2014-2017-2019)